

INFORMATION TO USERS

This manuscript has been reproduced from the microfilm master. UMI films the text directly from the original or copy submitted. Thus, some thesis and dissertation copies are in typewriter face, while others may be from any type of computer printer.

The quality of this reproduction is dependent upon the quality of the copy submitted. Broken or indistinct print, colored or poor quality illustrations and photographs, print bleedthrough, substandard margins, and improper alignment can adversely affect reproduction.

In the unlikely event that the author did not send UMI a complete manuscript and there are missing pages, these will be noted. Also, if unauthorized copyright material had to be removed, a note will indicate the deletion.

Oversize materials (e.g., maps, drawings, charts) are reproduced by sectioning the original, beginning at the upper left-hand corner and continuing from left to right in equal sections with small overlaps. Each original is also photographed in one exposure and is included in reduced form at the back of the book.

Photographs included in the original manuscript have been reproduced xerographically in this copy. Higher quality 6" x 9" black and white photographic prints are available for any photographs or illustrations appearing in this copy for an additional charge. Contact UMI directly to order.

UMI[®]

Bell & Howell Information and Learning
300 North Zeeb Road, Ann Arbor, MI 48106-1346 USA
800-521-0600

NOTE TO USERS

This reproduction is the best copy available

UMI

Ground-Based Infrared Remote Sensing of Cloud Properties
over the Antarctic Plateau

by

Ashwin Mahesh

A dissertation submitted in partial fulfillment
of the requirements for the degree of

Doctor of Philosophy

University of Washington

1999

Program Authorized to Offer Degree: Geophysics

UMI Number: 9944148

**Copyright 1999 by
Mahesh, Ashwin**

All rights reserved.


**UMI Microform 9944148
Copyright 1999, by UMI Company. All rights reserved.**

**This microform edition is protected against unauthorized
copying under Title 17, United States Code.**

UMI
300 North Zeeb Road
Ann Arbor, MI 48103

© Copyright 1999
Ashwin Mahesh

In presenting this dissertation in partial fulfillment of the requirements for the Doctoral degree at the University of Washington, I agree that the library shall make its copies freely available for inspection. I further agree that extensive copying of the dissertation is allowable only for scholarly purposes, consistent with "fair use" as prescribed in the U.S. Copyright Law. Requests for copying or reproduction of this dissertation may be referred to Bell and Howell Information and Learning, 300 North Zeeb Road, Ann Arbor MI 48106-1346, to whom the author has granted "the right to reproduce and sell (a) copies of the manuscript in microform and/or (b) printed copies of the manuscript made from microform. "

Signature 
Date August 20 1999

University of Washington
Graduate School

This is to certify that I have examined this copy of a doctoral dissertation by

Ashwin Mahesh

and have found that it is complete and satisfactory in all respects,
and that any and all revisions required by the final
examining committee have been made.

Chair of Supervisory Committee:

Stephen G. Warren.
Stephen G. Warren

Reading Committee:

Thomas C. Grenfell
Thomas Grenfell

Von P. Walden
Von P. Walden

Stephen G. Warren.
Stephen G. Warren

Date: 8-20-99

University of Washington

Abstract

Ground-based infrared remote sensing of cloud properties
over the Antarctic Plateau

Ashwin Mahesh

Chairperson of the Supervisory Committee
Professor Stephen G. Warren
Geophysics Program

A Fourier-transform interferometer, operated throughout the year 1992 at South Pole Station, measured downward spectral longwave radiance from 550 to 1500 cm^{-1} (7-18 μm) at a resolution of 1 cm^{-1} . Radiance measurements were usually made twice daily, coincident with routine launches of radiosondes made by the South Pole Weather Office; 252 radiance measurements were of cloudy-sky conditions. Cloud-base heights are retrieved from these data using a ground-based version of the radiance-ratioing method, originally developed to retrieve cloud-top heights from satellite data. Frequencies in the R branch of the 15- μm CO_2 band are used, exploiting the variation of atmospheric opacity with wavenumber.

A one-year climatology of cloud-base heights shows a bimodal distribution. Most clouds have bases in the lowest few hundred meters, within the surface-based temperature inversion. The other mode is of higher clouds with base heights 1.5 - 3 km above the surface. The retrieved cloud-base heights are in general uncorrelated with visual estimates made by observers at the South Pole Weather Office.

The longwave atmospheric emission spectra are also used to infer optical thicknesses and ice crystal sizes. This method makes use of the cloud's emissivity at 10 μm and 11 μm wavelength and the cloud's transmittance of stratospheric ozone emission in the 9.6 μm band. The difference in emissivity between 10 and 11 μm is sensitive to ice particle size because the absorption coefficient of ice varies greatly between these two wavelengths. The retrieval of optical depth (expressed as its value in the geometric-optics limit, τ_g) is limited to $\tau_g < 5$, and the effective particle radii r_{eff} are distinguished only for $r_{\text{eff}} < 25 \mu\text{m}$, but most (80%) of the clouds observed did have τ_g and r_{eff} in the retrievable range.

These clouds over the Antarctic interior are found to be optically thin, usually with $\tau_g < 1$, in contrast to coastal clouds which usually have $\tau_g > 20$. Most have r_{eff} in the range 5-25 μm , with a mode at 15 μm . The retrieved r_{eff} is larger in summer than in winter, in agreement with in-situ measurements.

Table of Contents

List of Figures	iii
List of Tables	v
Chapter 1. Introduction	1
1.1 Antarctic atmosphere	2
1.2 Review of previous measurements of Antarctic clouds.....	6
1.3 Cloud observations from satellites.....	13
1.4 Climate modeling of the Antarctic	17
1.5 Use of longwave spectral measurements	21
1.6 Organization of dissertation	23
Chapter 2. Cloud-Base Heights	32
2.1 Introduction	32
2.2 Data	33
2.3 Radiative Transfer Calculations	34
2.4 Retrieval of Cloud-Base Pressure	35
2.4.1 Method	35
2.4.2 Multiple Solutions.....	40
2.4.3 Uncertainties	43
2.4.4 Verification	44
2.5 Results	46
2.6 Conclusions	52
Chapter 3. Cloud Optical Depths and Particle Sizes	66
3.1 Introduction	66
3.2 Retrieval of Ozone-band transmittance	68
3.3 Retrieval of window emissivities	73
3.4 Minimization routine	76
3.5 Results	78
3.6 Comparison with independent observations	81
3.6.1 Crystal sizes	81
3.6.2 Cloud types	82
3.7 Conclusions	82
Chapter 4. Summary and Future Work	101
References	105

Appendix A. Comment on “Recent changes in the North American Arctic boundary layer in winter” by R.S. Bradley et al.	116
Appendix B. Radiosonde Temperature Measurements in Strong Inversions: Correction for Thermal Lag based on an Experiment at the South Pole	124

List of Figures

1.1	Surface temperatures at South Pole during 1992	26
1.2	Surface-based temperature inversion at South Pole, on May 01, 1992	27
1.3	Downward infrared spectra at the earth's surface.....	28
1.4	Spectral radiance measurements under cloudy and clear skies	29
1.5	Destruction of temperature inversion by a cloud.	30
1.6	Clouds over snow-covered sea ice.	31
2.1	The spectral radiance measurement under a cloud	57
2.2	Variation in e-folding distances of transmission in the 15- μm CO_2 band	58
2.3	Determination of cloud-base height in summer	59
2.4	Determination of cloud-base height in winter.	60
2.5	Cloud-base heights shown at their times of observation	61
2.6	Histogram of cloud-base heights at South Pole during 1992.	62
2.7	A one-year climatology of cloud-base heights	63
2.8	Is the bimodal distribution of cloud-base heights real?	64
2.9	Estimates of cloud-base heights made by observers at the SPWO	65
3.1	Spectral radiance measurements in the 9.6- μm band of ozone	84
3.2	Steps in determining transmittance from radiance measurements	85
3.3	Contribution of tropospheric ozone to downward radiance at the surface	86
3.4	Efficiencies of absorption, scattering and extinction	87
3.5	Spectral emissivity for ice clouds between 800 and 1200 cm^{-1}	88
3.6	Contours of effective emissivity and ozone-band transmittance	89
3.7	Emissivities at 903 cm^{-1} and 988 cm^{-1}	90
3.8	Clear-sky radiances in the 9.6- μm ozone band during 1992	91
3.9	Cloud optical depths and ice water paths during 1992-93.....	92
3.10	Histograms of optical depth and ice water path during 1992	93
3.11	Effective particle radii r_{eff} for clouds over the South Pole during 1992	94
3.12	Histogram of effective radii obtained at South Pole during 1992	95
3.13	Uncertainty in determination of particle radius and optical depth	96

3.14 Particle sizes and optical depths obtained at different viewing angles	97
3.15 Falling ice crystals at South Pole	98
3.16 Comparison of particle sizes obtained from spectra and photographs	99
3.17 Cloud-base heights and optical depths at South Pole, 1992	100

List of Tables

1.1	Height of surface-based inversion at South Pole	25
2.1	Uncertainties in cloud-base pressure	54
2.2	Comparison between values from radiance-ratioing and independent sources	55
2.3	Radiance ratioing applied to ARM data	56

Chapter 1: Introduction

Antarctica is the fifth largest continent; together with the large ice-shelves that extend beyond the continental margins, Antarctica covers approximately 14 million square kilometers. Over 97% of the continent is covered by ice, which in turn is covered by snow. At an average thickness of 2200 m, the Antarctic ice-sheet holds 90% of the fresh-water ice on the earth; were the ice sheet to melt entirely, the global mean sea level would rise by approximately 70 meters. With temperatures well below freezing even in summer over most of the continent, the snow is continually compressed under its own weight into ice. The ice sheet flows downslope and into the ocean surrounding Antarctica as ice shelves, which then calve off at the outer margins into the tabular icebergs commonly found in the Antarctic ocean. The sea-ice cover around the continent varies significantly through the year, with total surface areas ranging between nearly 20 million square kilometers in September-October and only 3 million square kilometers in March (Budd, 1991). Most of the sea-ice is first-year ice, but large areas of multi-year ice are also found, especially in the western Weddell Sea.

Antarctica can be broadly separated into three distinct zones, the high plateau in the eastern longitudes, the relatively lower regions of West Antarctica, and the Antarctic Peninsula stretching from the continental ice-sheet towards the southern tip of South America. The East Antarctic Plateau, which includes Amundsen-Scott South Pole Station, occupies 10.3 million square km, or roughly 70% of the continent. Weather stations on the plateau are widely separated from one another. There is little small-scale variation

in climate across the Antarctic Plateau above approximately 2500 meters; South Pole Station is thus representative of much of East Antarctica and the entire continental ice sheet.

1.1 Antarctic atmosphere

The atmosphere over the Antarctic Plateau is the coldest and driest on earth (Schwerdtfeger, 1970; 1984; Bromwich, 1979), representing an endpoint of terrestrial climate. The lowest recorded surface temperature on the earth was -89.2°C , measured at Vostok Station on July 21, 1983. The lowest average annual mean temperature was recorded at Plateau Station, which suggests that colder temperatures may exist along the topographic ridge of East Antarctica. The high elevation is also a barrier to water-vapor transport; water-vapor amounts on the high plateau are sometimes nearly as low as on Mars, (precipitable water at Plateau Station over a whole year varied between 0.05 and 0.3 mm - Kuhn, 1972), making Antarctica an ideal location for infrared astronomical observations.

The extreme conditions on the continent and its isolated location in the southern hemisphere long impeded extensive study of its surface and the atmosphere above it. Beginning in the 1770s and leading up to the 1820s, several explorers discovered various parts of the Antarctic coast, these were then named for them, for example, the Bellingshausen Sea and the Ross ice shelf. The earliest explorations of the higher elevations farther inland on the continent, however, took place only in the 1900s, when inland routes were discovered first by Robert Scott and later, Ernest Shackleton and others. Roald Amundsen first reached the South Pole on December 14, 1911. His expedition, like the others before him, was conducted during the summer. Many of the early explorers made

measurements of pressure, temperature, wind speed and direction on their journeys (King and Turner, 1997; Venter, 1957). These measurements, dating back to the 1900s, contributed to a rudimentary understanding of the continent's summer climate, but extensive monitoring and study of the Antarctic winter did not begin until the International Geophysical Year (IGY) of 1957-58, during which international agreements were reached to enhance the scientific exploration of the continent.

In-situ observations of the conditions on the plateau began to be routinely made at stations on the plateau in the late 1950s; South Pole Station was established in 1957. These data have since permitted the determination of mean climatic conditions at several weather stations. However, even data from the newly-established stations presented only a representative picture of the continent, since the stations were usually separated by large distances.

The long summer days, the elevation of the plateau and the small amount of water-vapor in the atmosphere above the continent permit large amounts of solar radiation to reach the surface. In fact, the Antarctic Plateau receives more summer sunshine than any other place on earth; Pionerskaya, located at an elevation of 2700 meters on the East Antarctic Plateau, receives 372 Wm^{-2} of solar radiation at the surface in December (Warren, 1996). This is also partly because the perihelion of the earth's orbit around the sun occurs in the austral summer. The radiative balance at the surface results from changes in solar radiation and in the upward and downward components of longwave radiation. Owing to the large solar zenith angles over the Plateau, and the high reflectivity of the snow surface, the effect of shortwave radiation on the radiative balance is limited to the short summer

period.

For the remainder of the year, the infrared radiation balance controls the surface energy budget. The upward component of longwave radiation is determined by the surface skin temperature since the infrared emissivity of snow is above 98% (Dozier and Warren 1982, Grenfell 1998). Surface temperatures are warmed by the presence of cloud; this produces increases in upward longwave radiation. But the downward infrared radiation from the atmosphere is the most variable component of the surface radiation budget for most of the year. In March, as the sun falls below the horizon, the surface quickly cools off for the long winter. At the onset of winter, the downward longwave radiation from the atmosphere, and the upward longwave from the cold surface quickly reach a balance, so that unlike at the coastal stations in Antarctica, the surface temperature on the Antarctic Plateau does not show a pronounced minimum at a specific time of the year. Instead, it is more or less constant throughout the winter, a phenomenon known as a “coreless” winter (Figure 1.1).

The cooling of the surface creates strong temperature inversions (Figure 1.2) which are maintained throughout the winter (Dalrymple, 1966) and preserve the balance between upward and downward longwave radiation. The strongest inversions typically occur under conditions of light winds and clear skies, but even under cloudy conditions the inversion is not fully destroyed. The temperature typically rises by about 30 degrees in the lowest few hundred meters from the surface, but extreme cases have been recorded where such a change occurred over a few tens of meters. The inversion is caused by the very high emissivity of the snow surface; radiative equilibrium with the lowest levels of

the much less absorptive atmosphere is achieved by the cooling of the surface. The strength of the surface-based inversion depends on elevation; as altitude increases, the atmosphere becomes thinner and less absorptive to infrared radiation. As a result, the surface must be at a lower temperature to reach radiative balance with the atmosphere, thus creating a stronger inversion. Storm-fronts generated off the Antarctic coast sometimes bring warmer temperatures and moister air inland. These fronts are usually detectable only at higher levels of the atmosphere (above 400 mb), but some fronts are strong enough to impact near-surface conditions and significantly diminish the surface-based temperature inversion.

The cooling of the Antarctic surface also cools the near-surface atmosphere relative to the air aloft; over the gradual slopes of the continent, the cold air flows downward as “katabatic winds”. Katabatic winds are a common feature of Antarctic climate; early explorers of the continent recorded the persistent nature of these winds as well as their constant direction of flow. The long winter permits persistently cold surface temperatures which maintain the negative buoyancy of near-surface air needed to maintain the winds. Katabatic winds strongly depend on clouds, since the cold near-surface temperatures which sustain them increase under cloudy conditions. Model results indicate that katabatic wind speeds are correlated with the strength of tropospheric meridional circulation present over the continent and off the coast of Antarctica (Parish, 1992).

Downward radiation is also important because of the way clouds alter it. Figure 1.3 shows that downward radiances in the atmospheric spectral windows ($550\text{-}600\text{ cm}^{-1}$,

800-1200 cm^{-1}) are much lower over Antarctica than elsewhere, because these regions are dominated by emission from water vapor, which is found in very low concentrations over the continent. Cloud emission in these spectral regions therefore can contribute relatively more to the downward radiance than in other parts of the world. Figure 1.4 shows a spectral measurement made from the ground under cloudy conditions at South Pole as well as a clear-sky spectrum calculated by radiative transfer modeling under similar atmospheric conditions; the large differences in the window region between the two curves suggests that the radiative impact of clouds on the surface is significant.

In recent years, study of the Antarctic, along with the Arctic, has received more attention, partly because it is believed that the signal of global warming will be observed first in the high latitudes (Manabe and Stouffer, 1979). Antarctica is involved in global climate change through radiative as well as hydrological processes, changes in precipitation or radiation budgets on the Antarctic plateau can affect these processes (Budd, 1991). The large difference in albedo between ocean water and snow-covered sea-ice makes the marginal ice-zones of the polar regions especially sensitive to rises in temperature, and some evidence of this has been observed, especially in the Antarctic Peninsula (Vaughan and Doake, 1996). Surface temperatures over much of the continent, however, are far below the melting point of water; even large changes in temperature may not melt the surface snow and ice. Antarctica could nevertheless experience indirect effects from global warming, such as changes in cloud-cover or precipitation.

1.2 Review of previous measurements of Antarctic clouds

The heightened interest in the polar regions has brought attention to the various

determinants of climate in the high latitudes. As elsewhere, clouds are especially important to climate on the Antarctic Plateau, affecting climate both by their influence on radiative processes and by their role in precipitation. However, unlike in other regions of the world, extensive studies of clouds, especially in situ observations, have not been conducted over the Antarctic Plateau; the research aircraft routinely used in other places have not been used nearly as much in Antarctica due to its remoteness. The few aircraft-based studies that have been carried out have been very limited, and include only a few observations. Ground-based remote-sensing of clouds too has been mostly limited to stations along the coast, where the clouds are considerably thicker and often contain liquid water, whereas limited studies indicate that clouds on the continent are much thinner and almost entirely ice-clouds.

Solar and infrared radiation are affected by clouds; solar radiation is partly reflected by clouds, increasing the outgoing radiance at the top of the atmosphere. Infrared radiation emitted by the earth's surface is trapped by clouds and re-radiated, leading to higher temperatures at the surface. In the polar regions, the shortwave effect is less important, as clouds do not significantly alter the planetary albedo, but the longwave effect is considerable. Figure 1.5 depicts an extreme case, and shows the effect of a passing cloud on near-surface temperatures at South Pole station on September 08, 1992; the 2-m temperature rises by as much as 16 degrees within 7 hours. Although the strength of the inversion (difference between the surface temperature and the temperature at the top of the inversion) is greatly affected by clouds, there does not appear to be any correlation between cloudiness and the height of the inversion itself (Table 1.1).

The global cloud distribution is recognized as forming a major component of the Earth's climate through its influence on both the energy and moisture exchanges in the Earth-atmosphere system. To determine the causes of differences among various model projections of climate change, Cess et al. (1989) compared 14 atmospheric general circulation models (GCMs); in this study; they noted that most of the variation in sensitivity of the models could be attributed to the way cloud-climate feedback processes were incorporated into the different models. Crane and Barry (1984) had earlier studied the influence of clouds on climate with a specific focus on high-latitude interactions and made the same observation, that model predictions of climate change are strongly connected to the determination of cloud radiative and microphysical properties and their proper inclusion in the models. Stephens et al. (1990), for example, showed that the influence of the cirrus clouds commonly found in the polar regions on climate was sensitive to the choice of effective particle size and the asymmetry parameter used in modeling them.

Studies of Antarctic clouds were initially carried out at coastal stations, and in the marine atmosphere off the coast of the continent. Wada and Takeda (1983) studied the correlation between atmospheric lapse rates and seasonal variations in cloud heights at Syowa Station in 1979 and 1980; whereas clouds forming under adiabatic lapse rates were seen both in the winter and summer, clouds were observed within isothermal layers only in the winter. Saxena and Ruggiero (1990) measured droplet size distributions in thin clouds between 75° and 80° S over the Ross Sea and Ross Ice Shelf and found a bimodal distribution of sizes, with an initial peak at 4 microns and a second one between 12 and 16 microns. Del Guasta et al. (1993) studied one year of cloud lidar data from Dumont

d'Urville, and compiled a climatology of cloud top and base heights. Clouds with base heights less than 1.5 km above the surface were the most common; a histogram of cloud base heights showed the number of observations falling steadily with increasing altitude.

Studies of clouds on the Antarctic Plateau itself have been fewer, and results from them have often been based on limited observations. Morley et al. (1989) made airborne observations of tropospheric clouds with a downward-viewing lidar during supply missions which spanned a total of six flights in January 1986 between South Pole, McMurdo Station and Siple Dome. They reported two types of clouds; midlevel clouds about 4-4.5 km above mean sea level; and higher, thin cirrus clouds. Morley et al. also recorded that water clouds ceased abruptly at the coast; clouds over the continent were made of ice crystals.

Stone et al. (1989) used surface radiation measurements to determine the radiative influence of clouds on the surface temperature at South Pole. Using daily mean values of surface temperature and the downward longwave irradiance measured during an entire year beginning in September 1987, they determined that the surface is always warmed by the presence of clouds in the winter, but they concluded that the influence of clouds on the surface temperature in the summer could be either negative or positive.

Stone and Kahl (1991) studied the variability in downward longwave flux and surface temperatures associated with cloudiness at the South Pole. Their study was based on 22 observations, 9 of which were under cloudy conditions. The authors found that surface temperature over the plateau is correlated with the downward flux, which in turn is corre-

lated with sky cover. Stone et al. also reported that the height of the surface-based inversion is greater when clouds are present (this is not observed in the year-long dataset used in this dissertation; see Table 1.1). Using coincident wind-direction data, the authors determined that inversions are weakened by the upslope transport of moist air from the N-NW direction, by increased downward mixing, and increased longwave heating of the surface by clouds. They suggested that parameters representing the inversion strength, as well as the tropospheric wind-shear, are appropriate indices for the detection of climate change on the Plateau.

Dutton et al. (1991) studied interannual variations in solar radiation, cloudiness, and surface temperature at the South Pole. Data from two pyranometers indicated that incoming solar fluxes during the austral summer decreased by 15% between 1976 and 1987, but most of this change was limited to the late summer months. A coincident 20% increase in cloud cover led the authors to believe that reduced insolation may have resulted from the increased sky-cover. Surface temperature time-series data from the same period were inconclusive. Some inconsistencies were also noted; changes in cloud cover were highest in February, but changes in surface temperatures were most noticeable in March. The authors also did not find any correlated changes in the surface-based inversions. Moreover, the trend in solar irradiance observed during the period was seen to be partly reversed in 1987 and 1988.

Studies have also been conducted to examine the impact of Antarctic clouds on radiation budgets at the surface as well as at the top of the atmosphere using satellite data. Nemesure et al. (1994) studied the impact of clouds on the shortwave radiation budget at

South Pole and in Saskatchewan, Canada, using ERBE data and coincident surface insolation measurements. They observed a negative correlation between the albedo at the top of the atmosphere and the solar irradiance reaching the surface. Since the latter is altered by cloud-cover, they concluded that clouds over snow-covered surfaces increase the planetary albedo. Yamanouchi and Charlock (1995) compared radiation budgets at the top of the atmosphere (TOA) and surface in the Antarctic from ERBE and surface-based measurements at Syowa and at South Pole. By plotting cloud amounts from surface synoptic observations against fluxes, they determined that cloud radiation heats the surface and cools the atmosphere. Longwave radiative effects were seen to be larger than shortwave effects. In the interior of the plateau, clouds have very little effect on the absorption of solar radiation by the atmosphere, and along the coast they slightly increase it. Extremely low surface temperatures throughout the long winter produced net longwave cooling at the top of the atmosphere in the interior of the plateau, but net warming along the coast.

Determining the relationships between cloud cover and other quantities is also impeded by the fact that during the long winter over the Plateau, estimates of cloud cover often are made in darkness, without the benefit of moonlight. Schneider et al. (1989) binned sky-cover observations according to lunar illuminance, and analyzed nighttime synoptic total sky coverage data from South Pole Station from 1976-1985; they found systematic errors in the observational record of cloud cover. They estimated that undercounting of cloud occurrence to be as high as 50%; this was later shown to be a miscalculation by Hahn et al. (1995), who compiled cloud climatologies based only on data collected under sufficiently moonlit conditions to be reliable.

Stone (1993) attempted to determine the physical radiative and microphysical properties of Antarctic clouds. Radiometersonde measurements of upward and downward fluxes from the 1960s were interpolated to 25 mb resolution and analyzed with coincident radiosonde data. However only 8 winter-time observations reliably met the criteria for inclusion in the analysis. The vertical profiles of flux and temperature were used to determine cloud top and base. The average cloud base height from the eight observations was 465 meters above the surface; Stone observed that the cloud base was often coincident with the top of the surface-based inversion. Stone estimated the emissivity and optical depths of the clouds by comparing the observations to model comparisons made at 10.8 μm ; he found the average emissivity to be 0.6, the mean optical depth to be 1.0. Stone concluded that clouds on the plateau are similar to high-level cirrus clouds observed in the mid-latitudes.

By comparing the emissivities with theoretically computed values for model clouds with various particle sizes and ice water contents (IWCs), the clouds' effective particle sizes were also inferred. In the model calculations, the cloud particles were represented as spheres with surface areas equal to that of the ice crystals; comparisons from these calculations showed that particle radii varied between 4 and 16 μm , while IWCs were between 0.3 and 6 mg m^{-3} . Despite the small datasets of his observations, and the large uncertainties in the flux measurements as well as in determining the cloud base pressure and temperature, these findings, along with Stone's earlier observations, have formed the basis for much of the conventional wisdom about clouds on the Antarctic Plateau.

In recent years, the determination of cloud properties has been facilitated by the

development and application of remote-sensing algorithms to shortwave and longwave spectral measurements. Using data from a Fourier Transform Interferometer (FTIR) at Palmer Station, Lubin (1994) determined the radiative properties of coastal clouds by comparing observations to radiative transfer model calculations. Spectral measurements were made between August and November 1991, at 1 cm^{-1} resolution from 5-20 microns. Model calculations were compared to observed emission spectra from the clouds, and cloud properties - emissivity, infrared optical depths, and the effective size of the particle size distribution - were determined, assuming the clouds were liquid. Most low-lying clouds were found to have optical depths between 5 and 10; higher clouds were thinner. The effective radius of the particles in the coastal clouds was found to be between 9 and 11 microns. Ricchiuzzi et al. (1995), however, determined much greater optical depths from solar flux measurements at Palmer station during that same spring of 1991. Simultaneous retrievals of cloud optical depths and surface albedo were made using discrete ordinate radiative transfer (DISORT) model calculations to match the observations of flux at 410 and 630 nm. The surface albedo at 630 nm was found to be higher than 0.9; cloud optical depths for overcast conditions varied between 20 and 50, with a median value around 25.

1.3 Cloud observations from satellites

Over the Antarctic Plateau itself, Lubin and Harper (1996) obtained cloud radiative properties at South Pole from Advanced Very High Resolution Radiometer (AVHRR) infrared data. Radiances in Channels 4 and 5 (11 and 12 μm) were observed to depend on effective cloud temperature, emissivity, ice water path, and effective radius of the particle size distribution. From AVHRR imagery covering the South Pole during 1992, the mean

cloud emissivity was estimated at 0.43 in the summer and 0.37 during winter. Estimates of effective radius were also made for both seasons; the average was 12.3 μm in summer and 5.6 μm in winter. Lubin and Harper concluded that AVHRR retrievals reasonably record the overall seasonal variations in cloud properties, but also noted that reliable findings from satellite data require coincident ground measurements as well. The usefulness of satellite data is limited by the fact that radiative transfer solutions for cloud heights are not single-valued in the polar regions (King et al., 1992). Also, during months when the polar vortex is present over much of Antarctica, infrared radiances recorded by the AVHRR may often include radiation from polar stratospheric clouds.

As satellite data became available, researchers sought to apply these to gain a greater understanding of the role of clouds in climate. The automated inference of cloud properties from satellite spectral data, however, requires the validation of some observations using surface-based spectral measurements of clouds. Similarly, automatic cloud classification algorithms applied to satellite data need to be validated with ground based observations of clouds. Such automation is inhibited by the fact that surface and satellite observations produce very different sets of data. Surface measurements are localized; the satellite data may be more representative of area averages of cloud cover. However, the two aren't always comparable; satellite data record high clouds more often than low clouds, whereas surface-based observations accomplish the reverse. Initially, climatologies from satellite data had to be compiled mostly by manual interpretation of the data (e.g., Clapp, 1964); these limitations were gradually overcome as automation was established in the 1970s and early 1980s. Reviewing several early climatologies of cloud prop-

erties from satellite data, Hughes (1984) noted that the polar regions were among the regions of greatest disagreement between the climatologies. This is partly because clouds over snow surfaces are not consistently seen to be brighter or darker than the surface; this makes their automated detection in the visible part of the spectrum difficult. Figure 1.6 shows satellite observations of clouds over snow-covered sea ice; in the upper frame, the cloud-covered snow is darker than the clear sky over snow, whereas it is brighter in the lower frame. Early cloud-cover assessments made by the International Satellite Cloud Climatology Project (ISCCP), for example, were considerably different from surface-based observations of cloud occurrences in the polar regions (Rossow et al., 1993), being up to 25% lower in the summer (Figure 13, Hahn et al., 1995).

Yamanouchi et al. (1987) determined that brightness temperature differences between AVHRR channels 3 and 4 were useful to detect water clouds at the coast of Antarctica near Syowa, but were much less reliable in determining clouds farther inland. Due to surface-based temperature inversions seen over the plateau for most of the year, cloud-top temperatures are also similar to surface temperatures; this limits the use of infrared brightness temperatures to distinguish between the two. Surface-based inversions also further make the determination of cloud heights inaccurate, as the radiative transfer solutions of height are not single-valued; clouds at the same temperature but at different heights are not discernible from one another using satellite data. To the extent that the inference of particle size and cloud optical depth requires accurate knowledge of cloud heights, they could also be in error.

Owing to the small contrast in infrared brightness temperatures as well as the small

contrast in visible brightness between clouds and the snow-covered surface (Yamanouchi et al., 1987), alternative cloud-detection algorithms have been necessary in the polar regions. Despite advances in the development of such schemes, uncertainties persist. Ebert (1987) developed a technique to detect clouds in the polar regions using pattern recognition and spatial coherence. Spectral features were identified which yielded information about albedos and brightness temperatures; alongside, textural features were identified that provided information on variability of the scene. By classifying clusters within the scene based on these features, the region under observation was determined to be one of seven surface types or one of eleven cloud categories. Model sample-scenes were classified correctly over 90% of the time, and tests of the detection algorithm on AVHRR data were accurate 83% of the time.

Ebert (1989) further improved the pattern-recognition technique to include information on spatial coherence, and applied it to summertime Arctic data from the AVHRR. The automated classification of cloud types and the determination of cloud fractions were both in reasonably good agreement with manual interpretation of the images and with surface observations, but uncertainties in cloud fraction were sensitive to the classification. A further refinement of the method (Ebert, 1992) used both infrared and visible channel data from the AVHRR, but only infrared channels were useful in classifying wintertime observations. Sakellariou et al. (1993) developed a technique to distinguish between clear and cloudy regions at high latitudes in the summer using all five channels of the AVHRR. Using reflectivity from the visible and near-IR channels (1,2 and 3), and brightness temperatures from channel 4 (in the thermal IR) cloudy and non-cloudy (including both clear

and partly cloudy) pixels are identified; non-cloudy pixels are further analyzed to determine the nature of the surface as well. On a second pass, brightness temperatures from the fifth channel (also in the thermal IR) are also included in the classification scheme, and using a series of thresholds, cloudy pixels are distinguished from clear ones. Such techniques, while improving the process of automated cloud detection, still do not match surface-based observations consistently.

Stone et al. (1990) addressed the problem of retrieving cirrus cloud optical depth from satellite radiance measurements using AVHRR near-infrared (NIR) and thermal infrared (IR) measurements. Independent estimates of cloud optical depths were made using ground-based lidar and radiometric (LIRAD) flux measurements as well as satellite data. Radiance differences between the NIR and IR channels were related to particular emissivities and cloud optical depths by radiative transfer modeling; values obtained by this spectral-differencing method were compared to modeled values under varying assumptions, to select relationships between optical depths and observed spectral differences. The LIRAD-derived optical depths agreed 70% of the time with satellite estimates for optical depths greater than about 0.3, but were dissimilar for thinner clouds; model calculations using equivalent spheres of equal surface areas suggested that particle radii were between 32 and 65 microns. Comparisons between spatially-averaged LIRAD data and time-averaged LIRAD data may also have been responsible for some inconsistencies, especially if cloud properties changed during the experiment.

1.4 Climate modeling of Antarctica

Along with advances in observation and analysis, model simulations of climate on

the Antarctic Plateau are used to obtain further insights. Initially, the relative lack of meteorological and radiation data from the Antarctic hindered the ability to provide stringent tests of computer model simulations of the climate of the plateau (Simmonds, 1990). However, as polar cloud properties were determined from observations, researchers then sought to include them in climate models, to arrive at better ways of predicting climate change. Ebert and Curry (1992) parametrized cloud properties in terms of the ice water path and the effective radius of the ice-crystal size distribution, at five wavelengths each in the shortwave and the longwave. This parameterization assumed that ice crystals can be approximated as randomly oriented hexagonal cylinders whose size is represented by the radius of a sphere with equivalent surface area. The parameterization allowed the variation of the effective radius and ice-water path independent of each other. Model calculations based on this parameterization showed that a change in effective particle size has a greater effect on the system albedo than a change in the ice-water path, whereas the longwave greenhouse effect was more sensitive to the ice-water path than to particle shape.

Despite continuing disagreement among various global climate models, numerous advances in understanding cloud-climate feedback processes over the last few years, have brought them into much better agreement (Cess et al., 1995). The availability of surface-based measurements and aircraft data from field experiments around the world has greatly enhanced the validation of climate models, and perhaps being thus constrained to simulate such “ground truth”, the models now agree better. This evolution of model representation is seen in efforts to model the climate of Antarctica as well. Simmonds (1990) noted that given the uncertainties in the data used for climatological statistics in the southern high

latitudes, climate models have done a reasonable job of simulating the Antarctic climate, but added that there is obvious need for improvement in both modeling and observations. He suggested that model calculations could be improved by better treatment of physical processes at high southern latitudes. Budd and Simmonds (1991) determined that precipitation and evaporation changes on the Antarctic continent would change sufficiently in case of reduced sea-ice off the coast and global warming to provide a small but significant offset (4 mm/yr. of lowering) to the expected sea-level rises.

Tzeng et al. (1993) examined the representation of the Antarctic climate by the NCAR Community Climate Model version 1 (CCM1). Katabatic winds, surface temperatures over the continent, the circumpolar trough, and the snowfall accumulation were analyzed. The CCM1 captured the phase and amplitude of variations in temperature reasonably well. The model, however, predicted anomalously large precipitation amounts over the continent and did not represent the katabatic winds reliably. A year later, Tzeng et al (1994) examined the NCAR CCM2 model, a successor to the CCM1 with higher horizontal resolution. They found that this model simulated several aspects of Antarctic climate reasonably well, such as the position and strength of the circumpolar trough, the coreless surface temperatures in winter over the plateau, the intensity of the surface-based temperature inversions, and the aridity of climate on the plateau. However, the model results contained some errors too; surface temperatures over the plateau in the summer and on the coasts in winter were colder than the observations indicated, and cloudiness over the continent continued to be higher than known from surface observations. Nevertheless, the authors concluded that the CCM2 was an improvement to its predecessor in its ability

to simulate Antarctic climate and probably good enough to be used for climate change studies.

Chen et al. (1995) examined the simulation of polar climates from 1979-88 by 14 global climate models as part of an international effort to determine the systematic errors of atmospheric models, called the Atmospheric Model Intercomparison Project (AMIP). Comparisons between models were based on the models' ability to simulate sea-level pressure, cloudiness, precipitation and evaporation/sublimation. The comparisons revealed that the reliability of model simulations in the high latitudes primarily depends on the horizontal resolution of the models and their treatment of physical processes.

Lubin et al. (1998) conducted a sensitivity study also using the NCAR Community Model version 2 (CCM2), but with modifications to include ice clouds instead of water clouds, to determine the sensitivity of regional and hemispheric climate to the optical properties of Antarctic clouds. Against a control run using 10- μm water clouds, the authors examined the effect of changing the optical properties of clouds over the continent to those of ice clouds of particle radius 10 μm without changing the cloud water path, and also of ice clouds of larger particles (40 μm), under perpetual January conditions. Cloud radiative forcing at the top of the atmosphere, as well as net radiation at the surface were examined. On the continent itself, temperature increases of 1-2 degrees were observed throughout the Antarctic troposphere. Total cloud fraction predicted by the model over Antarctica was smaller than in the control run at low levels of the troposphere, but larger than in the control elsewhere in the troposphere.

When model calculations were made with the radiative properties of 40- μm ice clouds instead, similar changes to those seen with 10- μm ice clouds were seen, but additionally, the surface temperatures over Antarctica cooled by up to 3 degrees C compared to the control run. Surprisingly, changing the cloud radiative properties to those of 10- μm ice clouds over Antarctica was seen to have significant impacts not only on the climate of the continent but even through the tropics and into the northern hemisphere. The authors hypothesize that climatic impacts in the tropics result from a weakening of the north-south temperature gradient, which in turn produces changes in polar meridional circulation, cloud cover, and the location and intensity of the circumpolar trough, as well as changes in the tropics.

1.5 Use of longwave spectral measurements

Walden (1995) compiled the South Pole dataset of observations made at South Pole Station during a year-long field program. The dataset includes 1- cm^{-1} -resolution infrared spectral measurements of the downward radiance, taken twice-daily throughout the year. Additionally, data from routine radiosonde launches conducted by the South Pole Weather Office, and ozonesonde data from NOAA's Climate Monitoring and Diagnostics Laboratory (CMDL) are also available.

In recent years, remote-sensing techniques have been developed and applied to such data taken elsewhere to derive the microphysical and radiative properties of clouds. Smith and Frey (1990) used spectral measurements from aircraft to determine cloud top heights using the radiance-ratioing method (Smith et al., 1974). Longwave spectral data have also been used to determine cloud optical depths and effective particle sizes. (e.g.,

Smith *et al.*, 1993; Lubin, 1994). Strabala *et al.* (1994) applied the “trispectral method”, which uses brightness temperature differences in the 8-12 μm spectral region, to distinguish ice clouds from water clouds. Grund *et al.* (1990) proposed that attenuation of stratospheric ozone emission by thin clouds could be used to determine their optical depths.

Although most of the commonly-used techniques were developed for application to downward-viewing measurements taken from aircraft or satellites and initially used in studies at lower latitudes, they can be adapted to spectral measurements made from the Antarctic surface. Such measurements offer a wide array of information about the conditions of the south polar troposphere, including the spectral longwave cloud forcing, cloud base heights, effective cloud particle radii, and optical depths. The subset of radiance measurements made under clear skies was used to make detailed comparisons between radiative transfer model representations of the Antarctic atmosphere and actual measurements (Walden *et al.*, 1998).

High-resolution spectral data, such as those in the South Pole dataset, also permit more accurate deduction of cloud properties using radiative transfer equations than data from satellites. Satellite data are often taken at specific spectral bands, whereas the dataset used in this study includes the entire spectrum between 550 and 1500 cm^{-1} . The Advanced Very High Resolution Radiometer (AVHRR), for example, makes measurements at only two adjacent channels in the same spectral region over which the South Pole dataset contains several hundred points. Uncertainties in cloud properties derived from

the spectral data are reduced by having more spectral information. This is especially important in the Antarctic, where the atmospheric mean-free-path of photons rapidly increases from a few meters (at 667 cm^{-1}) to hundreds of kilometers (at wavenumbers greater than 760 cm^{-1}) within a short spectral span (see Figure 2.2 in Chapter 2). Such rapid variation in atmospheric transmission limits the number of frequencies which are most sensitive to clouds at any given height; the few channels on satellite-based sensors do not always contain frequencies most suited to a given problem, whereas continuous spectral data overcome that limitation.

1.6 Organization of dissertation

This dissertation presents a climatology of cloud properties obtained from the South Pole dataset. This is the first cloud climatology of the Antarctic Plateau based on year-long data; cloud properties obtained here significantly add to our knowledge of the properties of clouds in the troposphere over the Plateau. Also, results from this work can be readily included in climate models, to permit better simulation of current Antarctic climate and more reliable estimates of future climates over Antarctica.

The dissertation is organized as follows: A climatology of cloud base heights is presented in Chapter 2; these heights were obtained by modifying an algorithm used to determine cloud top heights from satellite data. The applicability of the algorithm to spectral data taken in other polar and temperate winter environments is also discussed in this chapter. In Chapter 3, climatologies of effective cloud particle radii and optical depths are presented. These were determined by model comparisons to calculated values of radii and optical depth over a wide range.

Particle sizes obtained from the spectral measurements are compared to values obtained from photographs of falling ice crystals taken during the same period; Chapter 3 includes this work. The radiative and microphysical properties obtained in model calculations are sensitive to the shapes and sizes used to represent the cloud particles (Stephens, 1980; Platt, 1989). Model calculations made by Stephens, for example, showed that the infrared reflectance of cirrus clouds at cloud base was 50% higher when the cloud particles were modeled as cylinders instead of spheres. Particle radii are obtained by three methods of specifying equivalent spheres, and an appropriate one is suggested for future use.

Chapter 4 lists the major conclusions of this dissertation and future work that is planned.

Table 1.1: The average height of the top of the surface-based inversion at South Pole in 1992, obtained from radiosonde measurements of temperature in the lower troposphere. Only the autumn, winter and spring months are shown; inversions are not as common in the summer months although isolated instances can be seen from December to February as well. The inversion height is not consistently increased or decreased by clouds.

Month	z (clear) meters	z (cloud) meters
March	522	567
April	668	586
May	652	769
June	617	609
July	690	667
August	532	693
September	527	616
October	732	647

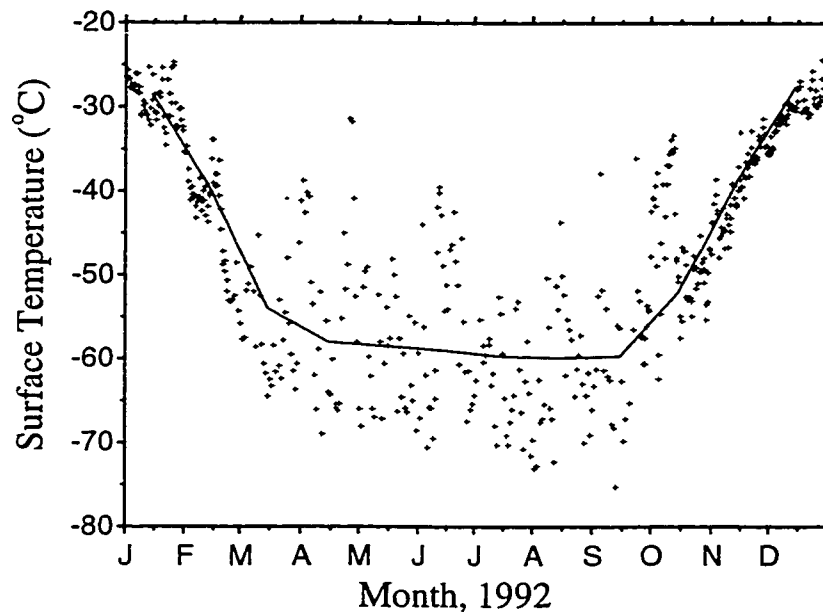


Figure 1.1. Surface temperatures at South Pole station during 1992 (dots). Temperatures are shown during the times of routine radiosonde launches conducted by the South Pole Weather Office (SPWO). When the sun sets at the end of the short summer, surface temperatures near -60° to 65°C are reached within a few weeks, and remain near this “coreless” value for most of the winter, except when warm air intrudes from the coast. The solid line shows the long-term monthly average surface temperatures at South Pole (from King and Turner, 1997).

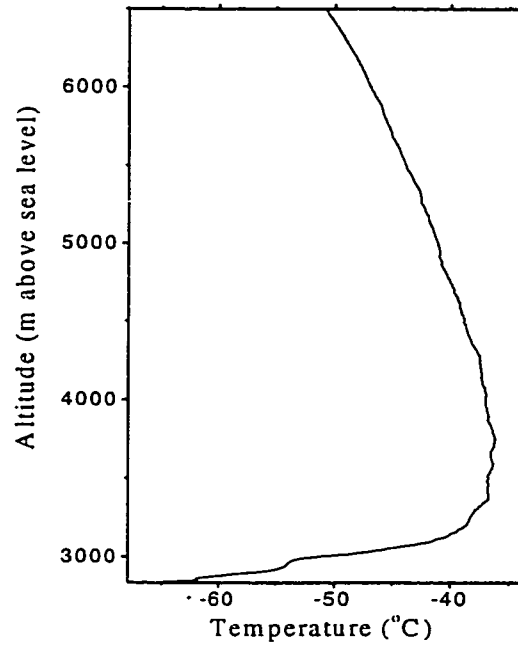


Figure 1.2. Surface-based temperature inversion at South Pole station, on May 01, 1992. The large difference in emissivity between the lower troposphere and the snow surface forces the surface to cool down rapidly once the sun sets, creating the inversion. A rise in temperature of 20-30 degrees in the lowest 300-600 meters above the surface is typical.

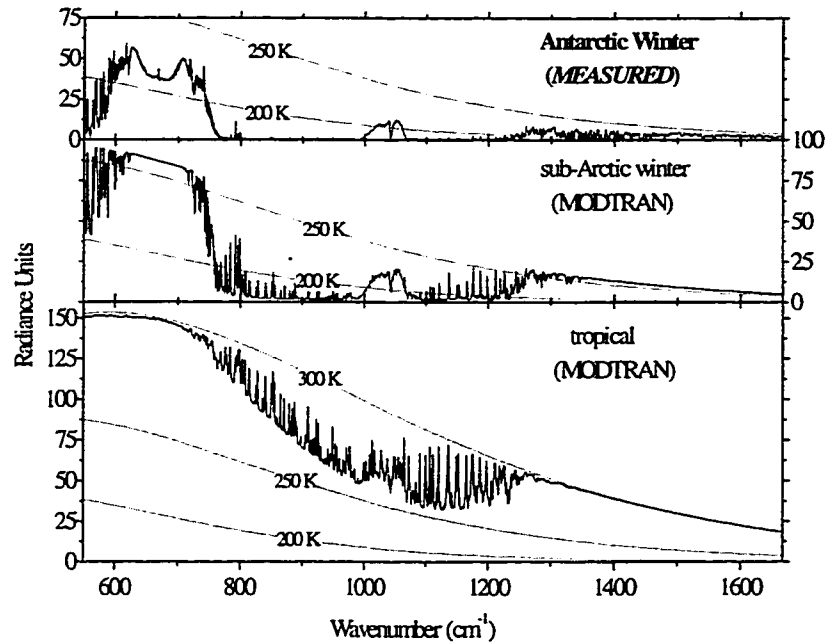


Figure 1.3. Downward infrared spectra at the earth's surface, under clear sky, from three different terrestrial atmospheres. The Antarctic winter spectrum was measured at South Pole Station on May 1, 1992. The sub-Arctic winter and tropical spectra are model simulations using MODTRAN (Berk et al., 1989). The viewing angle is 60 degrees from zenith; the spectral resolution is 1 cm^{-1} .

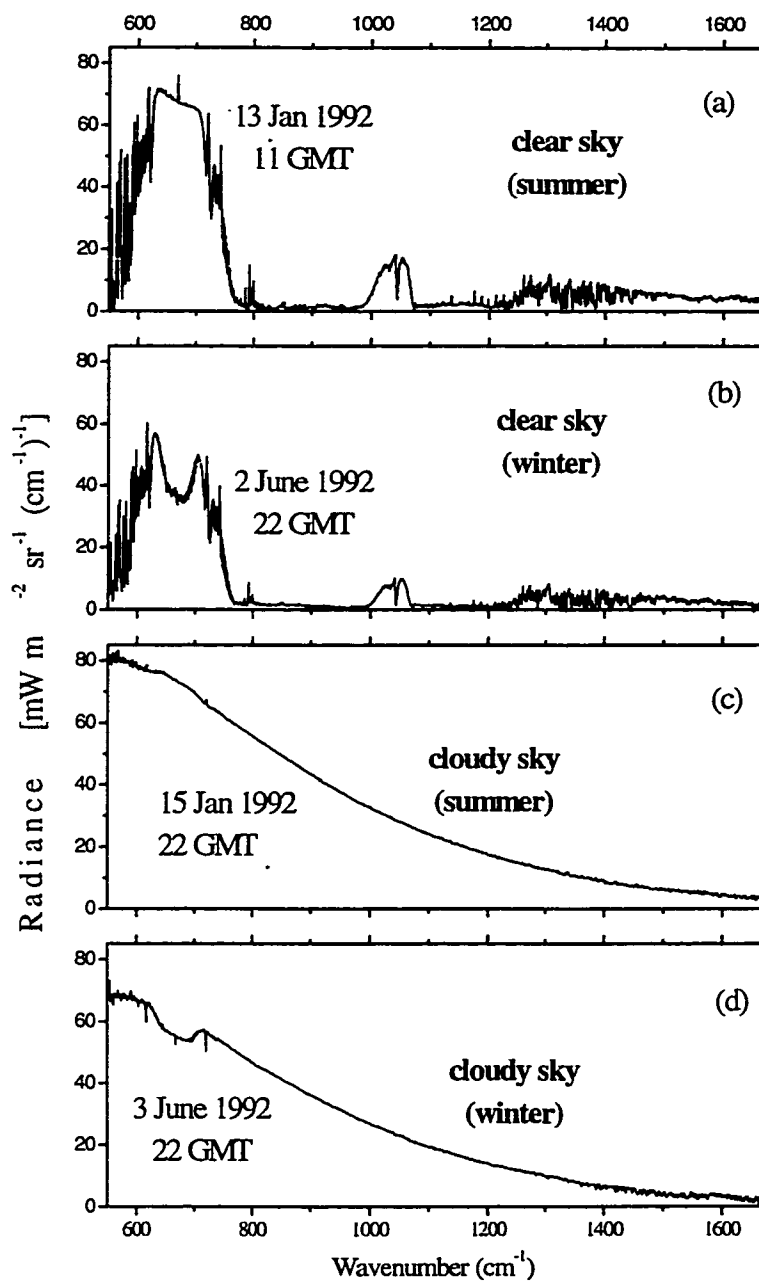


Figure 1.4: Spectral radiance measurements under cloudy and clear skies in the summer and winter at South Pole, at a zenith viewing angle of 45 degrees. The very low window radiances seen in the clear-sky spectra are due to the low water-vapor content of the Antarctic atmosphere; as a result downward radiation from clouds has a relatively higher impact on the surface radiation budget over Antarctica than elsewhere.

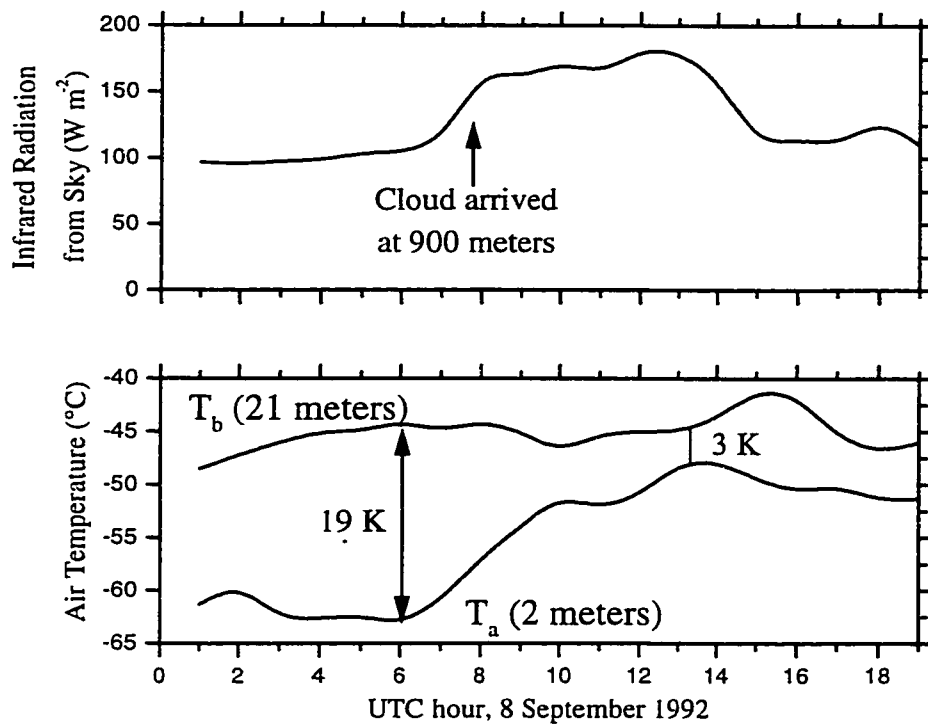


Figure 1.5. Destruction of surface-based temperature inversion at South Pole Station by a cloud. Before the cloud arrives, near 0700 UTC, the inversion is very strong, with 19K separating the temperature at 2 m (T_a) and the temperature at 21 meters (T_b). The cloud reduces this temperature difference to as little as 3K, most of the change occurring in the first two hours after the cloud arrives.

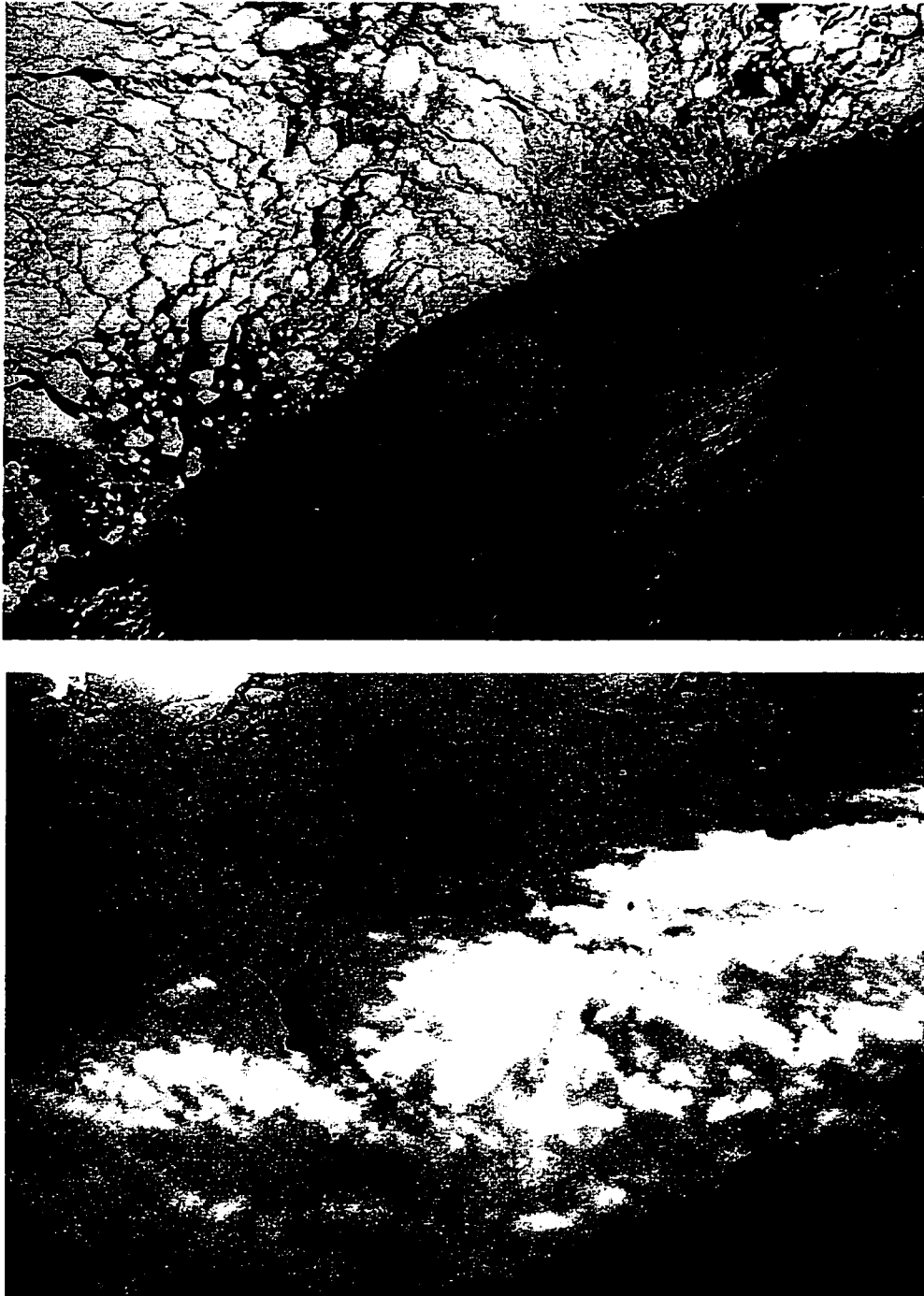


Figure 1.6. Clouds over snow-covered sea ice. (a) Landsat nadir view, north of Alaska, solar zenith angle 79° . (b) Photograph from airplane over the Ross Sea. Clouds are seen to be sometimes darker and at other times brighter than the snow surface.

Chapter 2: Cloud-Base Heights

2.1. Introduction

Retrievals of cloud properties from infrared satellite sensors are difficult over Antarctica because the snow surface is frequently at least as cold as the cloud, often making it difficult to identify a cloud, let alone infer its properties (Yamanouchi et al. 1987).

Ground-based remote sensing methods have the advantage that the background is cold space, whose brightness temperature can be much lower than that of the cloud. Ground-based remote sensing can therefore be useful for determining the properties of clouds relevant for the energy budget and also for aiding the development of cloud-retrieval methods applied to satellite data. Climatologies of cloud properties obtained from spectral data can be included in general circulation models (GCMs), providing a better representation of global climate. South Pole Station is located in a region that is representative of much of the Antarctic continent; a climatology obtained here can represent much of the Antarctic Plateau. In the past, the validation of GCMs has been inhibited by the lack of long datasets from polar regions; the high latitudes are therefore inadequately represented in these models (Simmonds 1990). More recent modeling work also suggests that proper inclusion of Antarctic cloud properties in these models is critical; significant changes in regional climate are observed when cloud properties are altered (Lubin et al. 1998).

Using Advanced Very High Resolution Radiometer (AVHRR) channels at 11 and 12 μm , Lubin and Harper (1996) showed that outgoing longwave radiances over the Antarctic Plateau depend on effective cloud temperature, ice water path, and effective radius of the cloud particle size distribution. However, the relationships they obtained were limited by uncertainties and by lack of unique solutions to the radiative transfer equations.

Retrieved solutions for cloud heights from satellite data are often multi-valued in the polar regions because of surface-based temperature inversions (King et al. 1992). In this paper, we show that ground-based remote sensing can overcome this limitation, permitting clouds below the inversion to be distinguished from those above it.

2.2. Data

Moderate-resolution (1 cm^{-1}) infrared radiance spectra were measured using a Fourier-transform interferometer (FTIR) at viewing zenith angles of 45° , 60° , and 75° (Walden *et al.* 1998). The interferometer was located on the roof of a building on the upwind side of the station. The important sources of errors in the measurements were investigated by Walden (1995), namely the radiance error induced by the uncertainties in the temperatures and emissivities of the calibration sources, and by thermal instability of the interferometer. The estimated radiance error at wavenumber $\nu=811 \text{ cm}^{-1}$ under clear skies is $1.5 \text{ mW m}^{-2} \text{ sr}^{-1} (\text{cm}^{-1})^{-1}$ (Radiance Unit; RU). About 5% of the spectral radiance measurements were discarded as unreliable, due to lack of thermal stability of the interferometer during an observation sequence lasting about 25 minutes.

If the radiance at 811 cm^{-1} exceeded three times the estimated radiance error at each viewing angle, and also was larger than 5 RU (this threshold, at 75° and for typical particle sizes, corresponds to an optical depth of about 0.06), corresponding to a brightness temperature of 164 K, the scene was classified as “cloudy”, otherwise it was “clear”. Of the 516 measurements made during 1992, 225 observations met this threshold for cloud detection.

The radiance measurements were usually made twice daily, at about 10:30 and

22:30 UT. These were the times of the routine radiosonde launches conducted by the South Pole Weather Office (SPWO) in summer (November-February); in winter radiosondes were launched only once a day at 22:30 UT, so half of the wintertime FTIR observations were made close to the time of a radiosonde launch. The atmospheric temperature profile corresponding to each radiance measurement was determined by interpolation of the profiles from sondes launched before and after the radiance measurement. The temperature profiles were corrected for the thermal lag of thermistors on the radiosondes according to the method of Mahesh *et al.* (1997); this is necessary to remove errors in temperature as the sonde rises through steep near-surface inversions. For temperatures above 30 km we used monthly-average temperatures obtained by the Upper Atmosphere Research Satellite (UARS) (Walden 1995). Surface air concentrations of carbon dioxide at South Pole were measured by NOAA's Climate Monitoring and Diagnostics Laboratory (CMDL); monthly averages were used in this study. During 1992, a ceilometer was operated by the South Pole Weather Office. However, after careful examination we concluded that the data from that instrument were unusable, and thus could not be used as an alternative source of cloud-base heights.

2.3. Radiative Transfer Calculations

For this paper, clear-sky radiances were calculated using the Line-By-Line Radiative Transfer Model (LBLRTM, Clough *et al.* 1992). Modifications were necessary to the LBLRTM subroutine ALAYER which calculates the path of refracted radiation through layers in a model atmosphere. In an atmosphere with a strong near-surface temperature inversion, ALAYER sometimes produced ray paths originating at one layer boundary that

did not exit at the other boundary, especially in the very cold layers near the surface. We therefore changed the ray-tracing algorithm in ALAYER for this particular application in consultation with the authors of the code (Pat Brown and Tony Clough, personal communication).

Figure 2.1 shows a radiance measurement made under a cloud, as well as a clear-sky spectrum computed using the ancillary data described above. At the center of the 15- μm band (667 cm^{-1}), the two spectra are identical. The opacity of the atmosphere in this region is very large; most of the radiance received by the instrument is emitted within a few meters of it. At higher wavenumbers, the transmittance of the atmosphere increases, permitting photons from increasingly greater distances to reach the instrument. Until the cloud base is reached, however, the two spectra remain similar. At even higher wavenumbers, the spectrum of the cloud is noticeably different from that of the clear sky. This difference increases in the atmospheric window regions, and at 810 cm^{-1} , a reference wavenumber used in our method, the clear-sky radiance is only a small fraction of the radiance from the cloud.

2.4. Retrieval of Cloud-Base Pressure

2.4.1 Method

Variation of atmospheric transmittance with wavenumber in the 15- μm band of carbon dioxide has been used in the past to determine cloud-top heights. The “CO₂-slicing” method was introduced by Smith et al. (1974) to determine cloud-top heights from infrared spectral data taken from satellites (Chahine, 1974; McCleese and Wilson, 1976; Smith and Platt, 1978; Menzel et al., 1983). More recently, the method was applied to

obtain cloud-top heights from high-resolution infrared spectral radiance data taken from aircraft (Frey 1988; Smith and Frey 1990). Wielicki and Coakley (1981) used the term “radiance-ratioing” to describe this method, which describes the physical principle used in the CO₂-slicing method. We have modified this procedure for ground-based remote sensing of cloud-base heights, using the spectral variation of atmospheric transmission.

The radiance-ratioing method relies on the fact that within the 15- μm band of carbon dioxide, the average distance a photon travels is different at different wavenumbers. We define the e-folding distance at a particular wavenumber as the *vertical* distance into the atmosphere from which transmission to the surface is $1/e$. The e-folding distances therefore vary with viewing angle; they are shown in Figure 2.2 for wavenumbers between 660 and 750 cm^{-1} . The CO₂ band is used because CO₂ is a well-mixed gas, so that the e-folding distances do not change from one day to the next.

The wavenumbers that are best suited for detecting cloud-base heights are those which have e-folding distances comparable to the distance from the interferometer to the base of a typical cloud. At wavenumbers between 667 and 700 cm^{-1} , the atmosphere is highly opaque, so that radiation reaching the surface comes from the nearby atmosphere rather than from the cloud base. Wavenumbers greater than about 755 cm^{-1} are less useful in determining the base heights of tropospheric clouds, since at these wavenumbers the e-folding distances of transmission into the atmosphere are greater than 100 kilometers. The useful wavenumber range is therefore 700-755 cm^{-1} . The e-folding distance is a function of the viewing zenith angle θ ; therefore, different subsets of wavenumbers are useful in obtaining cloud base heights from observations at different angles: 700-740 cm^{-1} at

$\theta=45^\circ$, $700-748 \text{ cm}^{-1}$ at $\theta = 60^\circ$, and $700-755 \text{ cm}^{-1}$ at $\theta=75^\circ$.

Smith et al. (1974) showed that the observed radiance (I_{obs}) measured above or below a non-black cloud can be related to the radiance from the clear sky (I_{clear}), as well as the radiance that would be emitted by a black cloud (emissivity equal to 1) at the same height (I_{bc}). By ratioing the difference of the observed and clear-sky radiances at two different wavenumbers, ν and ν_o , the following relationship is obtained (derivations are given by Smith et al. 1974, and more recently by Frey 1988).

$$\frac{I(\nu, \theta)_{\text{obs}} - I(\nu, \theta)_{\text{clear}}}{I(\nu_o, \theta)_{\text{obs}} - I(\nu_o, \theta)_{\text{clear}}} = \left(\frac{A\varepsilon(\nu, \theta)}{A\varepsilon(\nu_o, \theta)} \right) \times \left(\frac{I(\nu, \theta)_{\text{bc}} - I(\nu, \theta)_{\text{clear}}}{I(\nu_o, \theta)_{\text{bc}} - I(\nu_o, \theta)_{\text{clear}}} \right), \quad (1)$$

where ν is a wavenumber in the wing of the CO_2 -band that is sensitive to cloud-base height, ν_o is a reference wavenumber in the nearby window region where CO_2 does not absorb, θ is the viewing zenith angle, A is the cloud cover fraction within the field of view of the instrument, and $\varepsilon(\nu)$ is the spectral emissivity of the cloud.

The reference wavenumber, ν_o , is chosen to be as close to ν as practical, so that $\varepsilon(\nu) \sim \varepsilon(\nu_o)$, which allows them to cancel in (1). The variation of cloud emissivity between ν and ν_o is a limitation of methods that use satellite data taken at specific channel wavelengths (e.g., Lubin 1994). Data sets with continuous spectra, such as ours, allow the reference wavenumber to be chosen much closer to the wings of the CO_2 band, reducing errors caused by differences between $\varepsilon(\nu)$ and $\varepsilon(\nu_o)$.

Cancelling the cloud fraction and spectral emissivities in (1), we obtain

$$\frac{I(\nu, \theta)_{\text{obs}} - I(\nu, \theta)_{\text{clear}}}{I(\nu_o, \theta)_{\text{obs}} - I(\nu_o, \theta)_{\text{clear}}} = \frac{I(\nu, \theta)_{\text{bc}} - I(\nu, \theta)_{\text{clear}}}{I(\nu_o, \theta)_{\text{bc}} - I(\nu_o, \theta)_{\text{clear}}} \quad (2)$$

To calculate the cloud-base height, we calculate the two terms in (2) separately.

The left-hand term,

$$\gamma \equiv \frac{I(\nu, \theta)_{\text{obs}} - I(\nu, \theta)_{\text{clear}}}{I(\nu_o, \theta)_{\text{obs}} - I(\nu_o, \theta)_{\text{clear}}} \quad , \quad (3)$$

can be computed without specifying the cloud-base height; it requires only the observation and a clear-sky calculation. The right-hand term

$$R(p_c) \equiv \frac{I(\nu, \theta)_{\text{bc}} - I(\nu, \theta)_{\text{clear}}}{I(\nu_o, \theta)_{\text{bc}} - I(\nu_o, \theta)_{\text{clear}}} \quad , \quad (4)$$

is a function of the cloud base pressure p_c , where the radiance from a black cloud is computed as

$$I(\nu, \theta)_{\text{bc}} = B(T_c)t(p_c, p_s) + \int_{p_c}^{p_s} B(T(p)) \frac{d}{dp} t(p, p_s) dp \quad , \quad (5)$$

where $B(T)$ is the Planck function for temperature T , T_c is the cloud base temperature, t is transmittance between two pressure levels, p_s is surface pressure, and p_c is the cloud-base pressure which we are solving for. The first term, γ , is found by subtracting a clear-sky calculation from a spectral radiance measurement at two frequencies. The clear-sky calculation depends primarily on the atmospheric temperature structure, obtained from radiosonde data taken routinely at South Pole Station. The viewing zenith angle used in the calculation is the same as the one at which the radiance measurement was made.

The second term, $R(p_c)$, is a calculation assuming a black cloud at pressure p_c ; p_c is varied until $R(p_c) = \gamma$, giving the solution p_c for the cloud-base pressure. The transmit-

tance in (5) was determined as follows. Using monthly-average temperature profiles, the transmittances from the surface to many vertical heights in the atmosphere were computed for each wavenumber, yielding a matrix of transmittances. The instrument did not always stop at exactly the specified angle for each observation. However, the angle was recorded for each observation; for any given month it varied over roughly a 3-degree range. Therefore, we computed the transmission matrices at the extremes of the viewing angle as well as for the average viewing angle. Matrices for individual observations at a particular viewing angle were obtained by linear interpolation.

The quantity $R(p_c)$ is calculated for black clouds at many pressure levels within the troposphere; the cloud base is the pressure at which $\gamma=R$. An estimate of the cloud-base pressure is obtained at each wavenumber between 700 and 755 cm^{-1} at which the e-folding distance of transmission lies within the troposphere. The final estimate of cloud-base pressure is found in a second pass by weighting the initial estimates obtained at each wavenumber according to the estimated accuracy of each estimate, as follows. The slope of R versus p in a 10-mb interval centered on the initial estimate of cloud-base pressure is determined at each wavenumber, and each estimate of cloud base pressure is weighted by this slope. The highest weights are typically awarded to those wavenumbers whose e-folding distance of transmission into the atmosphere are comparable to the distance from the surface to the cloud base, since at these wavenumbers the atmospheric weighting functions (dt/dp in (5)) peak near the cloud base.

In many cases, the same cloud is observed at two or three viewing angles. The cloud base pressure p_c is obtained at each angle, and if the values of p_c are similar the two

or three values are averaged. The radiosonde temperature profile is then used to convert cloud base pressure to base height.

Figure 2.3a shows a summertime temperature profile in the lowest 3 km, plotted next to a graph of γ and $R(p_c)$ at a representative wavenumber of 716 cm^{-1} . The temperature profile shows a cloud-top inversion at 4000 m above sea level (1200 m above the surface). There are three values of p_c for which $R=\gamma$. For this case, the first crossing of γ and R is chosen as the cloud-base pressure, designated by the horizontal dashed line. The following section describes how this solution was chosen.

2.4.2 Multiple Solutions

In atmospheres with temperature inversions, multiple solutions are often obtained, only one of which is the correct cloud base. The difference in emissivity between the cloud and the overlying atmosphere often causes a cloud-top temperature inversion, which is seen in the temperature profile in Figure 2.3a. In cases such as this one, the base of the cloud can be determined from the temperature profile as the solution at the highest pressure, closest to the surface. But a cloud at either of the other two pressures where $R=\gamma$ would result in the same measured radiance at this frequency. This situation with a cloud-top inversion is rare for Antarctic continental clouds; only a few thick summertime clouds in 1992 produced noticeable changes in the lapse rate. In winter, no cloud-top inversions were noticeable in the soundings.

A much more common situation is *surface-based* temperature inversions, which also cause multiple solutions (Figure 2.4), but in this situation the choice of the correct cloud-base pressure is more difficult than for elevated inversions. On the Antarctic Pla-

teau, strong surface-based temperature inversions occur throughout most of the year. This condition leads to two intersections of R with γ if the data are perfect (and sometimes no intersection in real data with measurement errors). However, in such cases, the temperature profile is not helpful in determining the correct solution.

Figure 2.4 shows temperature profiles for June 8 and July 7, and plots of R and γ on these two days for two wavenumbers. Visual estimates by the SPWO place the cloud well above the top of the inversion in the June case, and within the inversion in July. The temperature inversion causes two solutions for the cloud-base pressure in both cases at 716 cm^{-1} , a representative “far-sighted” wavenumber. We call a wavenumber “far-sighted” if the e-folding distance of transmission into the atmosphere is typically greater than the height of the surface-based inversion, and “near-sighted” if only radiance from the within the inversion reaches the interferometer. Assuming the SPWO observations to be correct, the solution in the June case is the intersection at the lower pressure (higher altitude), whereas in the July case the higher-pressure solution (lower height) is correct (indicated by the filled circles in Figure 2.4).

To resolve the ambiguity without reference to the visual observations, we use near-sighted wavenumbers ($670\text{-}700 \text{ cm}^{-1}$), which are only sensitive to clouds within the inversion. At these wavenumbers, almost none of the emission from above the inversion reaches the interferometer. As seen in Figure 2.4 at 716 cm^{-1} , the e-folding distance of transmission into the atmosphere includes both solutions. This is generally true for all wavenumbers between 700 and 755 cm^{-1} . At lower wavenumbers, the increased opacity of the atmospheric CO_2 eliminates the solution at lower pressure. The curves of R and γ at

the representative near-sighted wavenumber of 681 cm^{-1} illustrate this point. In the July case, γ and R intersect, indicating a cloud within the inversion layer. In the June case, when the cloud is well above the inversion, there is no intersection of γ and R . Instead R merely approaches γ . In the absence of errors, γ and R would become equal beyond the distance of maximum transmission at near-sighted wavenumbers. When the cloud is above the inversion as in Figure 2.4f, errors, which can be both positive and negative, can cause γ and R to intersect at a few wavenumbers. If, on the other hand, the cloud is below the inversion as in Figure 2.4c, such intersections are much more likely, since not all negative errors in γ will eliminate the solution, and most positive errors will not destroy the intersection (unless the errors are large). Thus, the percentage of near-sighted wavenumbers at which a cloud is detected is large when the cloud base is within the inversion, and small when the cloud base is above the inversion. Visual estimates of cloud base height, made by the SPWO as well as by us, were also used in 11 cases to resolve ambiguities.

When surface-based temperature inversions are present, distinctions between multiple solutions are possible using wavenumbers at which only one of them is detectable. From satellites, however, it would be necessary to find wavenumbers at which the e-folding distance of transmission into the atmosphere from the satellite extends to the cloud above the inversion, but not to the one below it, which would be extremely difficult even with high-resolution spectral data.

2.4.3 Uncertainties

Uncertainties in cloud base heights derived by the radiance ratioing method are estimated using test cases. Uncertainties in radiance measurements (I_{obs}), concentrations

of CO₂, and the temperature profile all cause variations in the points of intersection of R and γ . Additionally, the viewing zenith angle is uncertain by 1.5°. For observations at $\theta=75^\circ$, this is a significant source of uncertainty in cloud base heights. Another important source of uncertainty is the variation in cloud emissivity between the reference wavenumber (811 cm⁻¹) and the wavenumbers used to determine cloud base height (700-755 cm⁻¹). Although emissivities in the wings of the 15- μ m band of CO₂ differ from the window emissivities by 10% or more, (Wielicki and Coakley, 1981), most of this difference (7%) occurs at wavenumbers greater than 811 cm⁻¹ (Wu, 1987). Using a reference wavenumber at 811 cm⁻¹, we estimate the average uncertainty in the ratio ϵ/ϵ_0 to be 3% across the wavenumber region from 700 to 755 cm⁻¹.

One source of uncertainty we do not consider is that a change in tropospheric humidity between the time of the radiosonde launch and the FTIR observation could cause a change in the clear-sky window radiance at 811 cm⁻¹. This source of uncertainty could be significant in warmer, more humid, atmospheres but is unimportant on the Antarctic Plateau, where water-vapor emission at 811 cm⁻¹ is always extremely small.

Table 2.1 shows the uncertainties in cloud-base pressures due to all the sources considered. In each case, these quantities were perturbed by the magnitude of the estimated uncertainties, both positive and negative, and the cloud-base pressures were recalculated. Uncertainties in CO₂ concentration cause small errors in cloud-base pressures, but uncertainties in the temperature profile and the angle of observation can result in uncertainties of up to 35 mb. Due to errors in various input quantities, solutions may not be obtained at all wavenumbers; uncertainties in these test cases are not monotonic with

angle, as a result. The bases of low clouds are more accurately derived than those of high clouds; a given change in temperature, which is the variable in the radiance-ratioing process, corresponds to a small change in pressure below the inversion, but higher in the atmosphere the same change in temperature corresponds to a larger change in pressure, as the lapse rate is not so large. Generally, the uncertainty in cloud-base pressure is found to be approximately 20-25 mb for low clouds and 30-55 mb for high clouds; uncertainties are also greater at larger zenith viewing angles (25-55 mb) than at smaller angles (20-40 mb).

Uncertainties in base height also result from the fact that clouds over the Antarctic Plateau are often thin ($\tau < 1$). The cloud base obtained in such cases may not lie close to the actual cloud base; the solution is instead obtained as the effective temperature at which the cloud radiates, and could be well above the cloud base. Radiosonde temperature profiles indicate that cloud thicknesses are typically less than 1 km. Also, even in the case of thin clouds, the base height obtained by radiance ratioing lies is bound by the range of temperatures that occur within the cloud.

2.4.4 Verification

On six occasions during the field program, the cloud-base height was determined directly by other methods. On occasion, the SPWO launches "pilot balloons" with a known ascent rate, which allow the cloud-base height to be estimated by measuring the time from launch until the balloon disappears into the cloud. In addition, incoming aircraft occasionally report the cloud-base height as they descend through the cloud. Table 2.2 shows our estimates of cloud-base height compared to the values obtained from these other sources. The agreement for low clouds is good, whereas the agreement for the high

cloud is poor. Some of the difference may be attributed to changing cloud conditions.

Another way to verify the radiance ratioing method is to use a comparable dataset from a different location. Using data taken in 1996 with the Atmospheric Emitted Radiance Interferometer (AERI) at the Southern Great Plains (SGP) site of the Atmospheric Radiation Measurement (ARM) Program, we derive cloud base heights using the radiance-ratioing method and compare those heights to lidar measurements made concurrently by a Micro-Pulse Lidar.

Over a two-week period during which clouds at different heights were seen, and which included periods of clear skies, we usually obtained cloud base heights close to those reported by the lidar. Additionally, we used several AERI measurements from a six-hour period when the cloud base height remained steady at about 700 m above the surface, and were able to repeatedly obtain the same cloud base using radiance ratioing. Comparisons were made at the times of radiosonde launches to keep uncertainties in the vertical temperature profile to a minimum. Table 2.3 shows a comparison of cloud base heights obtained by radiance ratioing with those reported by the lidar. The lidar data have coarse vertical resolution (300 m) and our values all lie within this uncertainty.

The radiance-ratioing method produces solutions that are directly related to the temperature of cloud base. At the ARM site, the lapse rates in the atmospheric temperature profile are smaller than at the South Pole, introducing greater uncertainty in the derived cloud-base height. When lapse rates are small, γ and R intersect at a smaller angle, and a given uncertainty in the measurement causes a larger error in the derived cloud base height. On the other hand, there is usually no surface-based inversion at this site, which

removes the ambiguity frequently encountered at the South Pole. Without the inversion, isothermal layers are also rare, whereas at South Pole, the sometimes broad nose of the inversion causes errors in cloud base height determined by the radiance ratioing method.

2.5. Results

Figure 2.5 shows the cloud base heights determined from 225 observations during the year, about 40% of all observations made during the year. This number corresponds well to the average cloud cover reported by visual observers of 43% (Hahn et al. 1995, Fig. 13b). The interferometer was located 11 m above the snow surface; the base heights reported here are given as height above the surface, not height above the instrument. Cloud bases are higher in summer than in winter. In the winter, clouds are often seen in the lowest 500m, with bases below the top of the surface-based temperature inversion. Since we detect only the lowest cloud, it is possible that higher clouds are also present. It is also possible that seasonal differences in cloud base heights seen in Figure 2.5 are particular to 1992; it will be useful to obtain additional years of data.

Figure 2.6 shows a histogram of the base heights obtained from all observations of clouds during the year. Cloud base heights are distributed into two distinct modes. Clouds are often seen in the lower 500m, typically within the surface-based inversion. A second mode, of higher clouds, is also seen distributed over a much wider range of base heights. The lowest cloud is almost always within 5 km of the surface (8 km above sea level). The tropopause at the South Pole is typically 5-6 km above the surface (Warren 1996, Figure 3), so all the clouds whose bases were located by the radiance ratioing method are in the troposphere. "High" clouds on the Antarctic Plateau are thus lower than elsewhere on

Earth, where the “high” cloud level usually means $Z_B > 6$ km. The bimodality of the distribution is discussed later.

At wavenumbers larger than 755 cm^{-1} the e-folding distance of transmission into the atmosphere is several tens of kilometers or more, and at these wavenumbers polar stratospheric clouds (PSCs) can be detected. However, the radiance-ratioing method cannot be used to determine their base heights. Observations of PSCs are shown outside the range of the vertical axis in Figure 2.5, indicating that the base heights exceed 6 km but cannot be quantified. Intersections of R and γ correspond to specific temperatures in the atmosphere; since PSCs are much colder than any tropospheric clouds, they can be detected by this method. To locate their base heights accurately, however, we would require sufficient wavenumbers at which atmospheric transmission extends beyond the troposphere, but not much farther than the height of a typical PSC. There are only a few wavenumbers at which the e-folding distance of transmission into the atmosphere is comparable to the typical base heights of PSCs. The weighting functions, even at these few wavenumbers, do not have strong peaks in the stratosphere, but are instead fairly broad. Broad weighting functions introduce too much uncertainty to be useful in detecting cloud base heights accurately in the stratosphere.

The interferometer had to be turned off during blizzards because its external mirror became coated with blowing snow, and it was shut down for a few other brief periods. Therefore, the cloud base heights presented so far do not constitute a climatology. To obtain a more representative climatology, we filled in values for missing days. Each day, the instrument was scheduled to make two observations, beginning at 1000 UT and 2200

UT. A total of 732 cases would therefore be necessary to compile a climatology for the entire year. Our FTIR dataset comprises 514 observations; we fill in the missing values as follows. In blizzard conditions, the instrument was turned off, and it was restarted immediately following each blizzard. We assumed that throughout the blizzard, cloud conditions were unchanged from the last observation immediately prior to the blizzard. Other missing values were also filled in similarly.

A climatology of cloud base heights, developed using such ‘persistence’ criteria, is shown in Figure 2.7. Some of the missing values were classified as clear-sky, so they do not appear. The streak of uniform cloud base height during June is the longest period during which missing values were filled in as clouds.

Stone (1993) reported cloud base heights from eight observations of winter clouds at the South Pole. His study was based on radiometersonde measurements, and is discussed in Part II. He reported that the cloud base is typically at the top of the inversion; the bimodal distribution we find, in contrast, suggests that whereas base heights are either above or below the inversion, they are rarely at the top of the inversion itself.

We now consider the possibility that the bimodal distribution seen in Figure 2.6 is an artifact of the radiance ratioing method. If the cloud base were exactly at the top of the inversion, then errors in any of the input quantities will result in solutions being formed above or below the inversion if the derived solution is at a lower temperature (or no solution for base height if the solution temperature exceeds the warmest temperature in the troposphere at the top of the inversion). As a result, cloud base heights would always lie below or above the inversion, which itself is typically around 600 - 650 m. Since the min-

imum of the bimodal distribution is at approximately this height, this potential artifact demands investigation.

Using calculations of cloud radiance from model clouds, and perturbations of the atmospheric temperature profile, we examined the errors in cloud base height that would be caused by perturbations of 3 K in the lowest 1 km of the atmosphere. The average uncertainty in cloud base height, for a cloud whose true base height is exactly at the top of the inversion, is at most 20 mb, or about 150 - 200 m. The radiance ratioing method relies on picking solutions that are either below or above the inversion and not exactly at the top of the inversion. Lapse rates below the top of the inversion are very steep and a temperature error of 3 K is unlikely to affect the determination of cloud base height by more than 5-10 mb. A cloud exactly at the top of the inversion is likely to be detected by several near-sighted wavenumbers. As a result, the radiance ratioing method would determine the cloud base height as the solution below the top of the inversion rather than the one above the inversion. Steep lapse rates within the inversion limit the error in cloud base height when the solution below the inversion is chosen.

On the other hand, if we were to choose the solution above the inversion, uncertainties as high as 25 mb are possible with a temperatures uncertainty of 3 K because lapse rates above the inversion are much less steep. However, in most of the cases, the radiance measurements were made coincident with the radiosonde launch, and the temperature errors we permitted in these simulations (± 3 K) are extremely generous. We thus conclude that temperature errors will not cause the shape of the distribution in Figure 2.6 to change much. This can also be verified by examining how the distribution of base heights

might look if in fact cloud bases are exactly at the top of the inversion instead of where we diagnose them to be.

The three parts of Figure 2.8 illustrate this. In the first panel (8a), the distribution of base heights diagnosed by our method is shown; this is identical to Figure 2.6. We then considered the subset of cases where the cloud base is more than 200 meters from the top of the inversion, but the difference between the temperature at cloud base and the temperature at the top of the inversion is less than 3 K. These cases represent the subset of our observations that are most likely to be affected by the fact that our method does not determine base heights that are exactly at the top of the inversion, and instead moves them away. A height difference of less than 200 meters is not significant since errors due to input parameters can cause comparable uncertainty in our determination of cloud base height, and similar uncertainties due to the method itself do not worsen the determination of cloud base height any further.

Assuming that this subset of cloud base heights has been erroneously determined, we reset the base heights for each of these clouds to the top of the inversion on that day. Note that 3 K represents a generous estimate of the temperature uncertainty in our radiosonde profiles. Despite this, the corrected distribution of base heights (Figure 2.8b) is not greatly altered, and still retains a bimodal appearance. Even if we grossly exaggerate this experiment and reset all values of cloud base within 6 K of the inversion temperature to the top of the inversion, the bimodal nature is still retained (Figure 2.8c). These experiments exaggerate the impact of errors due to the method by being generous in choosing the subset. Yet the bimodal distribution persists, indicating that the distribution of base

heights shown in Figure 2.6 is not an artifact of our method. Cloud bases are often located below or above the top of the inversion, but rarely exactly at the top itself.

Additionally, it is important to keep in mind that the bimodal distribution is a distribution of base heights, and it is quite probable that in the cases where the base height is below the inversion, the cloud itself extends through the top of the inversion. The average height of the inversion is about 600-650 meters, and even thin clouds with bases below the inversion can reasonably be assumed to extend beyond the top of the inversion.

The visual estimates of cloud base height made by the observers at the SPWO also show a bimodal distribution. However, the absolute values of such observations are not very reliable. Figure 2.9a shows the estimates of cloud base heights made by observers at the SPWO, along with our values derived from radiance ratioing. Comparisons were made only for the cases where the SPWO observations were within 2 hours of the FTIR measurement. The observers at the SPWO estimate the base height in hundreds of feet above the surface. The strings of values at 1500 m and 1800 m are reports of 5000 feet and 6000 feet. The average cloud base height from visual observations is close to that from radiance ratioing, but the individual values are uncorrelated. In the absence of reference objects, such as mountains, tall structures, etc., the observers really have no reliable way of making estimates of cloud base heights, and that is clearly seen in the figure. Figure 2.9b limits the comparison to the observations made under conditions of good illumination of the clouds, which should facilitate their identification by visual observation. There is still no correlation of the SPWO base heights with the FTIR base heights; however, as with the base heights determined by us, observations made by SPWO observers

also show a bimodal distribution.

2.6. Conclusions

Cloud base heights can be determined from surface spectral measurements of longwave emission by radiance ratioing, a technique originally developed for the determination of cloud top heights from satellite data. To resolve ambiguity in the retrieval, a variation on the radiance ratioing method has been developed here, that permits clouds above the surface-based inversion to be distinguished from those below it. Clouds appear to form in two distinct modes, one with base heights below the surface-based inversion and the other with bases 2-3 km above the surface. We do not have an explanation for why these two modes exist, but this result is consistent with visual observations; research into cloud formation mechanisms over the Plateau is needed to explain the distribution of base heights.

The cloud base heights derived in this study permitted the development of a limited climatology over the Antarctic Plateau. It would be desirable to continue these measurements in additional years, with ancillary data from a lidar and a frost-point hygrometer on a tethered balloon.

Acknowledgments. Eric Ray provided the monthly average profiles of temperature and ozone from UARS data for elevations above 30 km. Tony Clough and Pat Brown helped us identify the reason for the LBLRTM code's failure when applied to the Antarctic winter-time inversions, and helped in our efforts to rewrite the code for our purposes. Data for clouds over Oklahoma were obtained from the Atmospheric Radiation Measurement

(ARM) Program sponsored by the U. S. Department of Energy, Office of Energy Research, Office of Health and Environmental Research, Environmental Sciences Division. We thank David Bromwich for helpful discussions. This research was supported by NSF grants OPP-94-21096 and OPP-97-26676.

Table 2.1 Uncertainties in cloud-base pressures for individual test cases due to uncertainties in the vertical profile of temperature $T(z)$, the emissivity ratio (ϵ/ϵ_0), the zenith angle of observation (θ), the carbon dioxide concentration, and the measured radiance I_{obs} . The retrieved cloud-base pressure is p_c , the cloud-base height is Z_B , and H is the height of the top of the inversion.

Test Case	Z_B (m)	p_c (mb)	H (m)	input quantity	uncertainty in cloud base pressure (mb)		
					45°	60°	75°
January 26, 1992	945	603	-	$T(z)$	11	-	13
				ϵ/ϵ_0	10	-	9
				θ	7	-	11
				CO_2	1	-	1
				I_{obs}	8	-	9
				Total	18		21
June 08, 1992	2112	501	650	$T(z)$	29	26	28
				ϵ/ϵ_0	13	14	17
				θ	15	22	27
				CO_2	3	3	5
				I_{obs}	17	12	21
				Total	39	39	47
July 10, 1992	918	643	330	$T(z)$	22	21	29
				ϵ/ϵ_0	13	19	29
				θ	11	23	35
				CO_2	3	8	5
				I_{obs}	12	25	22
				Total	30	45	58
July 16, 1992	356	670	550	$T(z)$	18	15	21
				ϵ/ϵ_0	5	6	8
				θ	4	12	14
				CO_2	1	1	5
				I_{obs}	10	10	9
				Total	22	22	28

Table 2.2 Comparisons of cloud base heights derived from the radiance-ratioing method, with measurements from other sources..

Date	Z_B from radiance ratioing (m)	Z_B from other sources (m)	Time between two observations (hours:minutes)	Time between radiosonde and spectral measurements (hours:minutes)
January 20, 1992	397	270	0:15	0:10
February 15, 1992	160	180	0:05	0:10
June 3, 1992	360	240	11:45	1:50
June 4, 1992	286	390	0:25	1:45
December 29, 1992	2270	1350*	0:15	0:20
January 7, 1993	276	360**	1:00	0:20

* The nearest surface observation of cloud base height was reported 20 minutes after the spectral data were taken. The earlier observation, made 40 minutes before the spectral data were taken, reports the cloud base height at 1800 m, which agrees better with the value derived from radiance ratioing.

** Broken clouds were reported at this height; one other simultaneous cloud base height (at 900 m) was also reported. However, this second value is not reported as measured, but is reported as an estimate. It is not known which of these two clouds was in our field of view.

Table 2.3 Cloud base heights obtained by the radiance ratioing method are compared to those obtained by LIDAR at the ARM Southern Great Plains Site in Oklahoma for both randomly chosen clouds and a steady cloud system. The lidar's resolution is 300 m.

Cloud Conditions	Date and Time (UT)	Z_B (LIDAR) (m)	Z_B (radiance ratioing) (m)
Steady cloud base height over 6-hour period	Nov 1, 1996, 05:31	720	711
	Nov 1, 1996, 06:44	1020	825
	Nov 1, 1996, 08:08	1020	795
	Nov 1, 1996, 09:28	1020	885
	Nov 1, 1996, 11:05	1020	797
	Nov 1, 1996, 11:55	1020	874
Selected clouds at differ- ent heights	Oct 28, 1996, 13:32	720	560
	Nov 9, 1996, 05:29	2820	2640
	Nov 7, 1996, 13:31	2820	2810

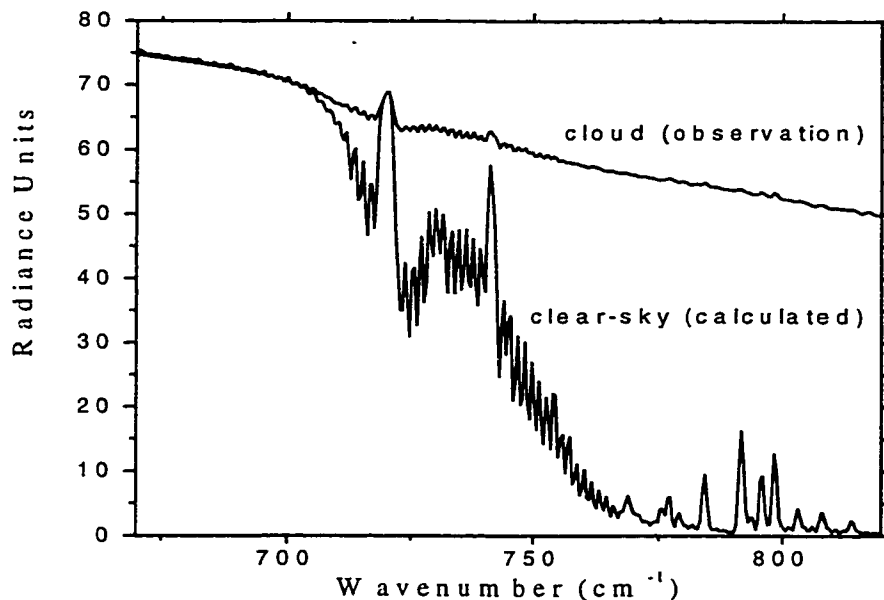


Figure 2.1: The spectral radiance measurement under a cloud (on January 26, 1992) at the South Pole, along with a simulated clear-sky spectrum calculated by radiative transfer modeling. Near the center of the 15- μm band of CO_2 (667 cm^{-1}), the opacity of the atmosphere is very high, and most of the observed radiance is emitted from very close to the instrument. At these wavenumbers, radiance from the cloud is not detected by the instrument. As we move to higher wavenumbers, the opacity of the atmosphere decreases, and the spectrum of the cloud is increasingly different from that of the clear sky.

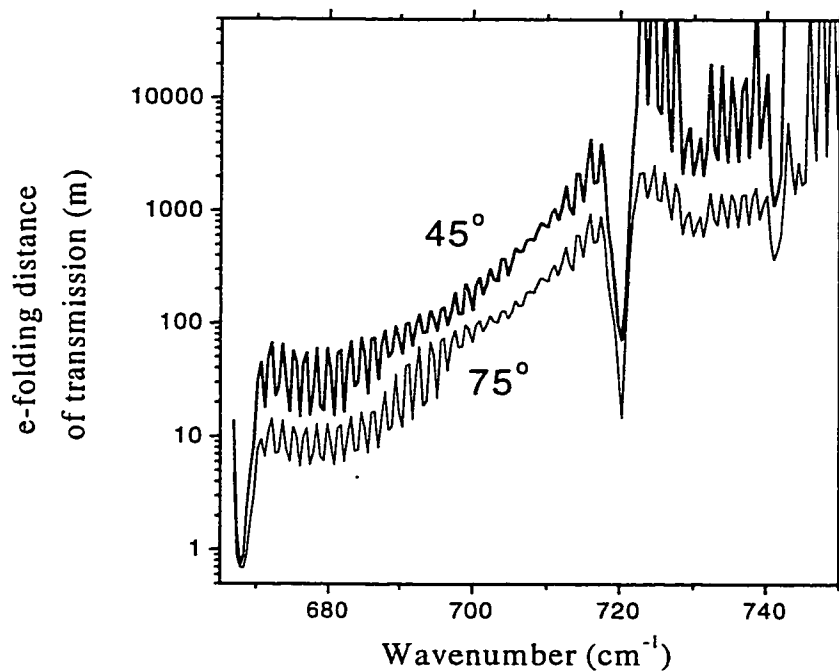


Figure 2.2: Variation in e-folding distances of transmission in the wing of the 15- μm CO_2 band, at viewing zenith angles of 45° and at 75° for a summertime Antarctic atmosphere. Moving from the center of the 15- μm band of CO_2 towards higher wavenumbers, the e-folding distance of transmission into the clear atmosphere generally increases. The average distance that a photon travels before being absorbed increases from a few tens of meters at around 670 cm^{-1} , to about 10 km at around 740 cm^{-1} . Radiance observed at the surface at these wavenumbers is therefore sensitive to clouds in the troposphere.

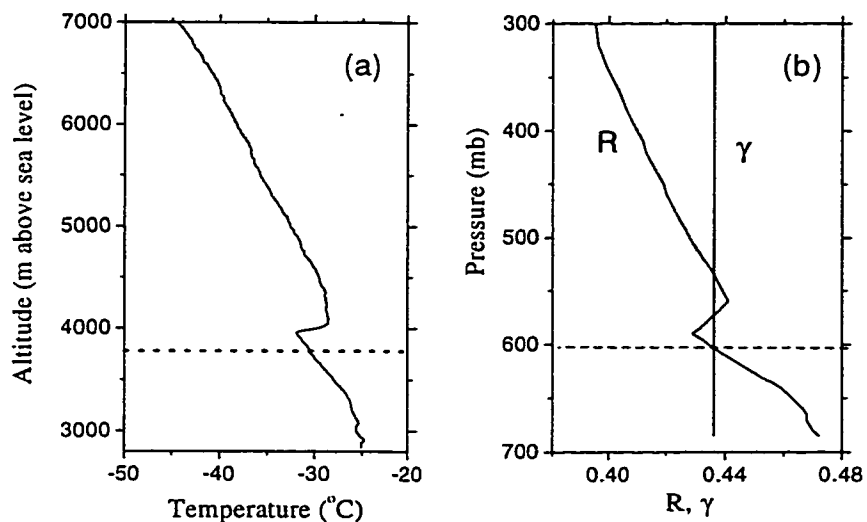


Figure 2.3: Determination of cloud base height in summer (January 26). (a) The radiosonde temperature profile suggests a cloud-top inversion 1200 meters above the surface. The cloud base height estimated by the SPWO (visual observation, indicated by dashed line) is shown. (b) R and γ , plotted against pressure, are shown at a representative wavenumber (715.6 cm^{-1}). The solution nearest to the surface (marked by the horizontal dashed line) is the cloud base height; the other two solutions correspond to points in the atmosphere at the same temperature, a condition that is caused by the putative cloud-top inversion.

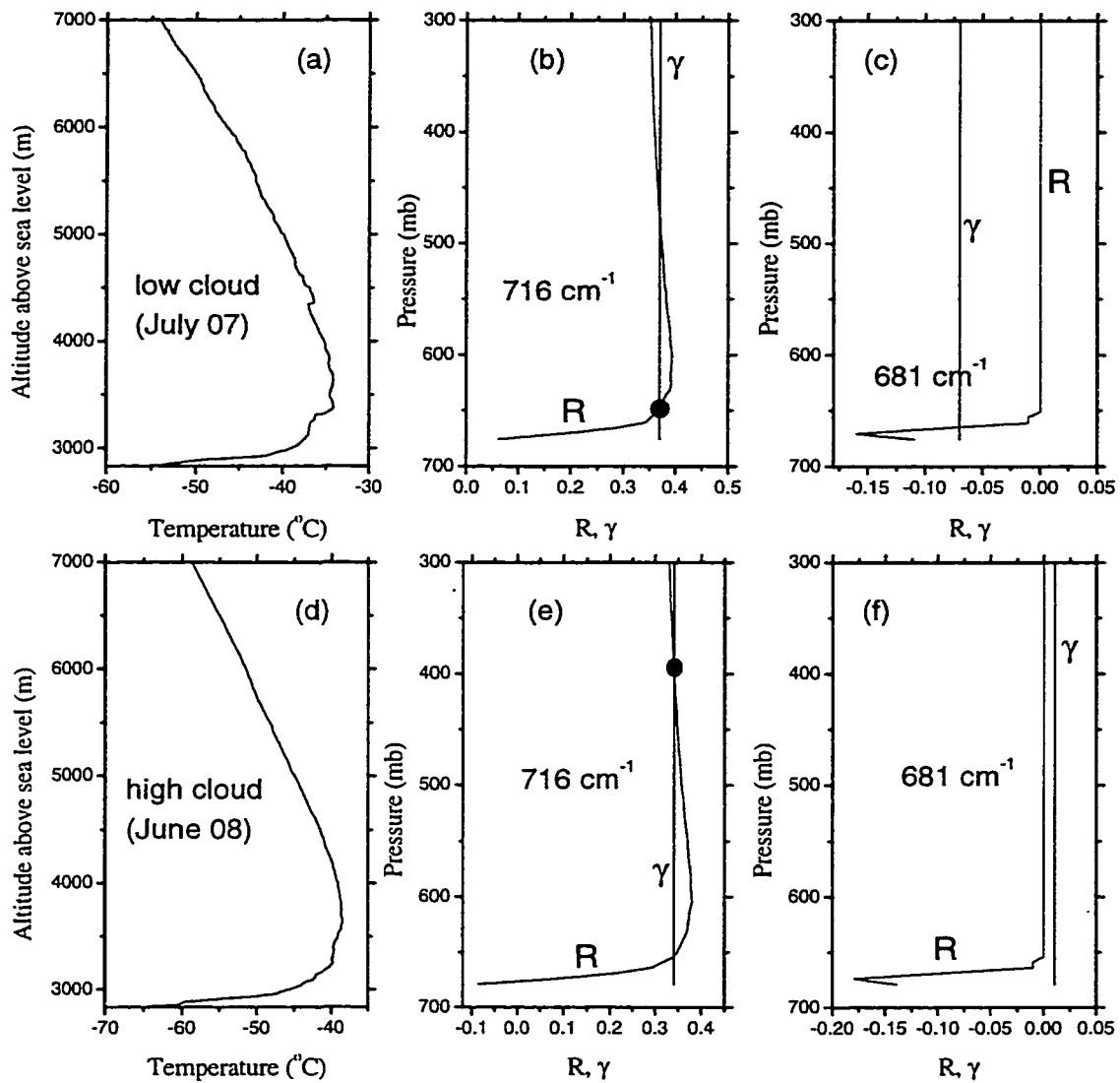


Figure 2.4: Determination of cloud base height in winter. Temperature profiles on two different days, one when the cloud base is estimated to be below the inversion (a) and the other when the cloud base is estimated to be above the inversion (d). Curves of γ and R , plotted against pressure, at a near-sighted wavenumber (680.9 cm^{-1}), as well as at a far-sighted wavenumber (715.6 cm^{-1}), are shown on the right. Only the July cloud is detectable at the near-sighted wavenumber; the June cloud is well beyond the e-folding distance of atmospheric transmission at this wavenumber. Both solutions are seen at the far-sighted wavenumber; depending on whether the cloud is detected at the near-sighted wavenumber, the appropriate solution (filled circle) is chosen at the far-sighted wavenumber.

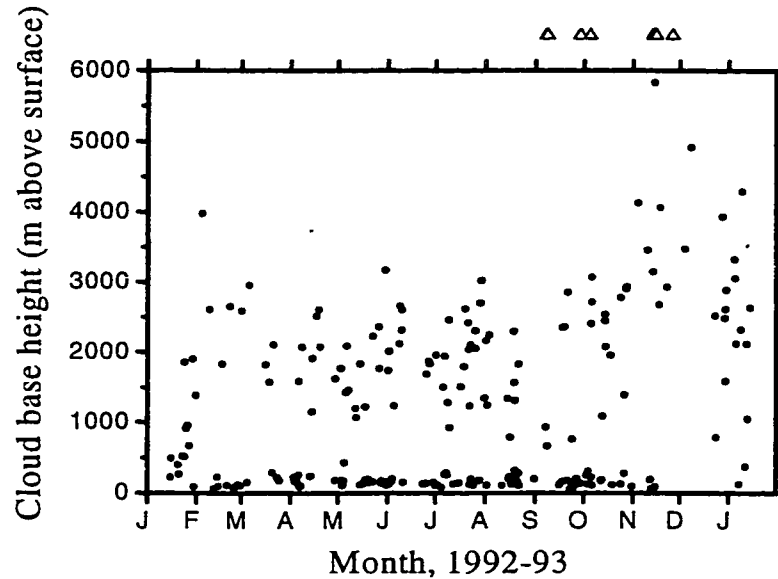


Figure 2.5: Cloud base heights shown at their times of observation during the year. Tick marks on the horizontal axis mark the beginning of each month. Cloud bases are higher in summer than in winter. The clouds were especially high during times when there was no surface-based inversion (Dec 1992). Polar stratospheric clouds (PSCs) can be detected by radiance-ratioing, but the method is not appropriate to locate their bases reliably. Observations of PSCs are shown as open triangles above the figure.

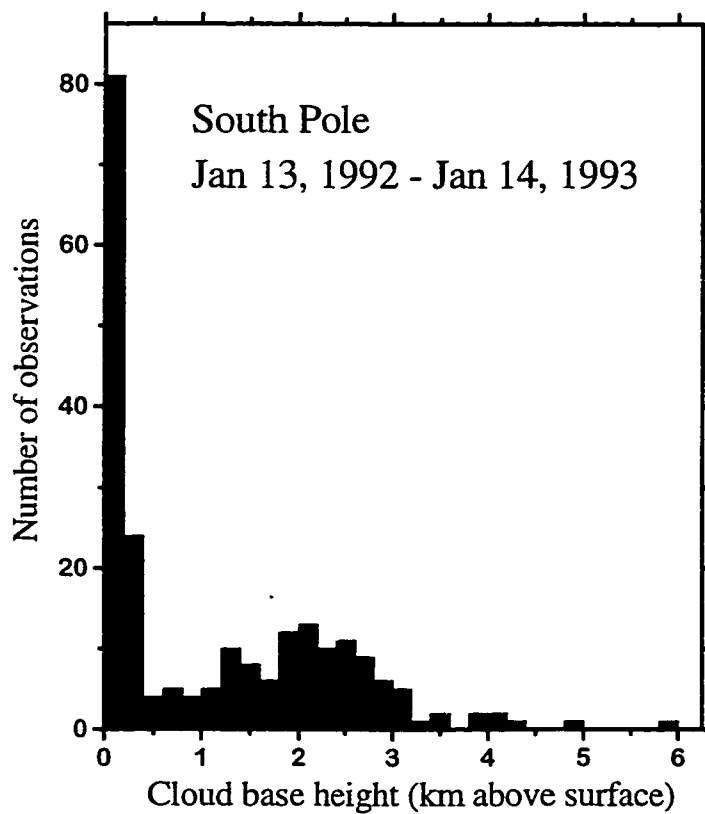


Figure 2.6: Histogram of cloud base heights at South Pole during 1992. A bimodal distribution of cloud heights is seen; many clouds have bases below the surface-based inversion, but another mode of higher clouds with bases 2-3 km above the surface is also seen.

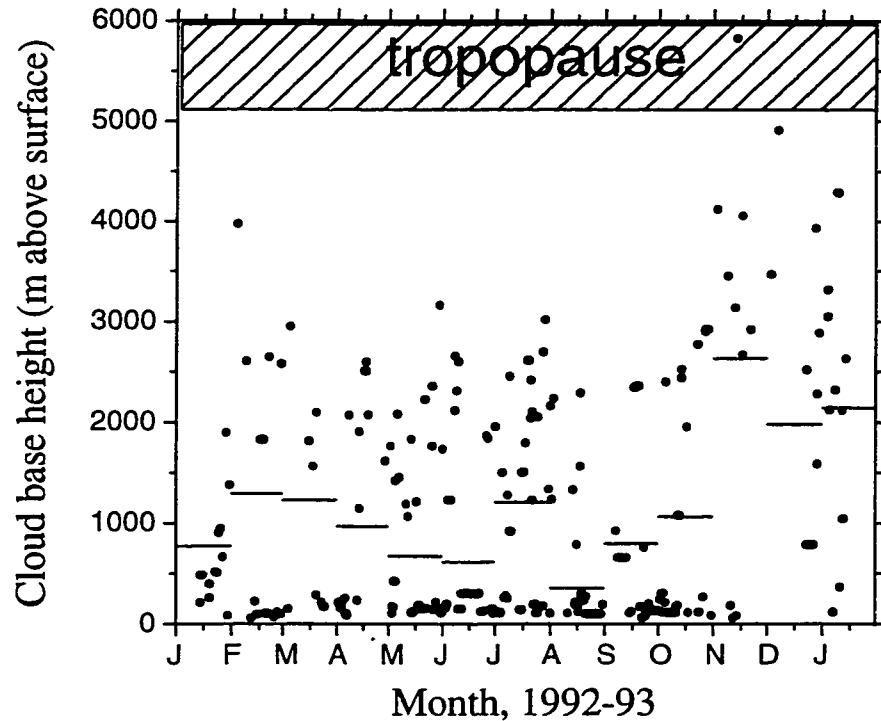


Figure 2.7: A one-year climatology of cloud base heights compiled using the values obtained by radiance ratioing, and by filling in missing values (using persistence) for times when the FTIR was not operating. Prolonged shut-down periods occurred only three times during the year; most of the time, missing values are at times when the nearest FTIR observation is only a day or two away. The dashed lines show monthly averages of cloud base heights.

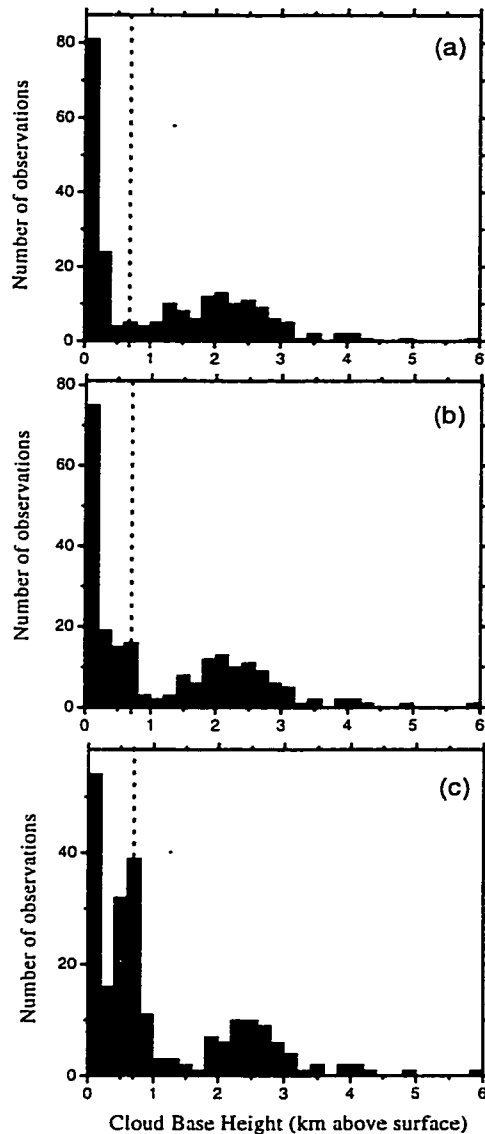


Figure 2.8: Tests to determine whether the bimodal distribution of cloud base heights obtained by radiance ratioing is real or an artifact. The first panel (a) is identical to Fig. 6, and shows the distribution of cloud base heights obtained from the spectral measurements. In (b), cloud base heights more than 200 meters above or below the top of the inversion, but at temperatures within 3K of the temperature at the top of the inversion, have been reset to the height of the inversion on that day. This creates new entries in the region of typical inversion height (600 - 700 m). (c) The condition for resetting the cloud base heights to the inversion heights is further relaxed to include clouds whose base temperature is within 6K of the inversion-top temperature. The bimodal distribution still persists, indicating that it is not an artifact of the radiance ratioing method. The vertical dashed line indicates the average height of the inversion-top.

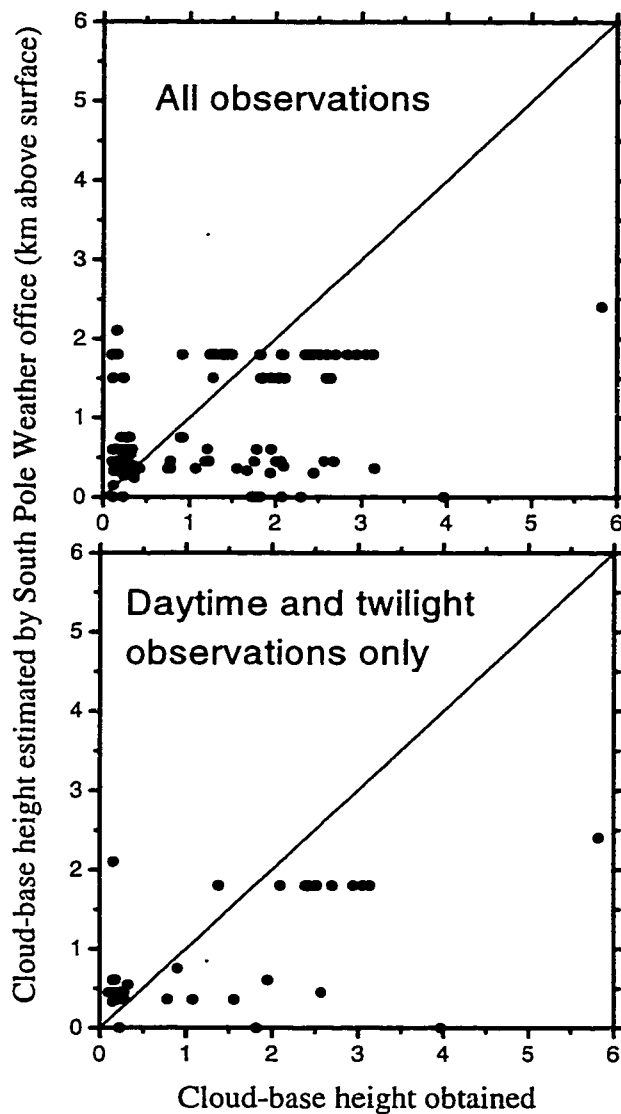


Figure 2.9: Estimates of cloud base heights made by the observers at the South Pole Weather Office (SPWO) compared to base heights derived by radiance ratioing. Comparisons were made only for those cases when the SPWO report was made within 2 hours of the FTIR measurement; in many cases, the weather office report is within half an hour of our measurement. The weather observers tend to underestimate the base heights of the high clouds, and overestimate the heights of the low clouds, relative to the base height inferred from radiance ratioing.

Chapter 3: Cloud Optical Depths and Particle Sizes

3.1 Introduction

The climate of the Antarctic Plateau, like everywhere else on Earth, is strongly affected by clouds, and the clouds are in turn affected by other meteorological variables. The radiative effects of clouds are determined by the clouds' vertical location, optical thickness, and particle sizes. Correspondingly, radiation measurements can be used to infer these properties, but they may not be uniquely obtained from such measurements directly because more than one combination of these cloud properties may produce the same radiance at any wavelength. Algorithms for the accurate determination of cloud properties therefore need to be developed and applied to radiation measurements.

In these papers (Parts I and II) we use longwave emission spectra measured at the surface to infer cloud base heights, optical thicknesses and particle sizes. Measurements made twice daily through one full year are used to obtain frequency distributions and seasonal cycles of these cloud properties. The measurements were made at only one location (South Pole Station), but because of the horizontal uniformity of the ice-sheet surface they are probably representative of a large area. We therefore offer them as a preliminary climatology of cloud properties for the East Antarctic Plateau, which should be useful for climate models of the Antarctic and surrounding regions (Simmonds 1990; Lubin et al. 1998). The determination of optical thicknesses and particle sizes is discussed in this paper (Part II); the method requires knowledge of the cloud base height, obtained from Part I (Mahesh et al. 1999).

The determination of particle sizes and optical depths uses three pieces of information: the transmittance of the cloud determined from spectral radiances in the 9.6- μm

ozone band, and cloud emissivities obtained at two microwindows near 10 and 11 μm in the atmospheric window. The first two sections describe the procedures to determine these quantities; these are followed by the algorithm to determine particle sizes and optical depths using both the emissivities and transmittances. A climatology of these properties is then presented, followed by a discussion of the findings. The particle sizes obtained from the spectral measurements are compared to values obtained from near-simultaneous photographs of falling ice crystals.

This study is related to others that develop remote sensing techniques using infrared spectral radiance measurements to determine cloud properties. A ground-based study of cirrus clouds was carried out in Wisconsin by Collard et al. (1995) during the First ISCCP Regional Experiment Phase II (FIRE II); as in this study, the authors used window radiances together with model calculations to obtain cloud particle effective radii. These techniques have also been applied to data from a coastal Antarctic station (Lubin 1994). A year-long climatology of cloud particle sizes and optical depths over the Antarctic Plateau has not previously been compiled, but short-duration studies have been conducted. Stone (1993) compared emissivities obtained from radiometer sonde data with theoretically computed values for model clouds with various particle sizes and ice water contents (IWCs), but his study was based on only eight observations of winter-time clouds. His calculations were made with cloud particles represented as spheres with surface areas equal to those of the ice crystals; he obtained particle radii of 4-16 μm and IWCs of 0.3-6 mg m^{-3} . Particle sizes have also been obtained previously from ice crystals collected over the plateau (Kikuchi and Hogan 1979), but these were limited to summer clouds.

3.2. Retrieval of Ozone-band transmittance

Ozone emission from above the cloud is often seen in our spectral measurements at the surface, since the cloud's optical thickness is usually not large enough to obscure this signal. Figure 3.1 shows a typical measurement sequence made under a cloud, in which emission from ozone above the cloud in the 9.6- μm band is detectable at the surface at all three viewing angles at which observations were made. At 45°, the ozone signal is much less attenuated than at 75°, since the path length through the cloud is much shorter at 45°, although the radiance itself is greater at the larger viewing angle because of cloud emission. Grund et al. (1990) showed that such incomplete attenuation of the ozone signal can be used to estimate cloud optical depths if one compares the ozone signal to the signal that would be recorded by the instrument in the absence of a cloud but under otherwise identical atmospheric conditions.

The radiance received by the interferometer can be expressed as a sum of six terms. Four of these represent contributions to the measured radiance from ozone, while the other two are independent of the ozone profile. Mathematically, this can be written as

$$\begin{aligned}
 I_{\text{obs}} = & \int_{P_s}^{P_B} B[T(p)] \frac{d}{dp} t(P, P_s) dp + r_c t(P_B, P_s) \int_{P_s}^{P_B} B[T(p)] \frac{d}{dp} t(P, P_B) dp \\
 & + t_c \int_{P_T}^0 B[T(p)] \frac{d}{dp} t(P, P_s) dp + \int_{P_B}^{P_T} t_o B[T(p)] \frac{d}{dp} t(P, P_s) dp \\
 & + \epsilon_c B(T_B) t(P_B, P_s) + r_c t^2(P_B, P_s) \epsilon_s B(T_s)
 \end{aligned} \tag{1}$$

where $t(P_x, P_y)$ is the transmittance from level x to level y , P_B is pressure at cloud base, P_T is pressure at cloud top, P_s is surface pressure, $B(T)$ is the Planck function at temperature T , ϵ_c is cloud emissivity, r_c is cloud-base reflectance, t_c is cloud transmittance, t_o is cloud transmittance for downward emission by in-cloud ozone, and ϵ_s is snow surface emissivity. The infrared emissivity of snow is greater than 0.98 in the 11- μm window, (Dozier and Warren 1982, Grenfell 1998). As a result, very little cloud radiance is reflected back and forth between the surface and the cloud base, and the contribution of multiple bounces to the observed downward radiance can be ignored.

The first term on the right side of Equation 1 is the downward emission by ozone in the atmosphere below the cloud. Part of the upward emission from this ozone is reflected downward by the cloud; this radiance is Term 2. The third term is the fraction of the emission from ozone above the cloud that is transmitted through the cloud to the surface. The fourth term is the emission from ozone within the cloud itself, the fifth term is the non-ozone contribution to radiance from the cloud (i.e. emission by ice crystals), and the sixth term is the portion of the upward radiance from the ground that is reflected back to the instrument by the cloud.

The vertical profile of ozone over the South Pole is measured at least once per week by ozonesondes throughout the year. During the spring, when the ozone concentration changes more rapidly, the sondes are launched every three days. If the cloud base height is known (from the method in Part I), then knowing the ozone concentration as a function of height, Term 1 can be calculated by radiative transfer modeling. Term 2 is usually at least an order of magnitude smaller than Term 1, since the reflectance of the

cloud at $9.6 \mu\text{m}$ is at most 2-3%. Term 1 represents only the contribution from ozone below the cloud. Ozone in the lower troposphere is less than 10% of the total column ozone and is usually much less because the clouds are low; we therefore ignore Term 2.

Terms 5 and 6 are independent of ozone, and along with Term 1, are part of the “background”; i.e., these are terms that would be observed even if the atmosphere above the cloud base contained no ozone. This background radiance can be estimated by interpolation from one side of the ozone band to the other. Brightness temperatures are computed across microwindows on either side of the ozone band. Microwindows are small spectral intervals in which there is negligible emission from atmospheric gases. The microwindows useful for background estimation are located at $950\text{-}970 \text{ cm}^{-1}$ on the small-wavenumber side of the ozone band, and $1118\text{-}1135 \text{ cm}^{-1}$, with a few exceptions, on the large-wavenumber side.); determining the brightness temperatures in these microwindows allows us to obtain the spectral signature of the cloud alone. These microwindows are chosen to be near the ozone band, so that cloud emissivity at these wavenumbers is nearly the same as the emissivity in the ozone band itself. The use of many wavenumbers in the microwindows reduces uncertainties in the brightness temperature resulting from noise in the spectral measurements.

The background radiances at wavenumbers within the ozone band are obtained by interpolating between the mean brightness temperatures in the microwindows on either side of the band. Means, rather than minimum values, are used because the minimum values include a bias towards low values due to instrumental noise. Also, interpolation in brightness temperatures, rather than interpolating radiance measurements directly, allows

the background to be drawn in such a way that any variation in emissivity across the ozone band is included in the calculation of the background.

If the atmosphere below the cloud base were isothermal and at the same temperature as the cloud base, then the absorption of cloud radiance by ozone below the cloud would be exactly balanced by emission from this same ozone, and the background radiance would include emission from ozone below the cloud (Term 1 in the above equation) exactly. However, the ozone below the cloud is actually distributed over a range of atmospheric temperatures, usually different from the cloud-base temperature. The background radiance obtained by interpolation, therefore, needs to be corrected. The emission from ozone below the cloud is calculated by radiative transfer modeling in two different ways, one using the actual vertical profile of temperature and another using an isothermal temperature profile with all temperatures set to equal the cloud base temperature. From the interpolated background radiance, the latter is subtracted and former is added back to give the true background.

Although we can determine the cloud base heights (by the radiance-ratioing method described in Part I), the cloud-top heights are unknown. However, this limitation is not serious, since tropospheric ozone is usually less than 10% of the total ozone. If all the ozone within the cloud were at the cloud base, then its emission would not be attenuated by the cloud. On the other hand, if all the ozone within the cloud were at the top of the cloud, then the attenuation of its emission would be similar to the cloud's attenuation of signals from other gases. We therefore assume that the transmittance of the cloud to emission by ozone within it lies half way between these extremes; i.e., in (1), we set

$t_o=(1+t_c)/2$. Since only a small part of the total ozone signal is derived from the troposphere, and the cloud thickness is only a fraction of the tropospheric thickness, emission from the ozone within the cloud is small, and the portion transmitted by the cloud can be adequately estimated using this assumption and any reasonable estimate of the cloud top height. Radiosonde data suggest that the cloud thicknesses are a few hundred meters to 2-3 kilometers, so for evaluation of Terms 3 and 4 we assume a cloud thickness of 1 km.

The integral calculations in Terms 3 and 4 can then be computed using a radiative transfer model. With the above assumption for t_o , the only unknown in (1) is the transmittance of the cloud. Collecting the terms in the background, we may write

$$I_{\text{obs}} - I_{\text{bkg}} = t_c \Sigma_3 + \left(1 + \frac{t_c}{2}\right) \Sigma_4 \quad (2)$$

where Σ_3 and Σ_4 are the integrands in Terms 3 and 4.

Equation (2) is solved for the transmittance (t_c) at several wavenumbers within the ozone band. Figure 3.2 illustrates the steps discussed so far. The three panels in this figure illustrate the determination of the brightness temperatures in the microwindows near the ozone band (3.2a), the interpolation of the background signal (3.2b), and the computed transmittances at different wavenumbers within the band (3.2c).

The transmission values show some variability over the range of wavenumbers at which they are calculated; this is due to the varying e-folding distance of transmission into the atmosphere at different wavenumbers within the band. Figure 3.3 shows the contribution of tropospheric ozone to the total clear-sky emission, calculated using the Line-By-Line-Radiative Transfer Model (LBLRTM, Clough *et al.* 1992) at viewing zenith angles

45° and 75°. Between 1025 and 1050 cm^{-1} , the e-folding distance is ~140 Dobson Units (DU); for 1000-1025 cm^{-1} , about 70 DU; and for 975-1000 cm^{-1} , about 3 DU (Houghton 1991). At 45°, tropospheric ozone contributes at most 10% of the total radiance at all wavenumbers within the band, whereas at 75°, only the wavenumbers in the far wings of the band meet this criterion. To minimize the uncertainty due to lack of knowledge of the cloud-top height, we estimate the transmittance of the cloud as the average value obtained at all wavenumbers at which tropospheric ozone contributes no more than 10% to the total ozone signal. At 45°, we use transmittance values near the center of the band (~1018-1040 cm^{-1}), but at 75° we use the longwave wing (1008-1020 cm^{-1}), and at 60° an intermediate set of wavenumbers. (The transmittances shown in Figure 3.2c are from measurements made at 45°).

3.3. Retrieval of window emissivities

Figure 3.4 shows absorption, scattering, and extinction efficiencies (Q_{abs} , Q_{scat} , and Q_{ext}) at six different microwindows in the 11- μm window region, over a range of particle sizes; these were computed using Mie theory (Wiscombe 1979; 1980) for ice spheres. The complex refractive index of ice was taken from Warren (1984). The microwindows were chosen at locations where absorption by gases is negligible. The absorption efficiency varies with cloud particle size at all wavenumbers, but is more sensitive at some wavenumbers than at others. At wavenumbers less than 900 cm^{-1} , Q_{ext} values do not suggest a unique particle size. Multiple solutions are not seen beyond 900 cm^{-1} , but Q_{ext} asymptotes to 2.0 very quickly, whereas at larger wavenumbers the Q_{ext} values asymptote more gradually, providing information to distinguish particle sizes. At all wavenumbers,

particle sizes larger than 30 microns cannot be distinguished. The ability to obtain unique solutions, as well as the two extremes of sensitivity to a broad range of particles (1-25 microns) are thus well represented at just the two microwindows at 903 and 988 cm^{-1} . Further, much of the variation in emissivity in the window (between 810 and 1000 cm^{-1}) occurs between these two wavenumbers at nearly all ice water paths (Figure 3.5), making these adequately representative of the variation in absorption by ice across the window.

Figures 3.6a and 3.6b show calculations of cloud emissivity at $\nu=903 \text{ cm}^{-1}$ and $\nu=988 \text{ cm}^{-1}$ in the 11- μm atmospheric window. Extinction efficiencies, single-scattering albedos, and phase function moments were calculated for ice spheres using Mie theory. Morley et al. (1989) had previously reported that clouds over the Antarctic Plateau were mostly made of ice particles. We verified this for our own observations using the trispectral method of Strabala et al. (1994), which clearly indicated that all our observations were of clouds consisting entirely or predominantly of ice. Cloud emissivities were computed using the Discrete Ordinates Radiative Transfer code (DISORT, Stamnes et al. 1988). Thermal emission radiances (I_{calc}) from clouds were computed using 40 streams in DISORT; the cloud emissivities were then computed using cloud base temperatures (T_c) obtained with information from Part I as

$$\varepsilon = \frac{I_{\text{calc}}}{B(T_c)} \quad (3)$$

However, I_{calc} includes not only emission from the cloud but also emission from the surface which is reflected back to the instrument by the cloud, and the emissivity obtained above is thus an “effective” emissivity, which includes reflection. Cloud reflectance in the infrared is typically less than 2%, but obtaining the emissivity by including

this additional radiance makes the calculations comparable to the measurements of downward radiance, which include reflection. For the DISORT computation the snow surface temperature was set equal to the cloud base temperature, but because of the small reflectance of the cloud this assumption does not significantly alter the results.

Mie and DISORT calculations were made for clouds with several different particle radii (r_{eff} between 0.5 and 100 microns) and many values of optical depth in the geometric-optics limit (τ_g between 0.01 and 100). The optical depth in the geometric-optics limit is chosen to describe the clouds because it is a quantity that is independent of wavenumber. For particle sizes greater than 5 μm , the emissivity at 903 cm^{-1} (ϵ_1) is insensitive to particle size, whereas at 988 cm^{-1} the sensitivity to particle size extends up to particles of $r_{\text{eff}}=25 \mu\text{m}$. This greater sensitivity to particle size is also true at wavenumbers within the 9.6- μm ozone band. Figure 3.6c shows that transmittance in the ozone band t_c is as sensitive to particle size as the emissivity at 988 cm^{-1} (ϵ_2). This variation in sensitivity with wavenumber means that the two desired quantities (r_{eff} and τ_g) can be inferred from the three measured quantities (ϵ_1 , ϵ_2 and t_c).

The computed emissivities and their difference ($\epsilon_1-\epsilon_2$) are shown as contour plots in Figure 3.7 over a range of cloud thicknesses (expressed either as optical depths or as ice water paths). For $r_{\text{eff}}>25 \mu\text{m}$, $\epsilon_1-\epsilon_2$ is negative; for $r_{\text{eff}}<25 \mu\text{m}$ it is positive. Over a range of particle sizes and geometric optical depths, the two emissivities together indicate specific particle radii and optical depths. Model computations of those quantities can then be compared to actual observations made under the cloud to obtain particle radii and geometric optical depths.

The effective emissivities at 903 cm^{-1} and 988 cm^{-1} are determined from the spectral radiance measurements and the cloud base temperature. To reduce the effect of random measurement errors, the emissivities ε_1 and ε_2 for each observation are obtained as averages over 3-cm^{-1} intervals centered at 903 and 988 cm^{-1} respectively, rather than at single wavenumbers. The temperature at cloud base is obtained from radiosonde data together with the cloud base heights determined in Part I.

3.4. Minimization routine

From each measured radiance spectrum, we obtain three different quantities, namely the effective emissivities at 903 and 988 cm^{-1} , and the transmittance t_c in the ozone band. These quantities can now be compared to corresponding values computed over a wide range of particle sizes and optical depths. This approach is similar to that used by Smith et al. (1993), but it uses fewer microwindows in the $11\text{-}\mu\text{m}$ atmospheric window than they used.

In the minimization algorithm, the emissivities and transmittance are weighted according to the reciprocal of the relative magnitude of their uncertainties. Uncertainty in cloud base height determined by radiance-ratioing propagates to uncertainty in cloud base temperatures, and thereby to uncertainty in emissivities determined at the two wavenumbers. Uncertainties in ozone-band transmittance also result from errors in spectral radiance measurements within the band, and from uncertainties in determining the emission from stratospheric ozone. Day-to-day variability in stratospheric ozone emission is nearly constant at about $1\text{ mWm}^{-2}\text{sr}^{-1}(\text{cm}^{-1})^{-1}$ (1 radiance unit; RU) throughout the year (Figure 3.8). However, the monthly average emission undergoes a large seasonal cycle, ranging

from 16-18 RU in summer to 5 RU in winter and spring. As a result, the uncertainties in ozone transmittance values due to uncertainty in the ozone profile are larger in the winter and spring (~20%) than in the summer and autumn (<10%).

Uncertainties in the emissivities were estimated to be typically 5-8% of the emissivity values themselves; these result mostly from uncertainties in cloud base temperature and uncertainties due to measurement error. Uncertainties in the measured radiances were determined by Walden (1995). Errors in cloud base temperature correspond primarily to errors in cloud base heights, which are estimated in Part I. Both sources of uncertainty are, however, correlated across the window region; i.e., errors in ε_1 are correlated with errors in ε_2 . As a result, the difference $\Delta\varepsilon=(\varepsilon_1-\varepsilon_2)$ can be estimated more accurately than ε_1 or ε_2 . The algorithm to minimize the differences between observations and calculations takes advantage of this.

The quantities ε_1 , $\Delta\varepsilon$, and t_c from the observations form a 3-element vector that is compared to corresponding vectors calculated for all possible combinations of r_{eff} and τ_g . The quantities are then weighted according to their relative accuracies; $\Delta\varepsilon$ is weighted 5 times as much as ε_1 . The relative accuracy of ε_1 and t_c is determined as follows. The emissivity at 903 cm^{-1} depends on the assumed cloud base temperature; uncertainties in this quantity result from uncertainties in the temperature. The cloud base temperature is perturbed by its estimated uncertainty of 3K, and the corresponding change in ε_1 is determined. The transmittance in the ozone band is most sensitive to day-to-day variation in stratospheric ozone emission. For each observation made under cloudy skies, the uncertainty in transmittance due the variability in stratospheric ozone emission is determined.

Uncertainties in ϵ_1 and t_c are then compared and assigned relative weights. The combination of particle radius and geometric optical depth is chosen such that the difference in the measured and calculated values of ϵ_1 , $\Delta\epsilon$ and t_c are minimized. The values of particle radius and geometric optical depth are determined at all viewing angles; when the same cloud is seen at more than one viewing angle, the angle at which the transmittance is closest to 0.5 is used to obtain the best accuracy.

3.5. Results

Figure 3.9 shows the cloud optical depths and ice water paths (IWP) obtained throughout the observation period; Figure 3.10 shows histograms of the same quantities. These are related by

$$\tau_g = \frac{3}{2} \frac{\text{IWP}}{r_{\text{eff}} \rho_{\text{ice}}}, \quad (4)$$

where ρ_{ice} is the density of pure ice, 917 kg m^{-3} . Optical depths are shown for all observations in which clouds were detected, but ice water paths are shown only for those observations in which both particle size and optical depth could be determined. This was possible in three-fourths of the observations; in other cases, only a lower limit to either the optical depth or particle size could be obtained. Fewer than 10% of the clouds have $\tau_g > 5$, and about two-thirds have $\tau_g < 1$.

Stone (1993) obtained similar values from radiometersonde measurements of upward and downward fluxes at the South Pole. He determined cloud-top and base heights of eight winter-time clouds from vertical profiles of flux and temperature. Stone then estimated the emissivity and optical depths of the clouds by comparing the observa-

tions to model comparisons made at 10.8 μm wavelength; he found the average emissivity to be 0.6, and the average optical depth to be 1.0. However, the values obtained from those measurements had large uncertainties (up to 30%). Stone's model calculations, which used equal-surface-area spheres, implied particle radii from 4 to 16 μm (consistent with our results shown below), and IWCs of 0.3 to 6 mg m^{-3} .

We considered the possibility that the smallest optical depths we obtain may in fact be of Pinatubo aerosol rather than clouds, but rejected it. The infrared optical depths of stratospheric aerosol are between a quarter and half of the visible optical depths (Lacis et al. 1992), which through most of 1992 were around 0.1 or less; measurements of aerosol under cloud-free conditions lie within our threshold for cloud detection (optical depth of 0.06 or less, see paper I, this issue).

Figure 3.9 shows that clouds with $\tau_g > 2$ are seen more often in winter than in summer. Thin clouds ($\tau_g < 2$), on the other hand, are seen during all months. As expected, these clouds are much thinner than clouds at the coast of Antarctica. Ricchiuzzi et al. (1995), using solar irradiance data from a ground-based multi-channel radiometer, found $\tau_g \sim 20$ for clouds at Palmer Station (65° S, 64° W). Such clouds are effectively semi-infinite in the infrared; our methods would therefore not be appropriate for determining their optical thicknesses.

The effective particle radii r_{eff} obtained from the spectral measurements are shown in Figure 3.11; a histogram of these values is shown in Figure 3.12. The median value of r_{eff} is 15.2 μm . As suggested by Figure 3.7, when $r_{\text{eff}} > 25 \mu\text{m}$ an accurate determination of r_{eff} is not possible, so only a lower limit is indicated in these cases. Approximately 20% of

the clouds have retrieved $r_{\text{eff}} > 25 \mu\text{m}$. Clouds with $r_{\text{eff}} > 25 \mu\text{m}$ are rarely seen in winter, and clouds with $r_{\text{eff}} < 10 \mu\text{m}$ are rarely seen in summer. Lubin and Harper (1996) determined effective radii using AVHRR channels at 11 and 12 μm , and like us found summer crystals to be larger than those in the winter. However, the values they obtained (mean r_{eff} of 12.3 μm in summer, and 5.6 μm in winter) are smaller than the r_{eff} we obtain. Precipitating ice crystals in summer were measured at South Pole Station by Kikuchi and Hogan (1979). For the 1200 crystals they sampled, the average c-axis length was 90 μm , and the ratio c/a typically varied between 2.5 and 5.5.

Uncertainties in the emissivities at 903 and 988 cm^{-1} and transmittance in the ozone band produce uncertainties in the derived particle radius and optical depth. The uncertainties in the emissivities and transmittance were estimated and the particle radius r_{eff}' and optical depth τ_g' were computed after the values of ϵ_1 , ϵ_2 and t_c were perturbed by these uncertainties, and compared to r_{eff} and τ_g respectively. The resolution of r_{eff} and τ_g were then determined as $\ln(r_{\text{eff}}/r_{\text{eff}}')$ and $\ln(\tau_g/\tau_g')$ respectively; these are shown in Figure 3.13. Smaller particle sizes are generally more reliably determined than larger particle sizes; this is expected from Figure 3.6, which shows that particle radii larger than 25 microns cannot be distinguished. Optical depths are not very sensitive to errors in emissivity and t_c ; over a broad range of cloud optical thicknesses τ_g can be reliably determined.

Figure 3.14 shows a comparison of particle sizes and optical depths obtained for the same cloud at two different viewing angles. As expected, the agreement for particle sizes greater than 20-25 μm is poor, whereas smaller particle sizes determined at different viewing angles are quite similar. The values can also be different if two different clouds at

different heights are being viewed at the two angles.

3.6. Comparison with independent observations

3.6.1. Crystal sizes

Atmospheric ice crystals falling onto a gridded slide were collected at South Pole Station for 100 days from June to October 1992, and photographed under a microscope; an example is shown in Figure 3.15. The photographs were then scanned and digitized for interactive computer analysis. Dimensions of 14,000 crystals were measured, and their surface areas and volumes were determined. For each crystal, “equivalent spheres” were determined using three different prescriptions: equal surface area, equal volume, and equal volume-to-area ratio (V/A). The third prescription is advocated by Grenfell and Warren (1999); it conserves both total area and total volume of ice in the cloud, but does not conserve particle number. The size distribution of ice crystals in each photograph was then used to obtain three values of r_{eff} , which are compared in Figure 3.16 to the particle radii obtained from spectral measurements. On average, the remotely-sensed radius agrees with the equal- V/A prescription, whereas the equal-volume and equal-area radii are much too large. However, the radii from the photographs are not correlated with the remotely-sensed radii. This may be due to the difference of 2-6 hours between the time the crystals were collected and the time the spectral measurements were taken. The average r_{eff} from the photographs ($17.4 \mu\text{m}$) is also seen to be slightly larger than the average remotely-sensed r_{eff} ($15.2 \mu\text{m}$). This bias is consistent with the expectation that the crystals must grow large enough to attain a significant fall-speed before they can be collected at the surface, and therefore the crystals collected will be somewhat larger than the average size of

crystals remaining in the cloud. The average r_{eff} is surprisingly close to that we obtain from analysis of Kikuchi and Hogan's (1979, Figure 7) scatter-diagram of a-axis and c-axis lengths, $r_{\text{eff}} = 17.5 \mu\text{m}$.

3.6.2. Cloud types

A scatter diagram of cloud optical depths and base heights is shown in Figure 3.17, where the base heights were obtained from Part I. Low clouds are distributed across all optical depths, but high clouds are typically thin. Almost all the clouds with $\tau_g > 2$ had bases below 300 m.

Visual cloud observations are made every six hours throughout the year by personnel of the South Pole Weather Office, and reported in the standard synoptic code (WMO, 1974). The reports of cloud types can be compared to our retrieved base heights and optical thicknesses. They are in general agreement, in that the optically thicker clouds are usually reported as nimbostratus (Ns), and clouds with the highest retrieved bases are reported as cirrus (Ci) or cirrostratus (Cs). Stratus (St) clouds tend to be reported as low, while altostratus (As) and altocumulus (Ac) are intermediate in height (other cloud types are less common). However, it is noteworthy that these cirrus clouds over the Antarctic Plateau are much lower than cirrus elsewhere, being only 1-6 km above the surface (4-9 km above sea level). This is consistent with the low tropopause height of 8-9 km above sea level (Warren 1996).

3.7 Conclusions

Cloud optical thickness over the Antarctic Plateau is considerably less than on the coast. Whereas clouds on the coast typically have optical depths of 20 or more, nearly

two-thirds of the clouds detected at the South Pole have optical depths of 1 or less. Effective cloud particle radii could be estimated in 80% of the observations; in the remaining 20%, only a lower limit of 25 μm could be established. The median effective particle radius is found to be 15.2 microns. Seasonal variations in particle radii are seen, with larger particle sizes recorded almost exclusively in the summer and smaller ones mostly in the winter months. Particle radii obtained from the spectral measurements are comparable to those obtained from photographs of falling ice crystals if each crystal is represented by a collection of spheres of the same surface-to-volume ratio as the real crystal.

Acknowledgments. Elizabeth Tuttle analyzed the photographs of falling ice crystals and measured the dimensions of each crystal. NOAA-CMDL provided ozonesonde data, and the South Pole Weather Office provided radiosonde data and synoptic cloud reports. We thank Steven Neshyba and Qiang Fu for helpful discussions, and Tom Grenfell and Norman McCormick for reading a draft of this publication. This research was supported by NSF grants OPP-94-21096 and OPP-97-26676.

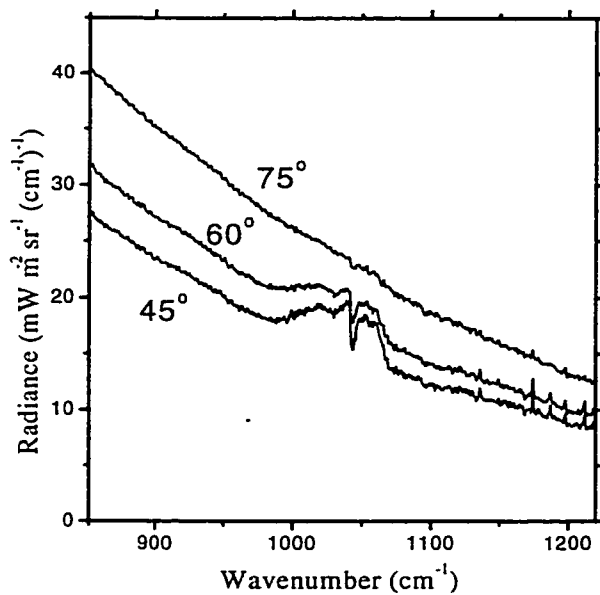


Figure 3.1: Spectral radiance measurements in the 9.6- μm band of ozone made under a cloud on November 22, 1992, at three different viewing zenith angles. At larger viewing zenith angles, the radiance from the cloud is greater, but the signal of the overlying ozone emission is reduced by the increased path length through the cloud.

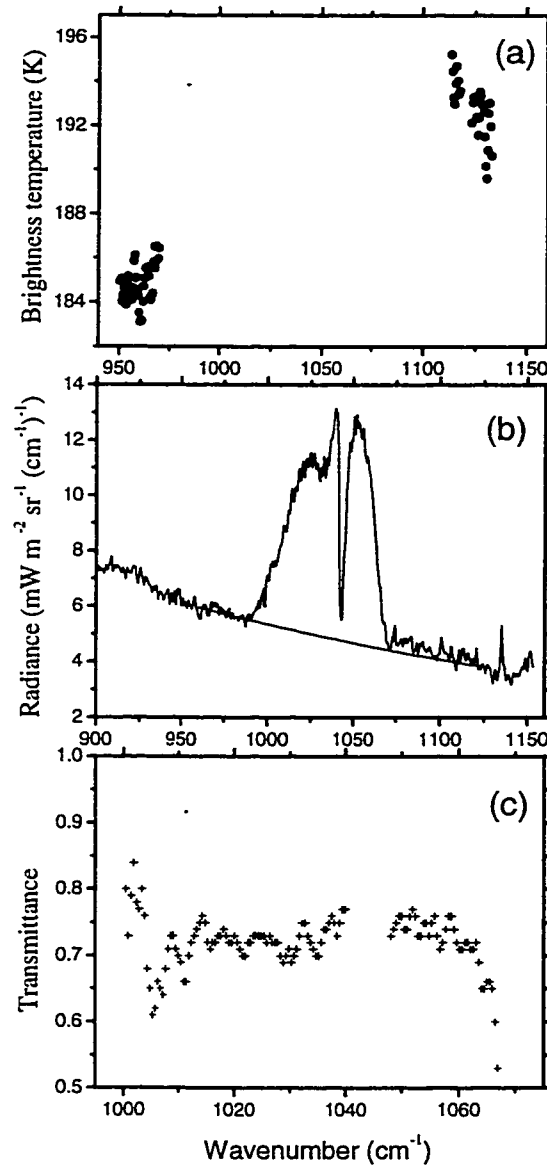


Figure 3.2: Steps in determining transmittance from radiance measurements made on April 14 at 1200 GMT, at a viewing angle of 45° . (a) Brightness temperatures are calculated in microwindows on either side of the ozone band. (b) The background radiance from non-ozone sources is estimated by interpolating across the band using the brightness temperatures. (c) After subtracting out the contributions of ozone above and below the cloud, the transmittance of the cloud is estimated at numerous wavenumbers within the band.

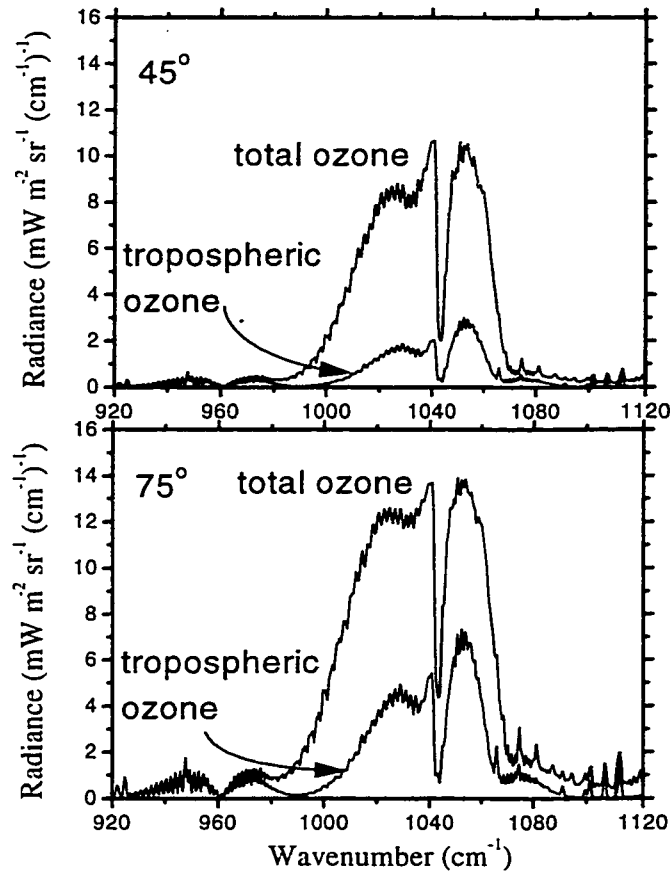


Figure 3.3: Contribution of tropospheric ozone to downward radiance at the surface, computed by LBLRTM. Tropospheric ozone is usually less than 10% of the total ozone in the atmosphere. At small viewing angles, the tropospheric contribution to the total radiance at all wavenumbers in the 9.6- μm band remains below 10%. But at larger viewing angles, the differences in atmospheric transmission between wavenumbers in the band become more important. At wavenumbers near the center of the band, where atmospheric opacity is greater, nearly a third of the ozone signal is from the troposphere. But near the edges of the band, at the more far-sighted wavenumbers, tropospheric contributions are still small.

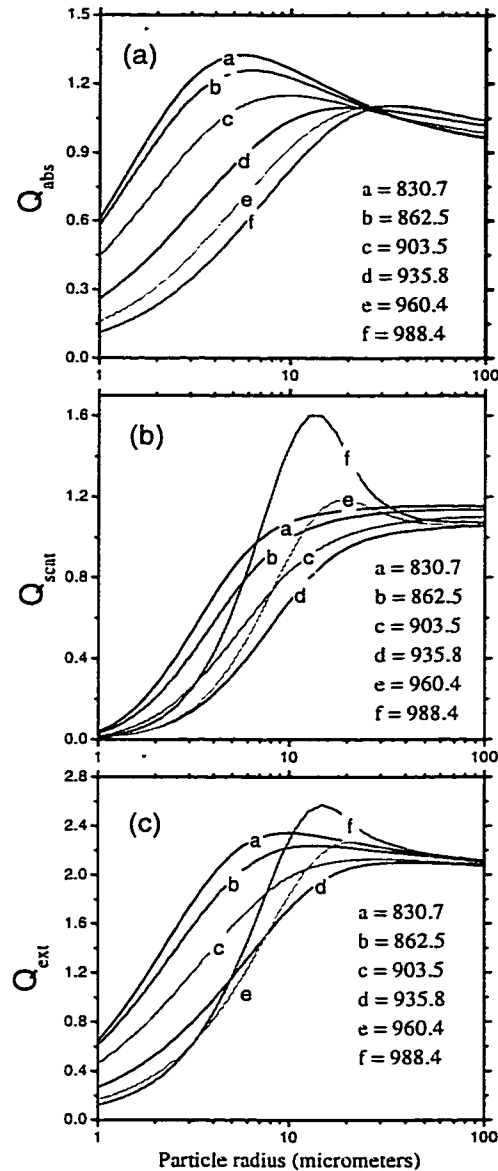


Figure 3.4: (a) Absorption efficiency (Q_{abs}), (b) scattering efficiency (Q_{scat}) and (c) extinction efficiency (Q_{ext}) as a function of cloud particle size at six different microwindows (labeled a through f, in cm^{-1}) in the $11\text{-}\mu\text{m}$ window region, shown over a range of cloud particle sizes. Variation in Q_{abs} with particle size is necessary to determine the cloud particle effective radius; although there is sufficient variation at all wavenumbers to distinguish particle radii less than 10 microns, it is only at 988 cm^{-1} that variation in Q_{abs} continues to radii of 20-30 microns.

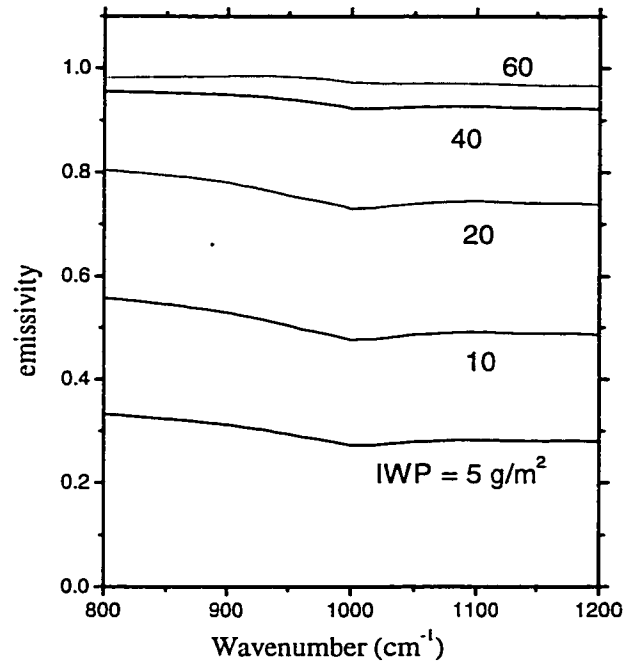


Figure 3.5: Spectral emissivity for ice clouds between 800 and 1200 cm⁻¹, computed for several values of cloud ice water path.

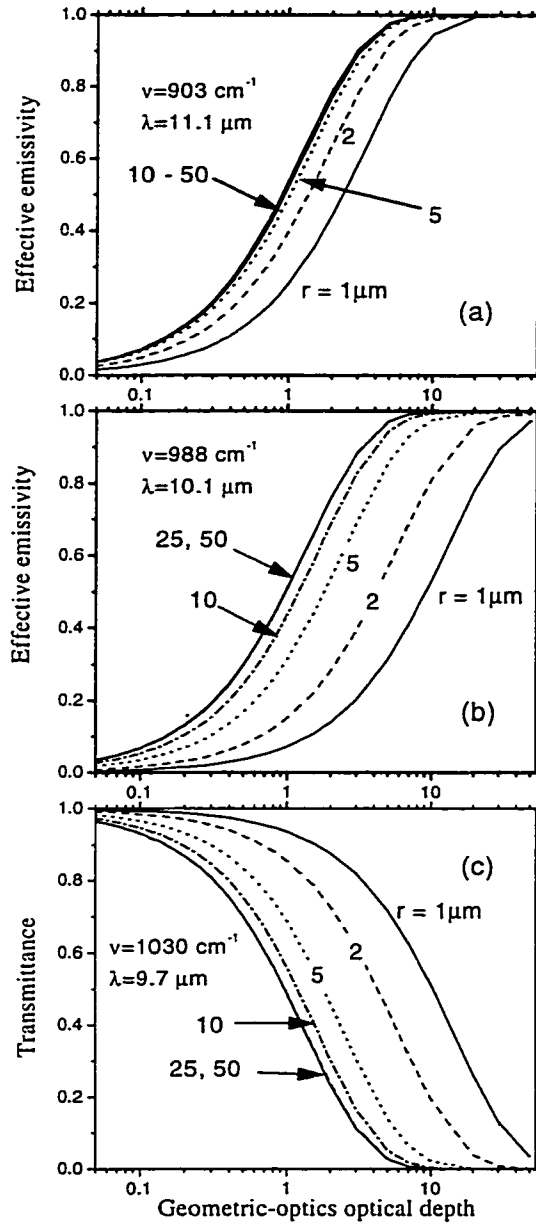


Figure 3.6: Contours of (a) cloud effective emissivity at 903 cm^{-1} , (b) cloud effective emissivity at 988 cm^{-1} , and (c) cloud transmittance in the $9.6\text{-}\mu\text{m}$ ozone band for different particle sizes, computed using Mie theory and DISORT. In each case, six different curves are shown, at particle radii from 1 to $50 \mu\text{m}$.

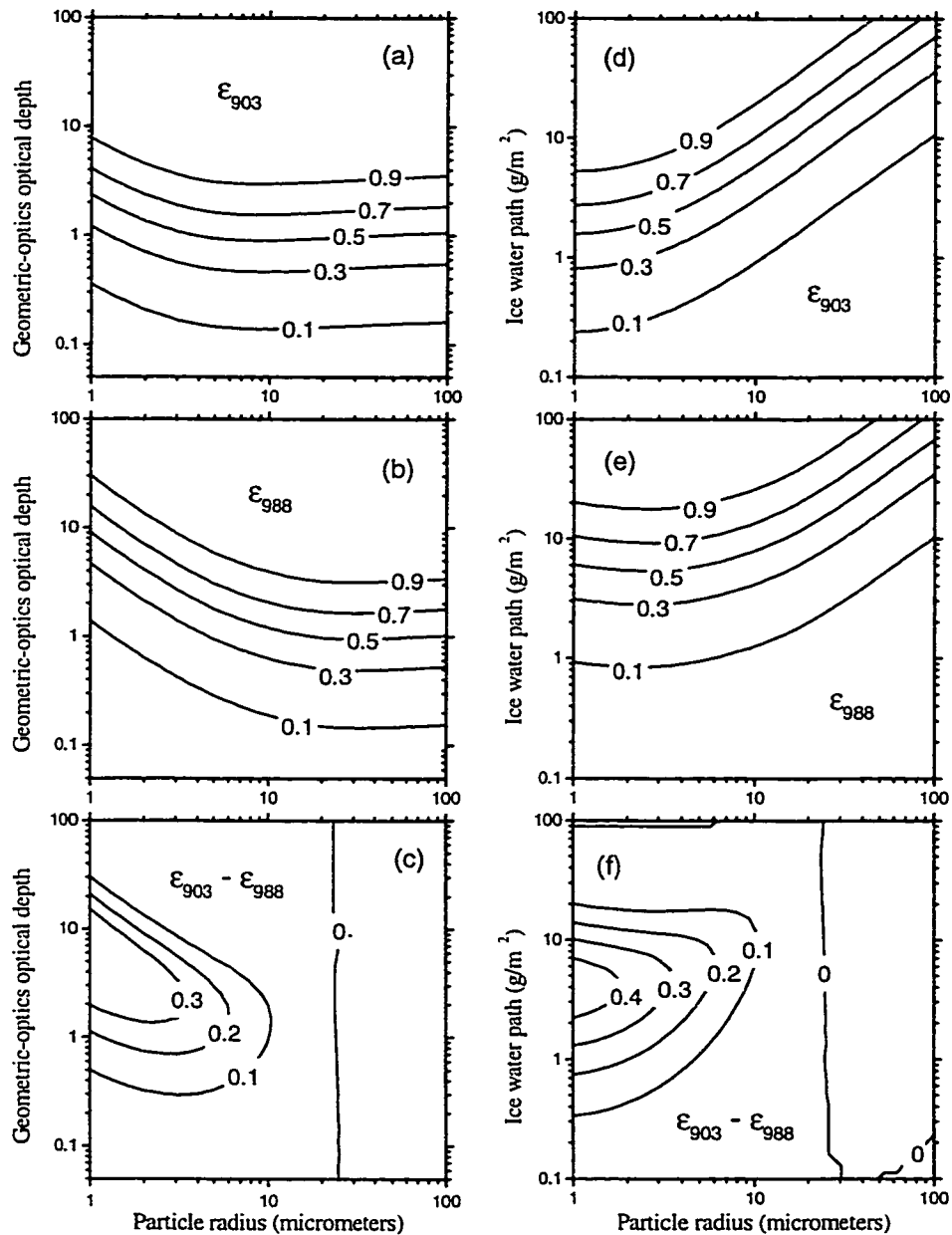


Figure 3.7: Emissivities at 903 cm^{-1} and 988 cm^{-1} , plotted as functions of particle radius and either cloud optical depth (left) or ice water path (right). The difference in emissivities at these two microwindows is also shown (c,f). A negative or zero emissivity-difference implies particle radius greater than 25 microns, whereas a positive difference implies smaller particles.

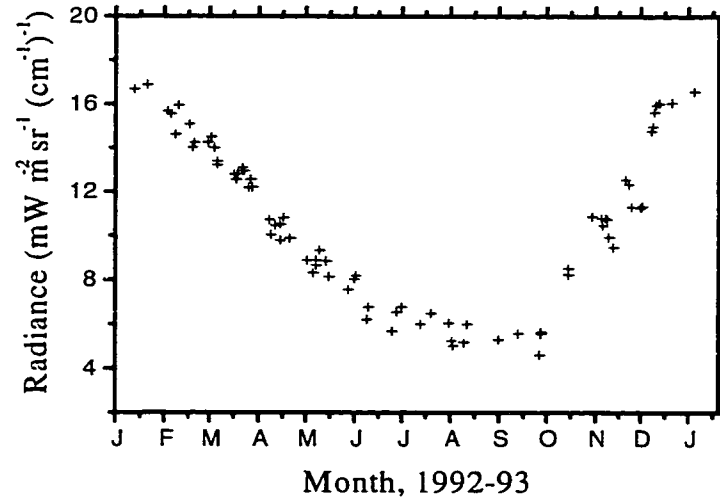


Figure 3.8: Clear-sky radiances in the 9.6- μm ozone band are shown for $\nu=1035\text{ cm}^{-1}$. The values range from summertime highs of around $17\text{ mWm}^{-2}\text{sr}^{-1}(\text{cm}^{-1})^{-1}$ (Radiance Units; RU) to spring-time lows of 4-6 RU. Day-to-day variability in the ozone emission is about 1 RU throughout the year, leading to greater winter- and spring-time uncertainties in ozone-transmittance.

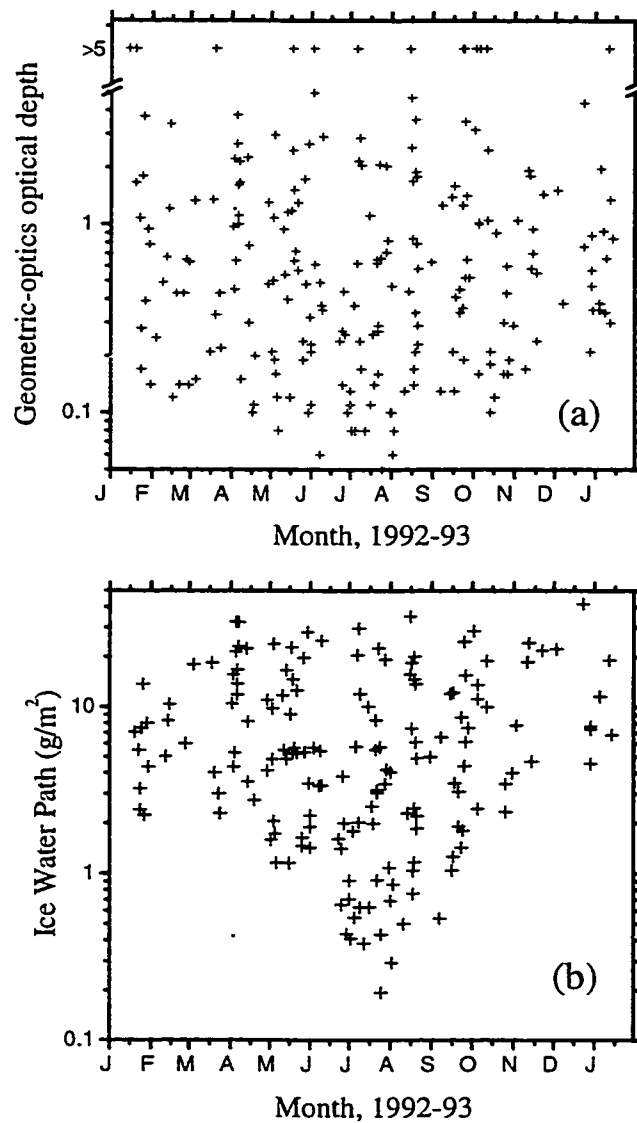


Figure 3.9: Cloud optical depths in the geometric-optics limit (upper), and ice water paths (lower) at South Pole during 1992-93. Tick marks indicate the beginning of each month. Both thick and thin clouds are observed during all seasons. Optical depths are not uniquely determined for extremely thick clouds ($\tau_g > 5$); for these cases, only a lower limit is indicated. Ice water paths are shown only for cases where both the optical depth and the particle radii were uniquely determined; about 75% of the observations met this criterion.

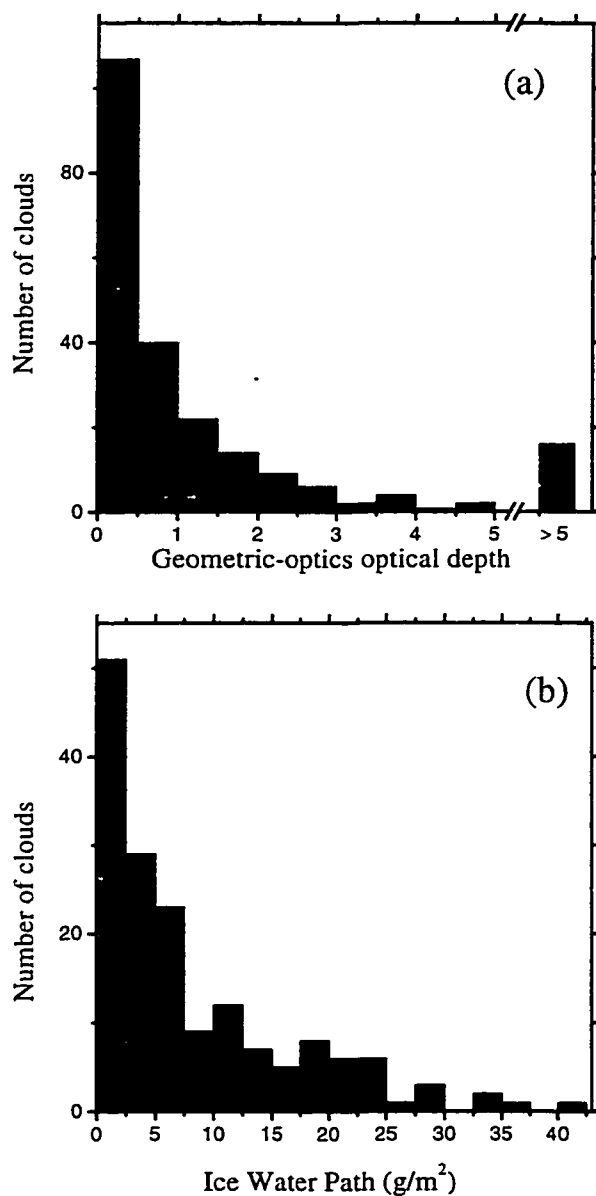


Figure 3.10: Histograms of (a) optical depth and (b) ice water path at South Pole during 1992. Roughly 5% of the clouds had optical depths too large to be uniquely determined ($\tau_g > 5$). Approximately 65% of the clouds have $\tau_g < 1$. Ice water paths are shown only for those cases where both particle size and optical depth could be uniquely determined; about 75% of the observations met this criterion.

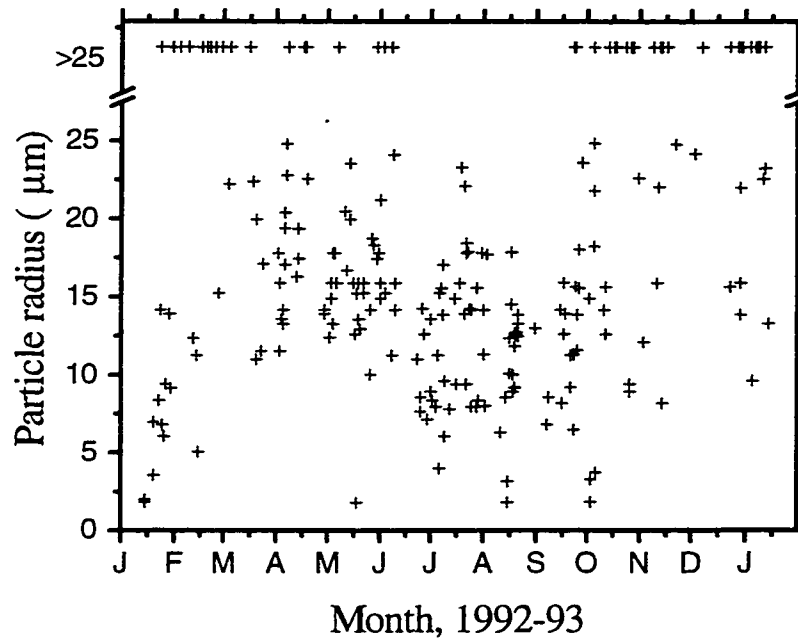


Figure 3.11: Effective particle radii r_{eff} for clouds over the South Pole during 1992-93. Large particle radii are observed mostly in the summer; for the four winter months June-September, no clouds were observed with $r_{\text{eff}} > 25 \mu\text{m}$. Particle sizes greater than $25 \mu\text{m}$ are not accurately determined; for these clouds, only a lower limit to r_{eff} is indicated.

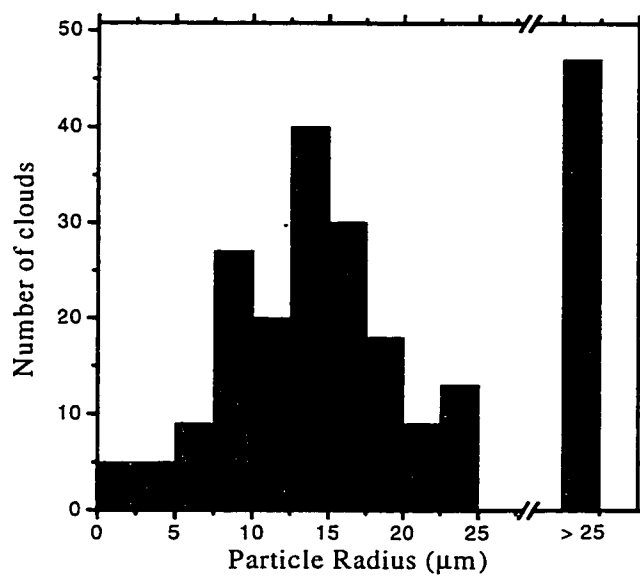


Figure 3.12: Histogram of effective radii obtained at South Pole during 1992. The median particle size is $15.2 \mu\text{m}$. For $r_{\text{eff}} > 25 \mu\text{m}$, only a lower limit to r_{eff} is determined.

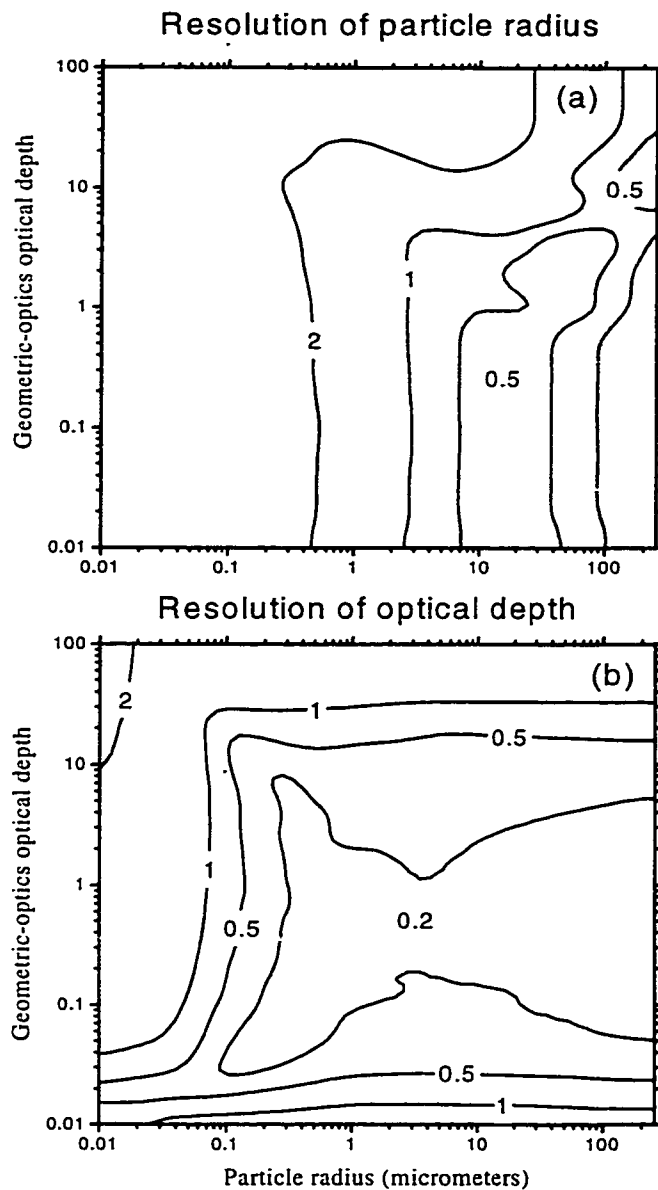


Figure 3.13: Relative uncertainty in determination of (a) particle radius and (b) optical depth due to uncertainty in estimation of window emissivities and ozone-band transmittance. For a specified (τ_g, r_{eff}) combination, emissivities (ϵ_i) and transmittance (t) were calculated; they were perturbed to ϵ_i' and t' using estimated uncertainties in measured radiance and temperature. These perturbed values ϵ_i' and t' were used to infer cloud properties $(\tau_g', r_{\text{eff}}')$. The contours plotted are of $\ln(r_{\text{eff}}'/r_{\text{eff}})$ and $\ln(\tau_g'/\tau_g)$.

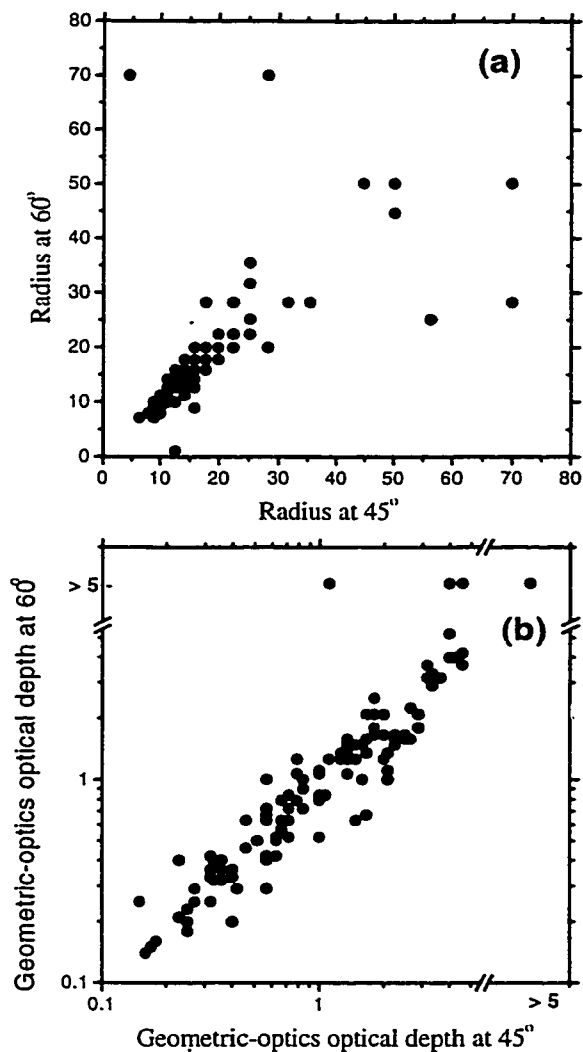


Figure 3.14: Comparison of particle sizes and optical depths obtained at two different viewing angles (45° and 60°), for all observations in which the same cloud was seen at both angles.



Figure 3.15: Photograph of falling ice crystals at South Pole, taken under a cloud on July 5, 1992. These particles were scanned and digitized, and their surface areas and volumes were computed so that they could be related to equivalent spheres of equal area ($r_A=28 \mu\text{m}$), equal volume ($r_V=21 \mu\text{m}$) and equal volume-to-area ratio ($r_{VA}=16 \mu\text{m}$). All three values are larger than the particle radius obtained from the spectral measurement from that day ($11.3 \mu\text{m}$), but r_{VA} is closest.

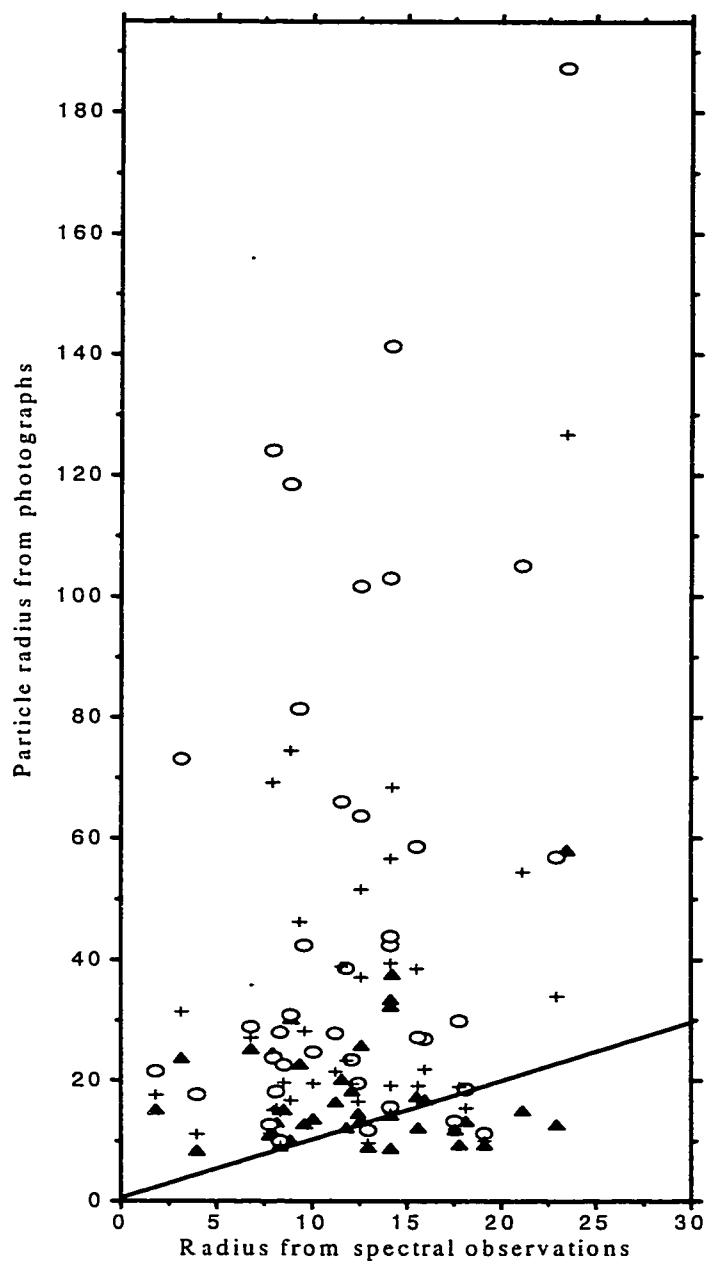


Figure 3.16: Comparison of particle sizes obtained from spectral measurements with those obtained from photographs. The equivalent spherical radius for each crystal observed in the pictures was obtained in three different ways, (a) open circles indicate the effective radii of spheres with identical surface areas to the crystals observed, (b) plus signs (+) indicate the effective radii of spheres with identical volumes, and (c) solid triangles indicate the effective radii of spheres with identical surface-to-volume ratios. The solid straight line shows a slope of 1.

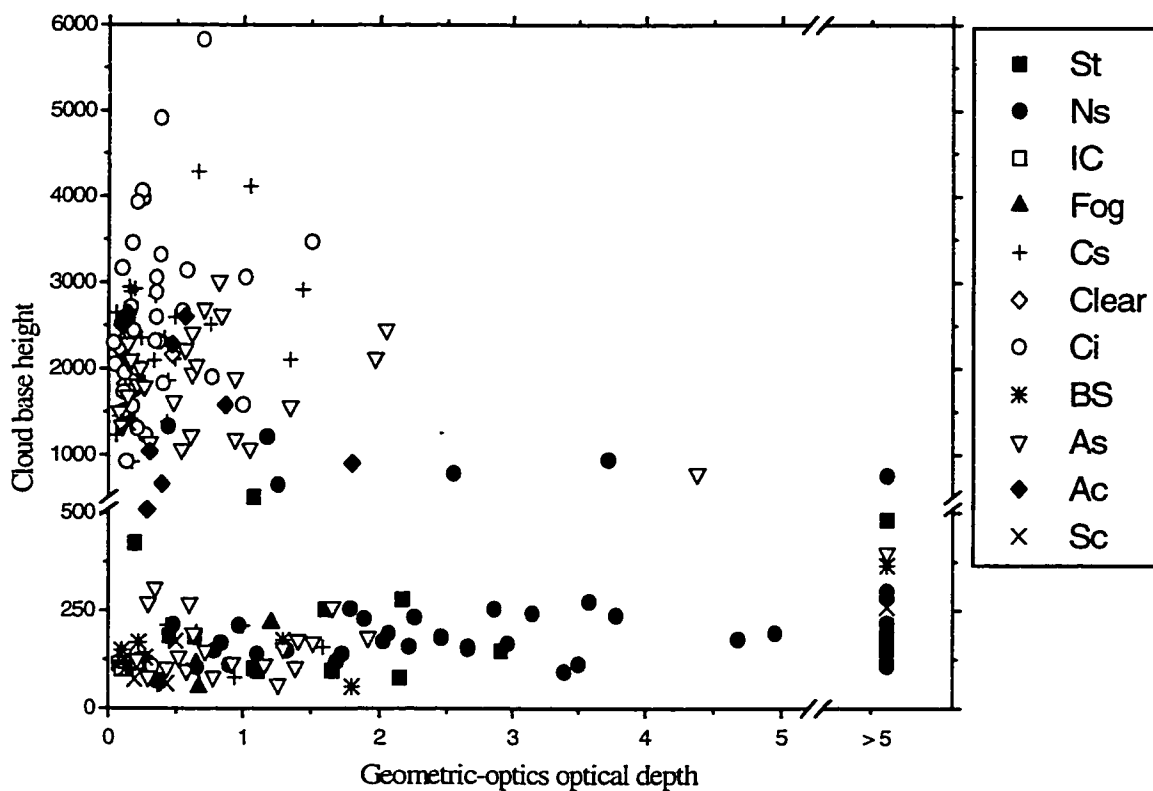


Figure 3.17: Cloud base heights and optical depths at South Pole, 1992 (note the break in the vertical axis to show the large number of clouds in the lowest 300 m). High clouds are typically thinner than low clouds, while low clouds have a larger range of optical depths. Almost all the thick clouds have base heights in the lowest 1000 m above the surface. The symbols indicate the cloud types reported by the South Pole Weather Office observers (St for stratus, Ns for nimbostratus, Cs for cirrostratus, Ci for cirrus, As for altostratus, Ac for altocumulus and Sc for Stratocumulus). In addition, a few cloudy spectra were also measured under other conditions, namely fog, blowing snow (BS) and falling ice crystals (IC), as well as one observation taken under reportedly clear skies (clear).

Chapter 4: Summary and Future Work

A year-long climatology of cloud properties over the interior of the Antarctic Plateau has not been previously compiled. This study has developed a climatology using ground based interferometer measurements of infrared spectra and coincident radiosonde and ozonesonde data. Cloud base heights were determined by radiance ratioing, a technique originally developed for the determination of cloud top heights from satellite data, applied to radiances in the 15- μm band of carbon dioxide. Computations using radiative transfer models usually compare temperature-dependent model calculations with actual measurements; this usually means that any atmospheric temperature inversions will result in multiple solutions. The radiance ratioing method has been further adapted to overcome this limitation, permitting clouds above the surface-based inversion to be distinguished from those below it. A bimodal distribution of cloud base heights is observed; several clouds with base heights below the surface-based inversion are seen, and a second mode with base heights between 2 and 3 km above the surface is also observed.

Future research into the causes of cloud formation over the plateau is necessary to determine why a bimodal distribution of cloud base heights is observed. Continuous measurements of vertical wind shear in the lower atmosphere, wind direction and speed over the plateau, and observations of large weather systems off the coast of the continent may suggest that the two modes represent different processes by which clouds are formed on the plateau.

These data are also obtained from a single year; more measurements from addi-

tional years are needed to augment the findings reported here. Tethered sondes will be useful in understanding the near-surface atmospheric conditions over the plateau. Lidar measurements of cloud base heights also need to be made continuously. Reliable lidar measurements were not available during the time of the spectral measurements, the spectral method had to be developed to overcome this difficulty. The successful development of the algorithm used here, however, suggests that interferometric data can be used to obtain several cloud properties, including their base heights, and a second instrument to obtain cloud base heights is not needed.

Clouds over the Antarctic plateau are seen to be much less optically thick than those on the coast of Antarctica. This is expected, since weather systems near the coast are significantly weakened during ascent over the plateau. Cloud optical depths in excess of 20 are observed on the coast regularly, whereas nearly 95% of the clouds have optical depths less than 5 over the interior. The low optical depths are readily inferred from the spectral measurements in the 9.6- μm band of ozone emission, where the signal of stratospheric ozone is almost always seen through a cloud by the instrument at the surface. The optical depths of very thick clouds cannot be determined from the spectra, since radiance from clouds of optical depths larger than 5 is fairly independent of the optical depth itself.

Cloud particle effective radii were also obtained from the spectra by model comparisons to clouds with varying cloud particle sizes. Particle radii smaller than about 25 microns can be deduced from the spectral observations, but only a lower limit to larger particles is known. The particle radii obtained from the spectra were compared to values obtained from photographs of ice crystals collected at the surface. Three different ways of

obtained the particle radius were applied to the digitized photographs, and an appropriate procedure to represent ice crystals is chosen from among the three. The procedure represents crystals as spheres of equivalent surface area and volume without conserving the number of particles; this allows both absorption and scattering to be represented well in radiative transfer calculations.

The climatologies presented in this thesis are a significant step toward better characterization of Antarctic clouds in global climate models, which indicate that climate as far north as the lower northern latitudes may be sensitive to changes in the properties of clouds on the Antarctic continent. Standard atmospheres need to be defined to characterize the Antarctic plateau, similar to the standard atmospheres previously defined by the Air Force Geophysical Laboratory (McClatchey et al., 1972) for the tropics, midlatitude summer, midlatitude winter, subarctic summer and subarctic winter. Radiosonde data and ozonesonde data from several years are available for this purpose, and these can be used to construct average profiles for the Antarctic summer, winter, and spring. Such average profiles can be used to represent the seasons over the continent. Temperature measurements will have to be corrected for the thermal lag of thermistors on the radiosondes as has been done for data taken from 1992 (see Appendix B, reprint of previous publication in the *Journal of Atmospheric and Oceanic Technology*).

The radiative effect of diamond dust in the near-surface atmosphere should also be investigated. The South Pole dataset includes a few observations made under clear skies when weather office observers reported diamond dust to be present. Model calculations using particle sizes typical of diamond dust and several assumed densities can be per-

formed to infer the distribution of ice crystals in the near-surface atmosphere which can explain the observed spectra.

Findings from this study, as well as the above-mentioned further work, will permit the incorporation of cloud properties into global climate models more accurately. Sensitivity studies using such climate models may then facilitate a better understanding of the changes in climate we can expect will take place due to changes on the Antarctic continent. At a time when there is significant concern around the world regarding the potential consequences of global climate change, it is important to understand how this endpoint in terrestrial climate plays a role in those changes.

References

- Berk, A., L. S. Bernstein, and D. C. Robertson, 1989. MODTRAN: A moderate resolution model for LOWTRAN7. AFGL-TR-89-0122. Air Force Geophysics Laboratory, Hanscom AFB, Mass. 01731, 38pp.
- Bromwich, D. H., 1979. *Precipitation and Accumulation Estimates for East Antarctica Derived from Rawinsonde Information*. Ph.D. Thesis, University of Wisconsin, 142 pp.
- Budd, W. F., 1991. Antarctica and global change. *Clim. Change*, **18**, 271-299.
- Budd, W. F., and I. Simmonds, 1991: Impact of global warming on the Antarctic mass balance and global sea level. *Proceedings of the International Conference on the Role of the Polar Regions in Global Change*, Fairbanks, Alaska, June 11-15, 1990, edited by G. Weller, C. L. Wilson, and B. A. B. Severin, pp. 489-494.
- Cess, R. D., 1989: Interpretation of cloud-climate feedback as produced by 14 atmospheric general circulation models. *Science*, **245**, 513-516.
- Cess, R. D., M. H. Zhang, W. J. Ingram, G. L. Potter, V. Alekseev, H. W. Barker, E. Cohen-Solal, R. A. Colman, D. A. Dazlich, A. D. Del Genio, M. R. Dix, V. Dymnikov, M. Esch, L. D. Fowler, J. R. Fraser, V. Galin, W. L. Gates, J. J. Hack, J. T. Kiehl, H. Le Treut, K. K.-W. Lo, B. J. McAvaney, V. P. Meleshko, J. J. Morcrette, D. A. Randall, E. Roeckner, J. -F. Royer, M. E. Schlesinger, P. V.

- Sporyshev, B. Timbal, E. M. Volodin, K. E. Taylor, W. Wang, and R. T. Wetherald, 1995: Cloud feedback in atmospheric general circulation models: an update. *J. Geophys. Res.*, **101**, 12791-12794.
- Chahine, M.T., 1974: Remote sounding of cloudy atmospheres. I. The single cloud layer. *J. Atmos. Sci.*, **31**, 233-243.
- Chen, B., D. H. Bromwich, K. M. Hines, and X. Pan, 1995: Simulations of the 1979-88 polar climates by global climate models. *Annals of Glaciology*, **21**, 83-90.
- Clapp, P. F., 1964: Global cloud cover for seasons using TIROS nephanalyses. *Mon. Wea. Rev.*, **92**, 495-507.
- Clough, S.A., M. J. Iacono, and J. L. Moncet, 1992: Line-by-line calculations of atmospheric fluxes and cooling rates: Application to water vapor, *J. Geophys. Res.*, **97**, 15761-15785.
- Collard, A. D., S. A. Ackerman, W. L. Smith, X. Ma, H. E. Revercomb, R. O. Knuteson, and S. -C. Lee, 1995: Cirrus cloud properties derived from high spectral resolution infrared spectrometry during FIRE II. Part III: Ground-based HIS results. *J. Atmos. Sci.*, **52**, 4264-4275.
- Crane, R. G., and R. G. Barry, 1984: Influence of clouds on climate with a focus on high-latitude interactions. *J. Climatology*, **4**, 71-93
- Dalrymple, P.C., 1966. A physical climatology of the Antarctic Plateau. In *Studies in Antarctic Meteorology*, M.J. Rubin (editor), *A.G.U. Antarctic Research Series*, **9**,

195-231.

Del Guasta, M., M. Morandi, L. Stefanutti, J. Brechet, and J. Piquad, 1993: One year of cloud lidar data from Dumont d'Urville (Antarctica). 1: General overview of geometrical and optical properties. *J. Geophys. Res.*, **98**, 18575-18587.

Dozier, J., and S.G. Warren, 1982. Effect of viewing angle on the infrared brightness temperature of snow. *Water Res. Res.*, **18**, 1424-1434.

Dutton, E. G., R. S. Stone, D. W. Nelson, and B. G. Mendonca, 1991: Recent interannual variations in solar radiation, cloudiness, and surface temperature at the South Pole. *J. Climate*, **4** 848-858.

Ebert, E. E., 1987: A pattern recognition technique for distinguishing surface and cloud types in the polar regions. *J. Climate and Appl. Meteor.*, **26**, 1412-1427.

Ebert, E. E., 1989: Analysis of polar clouds from satellite imagery using pattern recognition and a statistical cloud analysis scheme *J. Appl. Meteor.*, **28**, 382-399.

Ebert, E. E., 1992: Pattern recognition analysis of polar clouds during summer and winter. *Intl. J. Remote Sens.*, **13**, 97-109.

Ebert, E. E., and J. A. Curry, 1992: A parameterization of ice cloud optical properties for climate models. *J. Geophys. Res.*, **97**, 3831-3836.

Frey, R., 1988: *On the Determination of Cloud Altitude using Infrared Spectral Radiances.*

M.S. Thesis, University of Wisconsin-Madison, 52 pp.

Grenfell, T.C., 1998: Evolution of electromagnetic signatures of sea ice from initial formation to establishment of thick first-year ice. *IEEE TGARS*, **36**, 5, 1642-1654.

Grenfell, T. C., and S. G. Warren, 1999: Representation of a nonspherical ice particle by a collection of independent spheres for scattering and absorption of radiation. Submitted to *J. Geophys. Res. (Atmospheres)*.

Grund, C.J., S.A. Ackerman, E.W. Eloranta, R.O. Knuteson, H.E. Revercomb, W.L. Smith, and D.P. Wylie, 1990. Cirrus cloud characteristics derived from volume imaging lidar, high spectral resolution lidar, HIS radiometer, and satellite. In *Proceedings of the Seventh Conference on Atmospheric Radiation*, American Meteorological Society, 357-362.

Hahn, C. J., S. G. Warren, and J. London, 1995: The effect of moonlight on observation of cloud cover at night, and application to cloud climatology. *J. Climate*, **8**, 1429-1446.

Houghton, J. T., 1991: *The Physics of Atmospheres*. Appendix 10., Cambridge University Press. pp 251-252.

Hughes, N. A., 1984. Global cloud climatologies: a historical review. *J. Clim. Appl. Meteor.*, **23**, 724-51.

Kikuchi, K., and A. W. Hogan, 1979: Properties of diamond dust type ice crystals observed in summer season at Amundsen-Scott South Pole Station, Antarctica. *J.*

Meteor. Soc. Japan, **57**, 180-190.

King, J.C., and J. Turner, 1997. *Antarctic Meteorology and Climatology*, Cambridge University Press, 409 pp.

King, M. D., Y. J. Kaufmann, W. P. Menzel, and D. Tanre, 1992: Remote sensing of cloud, aerosol, and water vapor properties from the Moderate Resolution Imaging Spectrometer (MODIS). *IEEE Transactions on Geoscience and Remote Sensing*, **30**, 2-27.

Kuhn, M., 1972: Die spektrale Transparenz der antarktischen Atmosphaere, Teil II: Messergebnisse und Analyse. *Arch. Met. Geoph. Biokl.*, Ser. B, **20**, 299-344.

Lacis, A., J. Hansen, and M. Sato, 1992: Climate forcing by stratospheric aerosols. *Geophys. Res. Lett.*, **19**, 1607-1612.

Lubin, D., 1994. Infrared properties of the maritime Antarctic atmosphere. *J. Climate*, **7**, 121-140.

Lubin, D., B. Chen, D. H. Bromwich, R. C. J. Somerville, W. Lee, and K. M. Hines, 1998: The impact of Antarctic cloud radiative properties on a GCM climate simulation. *J. Climate*, **11**, 447-462.

Lubin, D., and D. A. Harper, 1996: Cloud radiative properties over the South Pole from AVHRR Infrared Data. *J. Climate*, **9**, 3405-3418.

Mahesh, A., V.P. Walden and S.G. Warren, 1997: Radiosonde temperature measurements

in strong inversions: Correction for thermal lag based on an experiment at South Pole. *J. Atmos. Ocean. Tech.*, **14**, 45-53.

Mahesh, A., V. P. Walden, and S. G. Warren, 1999: Ground-based infrared remote sensing of cloud properties over the Antarctic Plateau, Part I: Cloud base heights.

Submitted to *J. Appl. Meteor.*

Manabe, S., and R.J. Stouffer, 1979. A CO₂-climate sensitivity study with a mathematical model of the global climate. *Nature*, **282**, 491-493.

McClatchey, R. A., R.W. Fenn, J.E.A. Selby, F.E. Volz, and J.S. Garing, 1972: Optical properties of the atmosphere. Rep. AFCRL-72-0497, 108 pp. [Available from Geophysics Laboratory, Hanscom AFB, Bedford MA 01731].

McCleese, D. J., and L.S. Wilson, 1976: Cloud top heights from temperature sounding instruments. *Q. J. R. Met. Soc.*, **102**, 781-790.

Menzel, W. P., W.L. Smith, and T.R. Stewart, 1983: Improved cloud motion wind vector and altitude assignment using VAS. *J. Appl. Meteor.*, **22**, 377-384.

Morley, B. M., E. E. Uthe, and W. Viezee, 1989: Airborne lidar observations of clouds in the Antarctic troposphere. *Geophys. Res. Lett.*, **16**, 491-494.

Nemesure, S., R. D. Cess, E. G. Dutton, J. J. DeLuisi, Z. Li, and H. G. Leighton, 1994: Impact of clouds of the shortwave radiation budget of the surface-atmosphere system for snow-covered surfaces. *J. Climate*, **7**, 579-585.

Parish, T.R., 1992. On the role of Antarctic katabatic winds in forcing large-scale

tropospheric motions. *J. Atmos. Sci.*, **49**, 1374-1385.

Platt, C. M. R., 1989: The role of cloud microphysics in high-cloud feedback effects on climate change. *Nature*, **341**, 428-429.

Ricchiazzi, P., C. Gautier, and D. Lubin, 1995: Cloud scattering optical depth and local surface albedo in the Antarctic: Simultaneous retrieval using ground-based radiometry. *J. Geophys. Res.*, **100**, 21,091-21,104.

Rossow, W. B., A. W. Walker, and L. C. Garder, 1993: Comparison of ISCCP and other cloud amounts. *J. Climate*, **6**, 2394-2417.

Sakellariou, N. K., H. G. Leighton, and Z. Li, 1993: Identification of clear and cloudy pixels at high latitudes from AVHRR radiances. *Intl. J. Remote Sens.*, **14**, 2005-2024.

Saxena, V. K., and F. H. Ruggiero, 1990: Antarctic coastal stratus clouds: Microstructure and acidity. *Contributions to Antarctic Research I*, *Antarc. Res. Series*, **50**, 5-18.

Schneider, G., P. Paluzzi, and J. P. Oliver, 1989: Systematic error in the synoptic sky cover record of the South Pole. *J. Climate*, **2**, 295-302.

Schwerdtfeger, W., 1970. The Climate of the Antarctic. In *World Survey of Climatology*, vol. 14, 253-355.

Schwerdtfeger, W., 1984. *Weather and Climate of the Antarctic*. Developments in

Atmospheric Science, 15, Elsevier Science Publishers, New York, New York, 261 pp.

Simmonds, I., 1990. Improvements in general circulation model performance in simulating Antarctic climate. *Ant. Sci.*, **2**, 287-300.

Smith, W.L. and R. Frey, 1990. On cloud altitude determinations from High Resolution Interferometer Sounder (HIS) observations. *J. Appl. Met.*, **29**, 658-662.

Smith, W.L., X.L. Ma, S.A. Ackerman, H.E. Revercomb, and R.O. Knuteson, 1993. Remote sensing cloud properties from high spectral resolution infrared observations. *J. Atmos. Sci.*, **50**, 1708-1720.

Smith, W.L., and C.M.R. Platt, 1978: Comparison of satellite-deduced cloud heights with indications from radiosonde and ground-based laser measurements. *J. Appl. Meteor.*, **17**, 1796-1802.

Smith, W.L., H.M. Woolf, P.G. Abel, C.M. Hayden, M. Chalfant, and N. Grody, 1974: *Nimbus-5 Sounder Data Processing System. Part I: Measurement Characteristics and Data Reduction Processes*. NOAA Tech. Memo. NESS 57, 99 pp.

Stamnes, K., S.-C. Tsay, W. Wiscombe and K. Jayaweera, 1988: A numerically stable algorithm for discrete-ordinate-method radiative transfer in multiple scattering and emitting layered media, *Appl. Opt.* **27**, 2502-2509.

Stephens, G. L., 1980: Radiative properties of cirrus clouds in the infrared region. *J. Atmos. Sci.*, **37**, 435-446.

- Stephens, G. L., S. C. Tsay, P. W. Stackhouse Jr., and P. J. Flatau, 1990: The relevance of the microphysical and radiative properties of cirrus clouds to climate and climatic feedback. *J. Atmos. Sci.*, **47**, 1742-1753.
- Stone, R. S., 1993: Properties of austral winter clouds derived from radiometric profiles at the South Pole. *J. Geophys. Res.*, **98**, 12961-12971
- Stone, R.S., E.G. Dutton, and J.J. DeLuisi, 1989. Surface radiation and temperature variations associated with cloudiness at the South Pole. *Antarctic J. U.S.*, **24**, 230-232.
- Stone, R.S., and J.D. Kahl, 1991. Variations in boundary layer properties associated with clouds and transient weather disturbances at the South Pole during winter. *J. Geophys. Res.*, **96**, 5137-5144.
- Stone, R. S., G. L. Stephens, C. M. R. Platt, and S. Banks, 1990: The remote sensing of thin cirrus cloud using satellites, lidar and radiative transfer theory. *J. Appl. Meteor.*, **29**, 353-366.
- Strabala, K.I., S.A. Ackerman, and P. Menzel, 1994. Cloud properties inferred from 8-12- μm data. *J. Appl. Met.*, **33**, 212-229.
- Tzeng, R-Y., D.H. Bromwich, and T.R. Parish, 1993. Present-day Antarctic climatology of the NCAR Community Climate Model version 1. *J. Climate*, **6**, 205-226.
- Tzeng, R-Y., D.H. Bromwich, T.R. Parish, and B. Chen, 1994. NCAR CCM2 simulation

of the modern Antarctic climate. *J. Geophys. Res.*, **99**, 23131-23148.

Vaughan, D. G., and C. S. M. Doake, 1996: Recent atmospheric warming and retreat of ice shelves on the Antarctic Peninsula. *Nature*, **379**, 328-331.

Venter, R.J., 1957. Sources of meteorological data for the Antarctic. In *Meteorology of the Antarctic*, M.P. van Rooy (editor), Weather Bureau of South Africa, Department of Transport, Pretoria, 17-38.

Wada, M., and T. Takeda, 1983: Characteristic features of clouds in Antarctica as observed at Showa Station. in *Japan. Natl. Instt. of Polar Res., Memoirs, Special Issue*, **29**, 94-102.

Walden, V. P., 1995. *The downward longwave radiation spectrum over the Antarctic plateau*. Ph.D. Thesis, University of Washington, Seattle, 267 pp.

Walden, V. P., S. G. Warren, and F. J. Murcray, 1998: Measurements of the downward longwave radiation spectrum over the Antarctic Plateau and comparisons with a line-by-line radiative transfer model for clear skies. *J. Geophys. Res.*, **103**, 3825-3846.

Warren, S.G., 1984: Optical constants of ice from the ultraviolet to the microwave. *Applied Optics*, **23**, 1206-1225.

Warren, S. G., 1996: *Antarctica*. In *Encyclopedia of Climate and Weather*, Oxford University Press, New York, 32-39.

- Wielicki, B. A., and J.A. Coakley Jr., 1981: Cloud retrieval using infrared sounder data: Error analysis. *J. Appl. Meteor.*, **20**, 157-169.
- Wiscombe, W. J., 1979: Mie scattering calculations: Advances in technique and fast, vector-speed computer codes. NCAR Tech. Note TN-140+STR [NTIS PB 30i388].
- Wiscombe, W. J., 1980: Improved Mie scattering algorithms. *Applied Optics*, **19**, 1505-1509.
- World Meteorological Organization, 1974: Manual on Codes, Vol. 1, WMO Publ. No. 306, WMO, Geneva.
- Wu, Man-Li C., 1987: A method for remote sensing the emissivity, fractional cloud cover and cloud top temperature of high-level, thin clouds. *J. Clim. Appl. Meteor.*, **26**, 225-233.
- Yamanouchi, T., and T. P. Charlock, 1995: Comparison of radiation budget at the TOA and surface in the Antarctic from ERBE and ground surface measurements. *J. Climate*, **8**, 3109-3120.
- Yamanouchi, T., K. Suzuki, and S. Kawaguchi, 1987. Detection of clouds in Antarctica from infrared multispectral data of AVHRR. *J. Met. Soc. Japan*, **65**, 949-962.

Appendix A. Comment on "Recent changes in the North American Arctic boundary layer in winter" by R.S. Bradley et al.

JOURNAL OF GEOPHYSICAL RESEARCH, VOL. 101, NO. D3, PAGES 7127-7134, MARCH 20, 1996

Comment on "Recent changes in the North American Arctic boundary layer in winter" by R. S. Bradley et al.

Von P. Walden, Ashwin Mahesh, and Stephen G. Warren

Geophysics Program and Department of Atmospheric Sciences, University of Washington, Seattle

Introduction

Near-surface temperature inversions are common in the Arctic and Antarctic, especially in winter. An early, comprehensive study of Arctic inversions was done by Belmont [1957]. More recently, Kahl et al. [Kahl, 1990; Kahl et al., 1992a, 1993a b; Serreze et al., 1992; Skony et al., 1994] have investigated the characteristics of Arctic inversions and have also constructed a database of Arctic radiosonde data [Kahl et al., 1992b]. Antarctic inversions have been examined by Stone and Kahl [1991]. Inversions on the Arctic coast of North America have been characterized by Bradley et al. [1992], who restricted their study to surface-based inversions. In their subsequent work, Bradley et al. [1993] (hereinafter referred to as BKD) showed that the average height of wintertime surface-based inversions (average of the 4 months December to March) had decreased by about one third from 1967 to 1990 at all the stations they analyzed (three in Alaska and six in Canada). This was true regardless of whether the average surface air temperature, for days with surface-based inversions, increased (e.g., Inuvik, Canada and Barrow, Alaska) or decreased (Eureka, Canada) as shown in Figures 2 and 3 of BKD. They were unable to find a physical explanation for this dramatic trend in inversion height.

We find that BKD's conclusion is sensitive to their particular definition of average inversion height, in which the lowest inversion height is first found in each individual profile, and those heights are then averaged for a season. As shown below, when we instead first average all the temperature profiles for a season and then find the inversion height in the seasonal average profile, we find no significant climatological trend over the past few decades. Our conclusion is to recommend the use of monthly or seasonal average profiles in climatological studies of inversions for the following reasons:

1. The various definitions of "inversion height" often lead to different diagnostic heights when applied to a single profile, but they usually all agree when applied to the much smoother monthly or seasonal average profile.
2. Nonclimatic causes, such as improvement in thermometer response time, reduction of balloon ascent rate, and

increase in the sampling rate of radio transmission, can cause an apparent decreasing trend in the height of the lowest inversion in individual soundings by adding detail and therefore reducing the smoothness of the profile. Such changes in operational procedures have much less effect on the seasonal average profile.

Average Temperature Profiles at Barrow and Eureka

We have analyzed radiosonde data from Barrow and Eureka, the stations with the lowest and highest frequencies of wintertime surface-based inversions (61% and 84%, respectively, on average, according to Table 1 of BKD). The period of record analyzed by BKD was 38 years at Barrow and 24 years at Eureka. Soundings were made at 0000 and 1200 UT; we have analyzed all of the 1200 UT soundings for the four winter months December to March, as did BKD. (At Barrow, the soundings prior to 1958 were made at other times, usually 0300 and 1500 UT. We use the sounding closest to 1200 UT for those years, as did BKD; it was usually at 1500 UT.)

Although the radio transmissions from each radiosonde to its ground station are sampled at intervals of a few seconds, only a small subset of the data is sent out to the Global Telecommunications System (GTS) to be archived: the "mandatory" levels (surface, 1000, 850, 700, 500, 400, 300, 250, 200, 150, 100, 70, 50, 30, 20, 10, 7, 5, 3, 2, and 1 mbar) and "significant" levels, where the lapse rate or humidity changes significantly [National Weather Service, 1976].

Figure 1 shows the multiyear monthly average temperature profiles at Barrow and Eureka at 1200 UT, from the surface to 3000 m, for the four winter months. (The profiles for 0000 UT are nearly identical to those for 1200 UT except in March when surface warming is apparent in the afternoon.) There is an inversion in the monthly average profile in each of these months, and the average profiles are sufficiently smooth that all definitions of inversion height (such as the various definitions reviewed by Bradley et al. [1992]) are likely to agree; i.e., isothermal layers and multiple inversions are unlikely, so the height of maximum temperature is usually the same as the height at which the lapse rate ($-dT/dz$) first becomes positive.

Figure 1 shows that the inversion strength (difference between maximum temperature and surface air temperature) is greatest in December at Eureka (12 K) and in Janu-

Copyright 1996 by the American Geophysical Union.

Paper number 95JD03233.
0148-0227/96/95JD-03233\$05.00

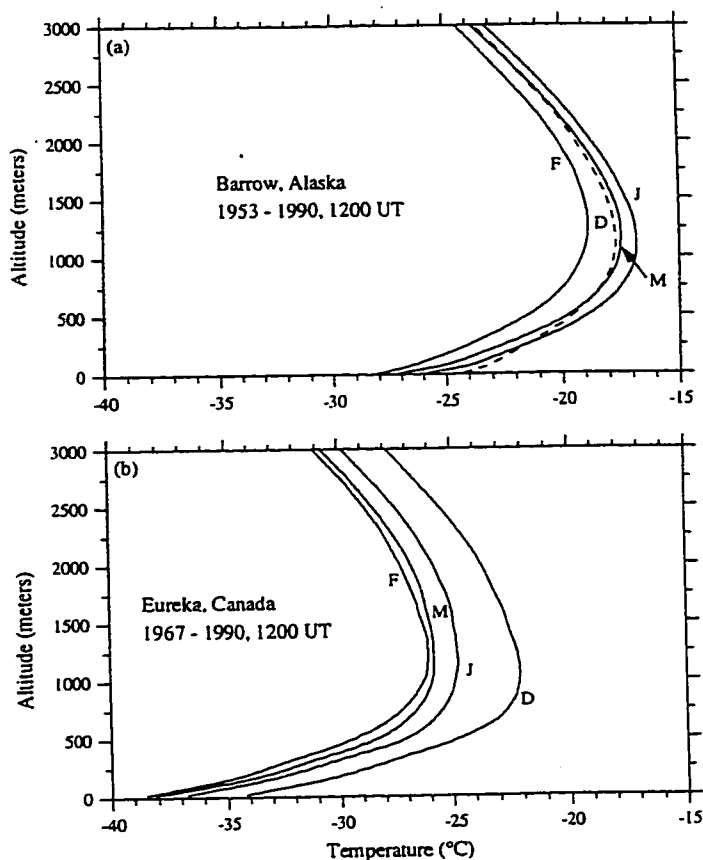


Figure 1. Multiyear monthly average temperature profiles (December, January, February, March) at 1200 UT for (a) Barrow (71°N, 157°W) and (b) Eureka (80°N, 86°W). Individual months are marked by their initials. The data at Barrow are for 1953-1990, and those for Eureka are for 1967-1990. (The Barrow soundings prior to 1958 were mostly at 1500 UT, not 1200.) Average temperature profiles are generated by linearly interpolating the individual daily soundings onto a 10-m grid and then averaging the gridded profiles.

ary at Barrow (9 K) and that the lowest 3 km of the troposphere is coldest in February at both locations. The average inversion height (height of maximum temperature) is about 1200 m at both Barrow and Eureka.

Recent Trends in Arctic Inversions

We now investigate multiyear trends in the wintertime inversion. BKD's method was to locate the top of the lowest inversion in individual soundings that exhibited surface-based inversions and then to average those heights. BKD rejected all soundings that did not contain inversions and also rejected soundings that did contain inversions unless there was a surface-based inversion (i.e., temperature increasing from the surface to the first above-surface reporting level). The fraction of soundings rejected varied by 20-50% from year to year.

The result of BKD's analysis is shown as the lower solid line in Figures 2a and 2b (copied from their Figures 2 and 3). Our analysis of the same radiosonde observations, using their procedure, gives similar results (dashed line). The small differences may mean that we have misinterpreted some subtleties of their criteria for rejecting erroneous soundings given in the appendix of *Bradley et al.* [1992].

However, when we instead first average all the temperature profiles for a season and then find the inversion height in the seasonal average profile, we find no significant trend at these two stations. These inversion heights are plotted as the upper lines in Figures 2a and 2b. Our average temperature profiles are found by linearly interpolating the individual daily soundings onto a 10-m grid and then averaging the gridded profiles. Most months have approximately 30 soundings, giving about 120 per season. The individual

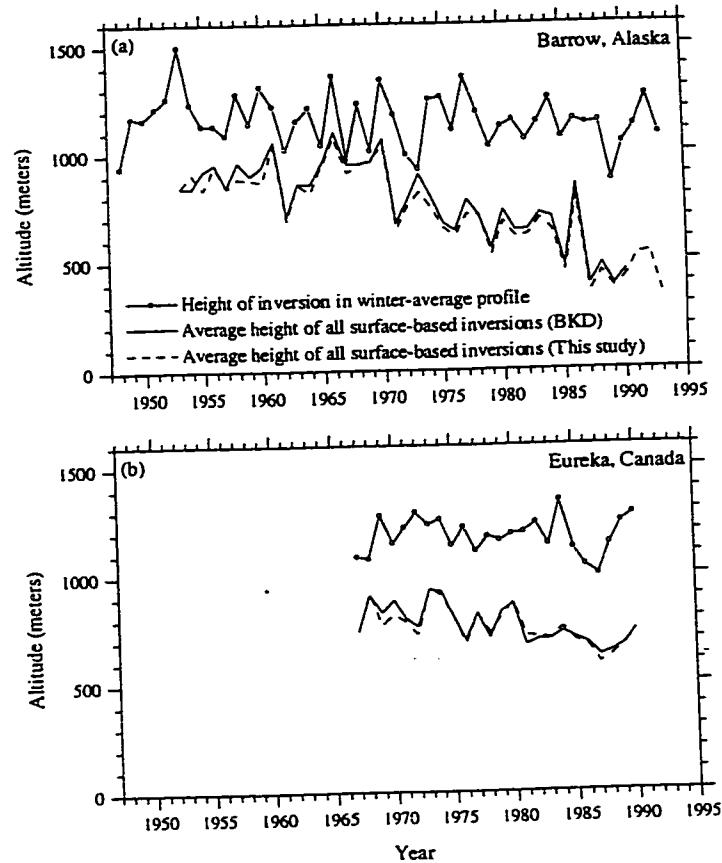


Figure 2. Winter-average inversion height at (a) Barrow and (b) Eureka, as determined by two different methods. Each point is the average for December-January-February-March, plotted in the year of January. The lower solid lines are copied from Figures 2 and 3 of *Bradley et al.* [1993]. The dashed lines are what we obtain when we apply their procedure to the soundings from these stations. The upper lines with open circles give the inversion height of the winter-average profiles. Least squares linear fits to the time series of winter-average profiles give slopes of -0.6 ± 2.5 m/yr (Eureka, 1967-1990); -2.0 ± 1.4 m/yr (Barrow, 1948-1993); and -3.8 ± 1.8 m/yr (Barrow, 1953-1990). The slope obtained is sensitive to the choice of starting and ending years [cf. *Karl*, 1994].

months are not weighted by the number of days per month; this lack of weighting introduces very little bias. An exception is 1973, which may be biased since it is missing data from January and most of February.

Figures 2a and 2b show that our diagnosed height for the top of the inversion is higher than those determined using BKD's method. At Barrow, where BKD reported the winter seasonal average of inversion height to drop from about 900 m to 400 m in 37 years, we find that the inversion height of the seasonal average profile fluctuated around 1200 m with no significant trend. There are slight negative trends at both Barrow and Eureka, but these trends do not differ significantly from zero at the 2σ level. The slope obtained is sensitive to the choice of starting and ending years [cf. *Karl*, 1994].

Another important measure is the inversion strength. The inversion strength of the winter average profiles (Figure 3) shows no trend at Barrow and a possible positive trend at Eureka. The results are insensitive to the temperature uncertainties in the average profiles.

BKD also reported trends in the seasonal average surface air temperature, which we are not discussing in this comment. However, those trends are for the same subset of data used for their inversion height analyses, i.e., only those soundings with surface-based inversions.

Explanations

To explain long-term trends in climatic variables, it is useful to classify the causes as "climatic" and "nonclimatic"

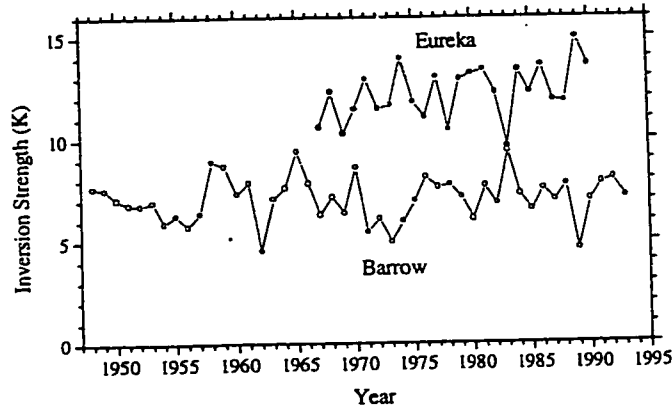


Figure 3. Inversion strengths at Barrow and Eureka determined from the winter-average temperature profiles. Least squares linear fits to these data give slopes of 0.00 ± 0.01 K/yr at Barrow and $+0.08 \pm 0.04$ K/yr at Eureka.

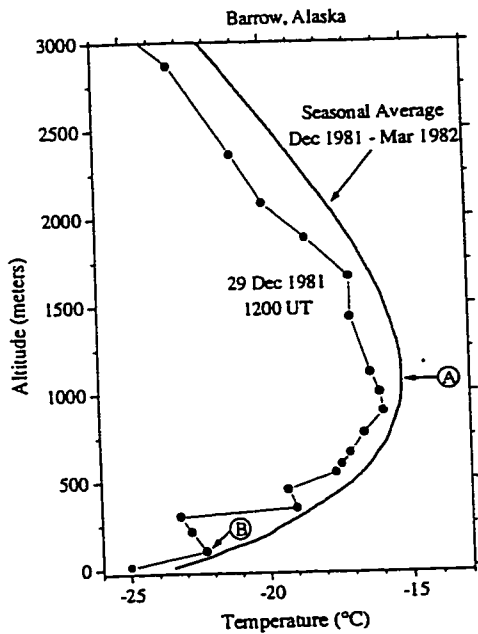


Figure 4. Illustration of the different results from two procedures used for assessing inversion height. The bold line is the average profile of the temperature in the lower troposphere at Barrow during December 1981 to March 1982. The thin line with reporting levels marked is one individual sounding taken during that winter. The method of Bradley *et al.* [1992] picks point B as the top of the surface-based inversion on that day. In the seasonal average profile, the top of the inversion is at point A.

[Jones *et al.*, 1986]. BKD suggest some possible climatic causes; here we investigate some possible nonclimatic causes, using the Barrow station as an example. Figure 4 shows the temperature profile at Barrow for a single sounding on December 29, 1981, together with the mean profile for that winter. The inversion height for the average profile is marked A; the height of the surface-based inversion is marked B, according to the criterion of BKD as the first point at which the lapse rate ($-dT/dZ$) becomes positive. BKD's reported average inversion height is the average of all points B on individual profiles that contained a surface-based inversion.

Thermistor Response Time

Our first thought was that improvements in radiosonde technology had allowed a more rapid response of the thermistor in more recent years, thus increasing the resolution of small-scale temperature fluctuations in the profile. This would result in the identification of a greater number of "significant" levels, and BKD did indeed find an increase over the years in the number of significant levels at all nine stations they studied. Soundings from earlier years, assuming a slower thermistor response, would be relatively smoother and also lagged relative to the true temperature profile, both factors causing the apparent height of the inversion to decrease with time. This is indeed what happened with Vaisala radiosondes. Huovila and Tuominen [1989] (quoted also in Table 2 of Parker and Cox [1995]) showed that the thermistor's e -folding response time τ at 1000 mbar pressure decreased from 10.5 s (1938-1959), to 5.1 s (1960-1975), 3.5 s (1976-1980), and 2.3 s (1981-1989), causing an apparent downward trend to the height of wintertime inversions in Finland. (Thermal lag was also shown by Skony *et al.* [1994] to cause the temperature profiles measured by radiosondes to differ from those measured by dropsondes.)

However, this effect turned out not to be relevant for the Barrow record. The response time of the temperature element in U.S. radiosondes was reduced in 1949 [Elliott and Gaffen, 1991, Table 1; Jenne and McKee, 1985, p. 1198] but was not changed subsequently. The radiosondes used at Barrow were made by Bendix-Friez prior to 1958 and by VIZ Corporation since 1958 (A. Brewington, personal communication, 1994). Both sondes have the same 5 to 6 s response time (M. Friedman, VIZ Corporation, personal communication, 1994). This is the radiosonde type used at most U.S. Weather Service stations. The Army radiosondes have a shorter response time of 3 to 4 s because they are thinner; the response time is proportional to the square of the radius of the thermistor rod [Ney *et al.*, 1961]. In conclusion, although thermistor response time did shorten over the past few decades in Europe and may have shortened in the Soviet Union [Zaitseva [1993] gives the response time as 5-6 s only for the new thermistor introduced in 1984], it did not change at Barrow.

Ascent Rate of Balloon

In interviews with past and present weather observers at Barrow, we learned that the balloons had been inflated with hydrogen or helium in the 1940s and 1950s but have been inflated with natural gas since March 1967. The balloon ascent rate with helium was 6 m s^{-1} ; with natural gas, it is only 3 m s^{-1} . This change would have the same effect on the temperature profile as reducing the thermistor response time by half.

Radio Transmission Rate

Over the years, the data transmission rate of radiosondes has increased and reporting policies have changed. Together, these modifications would be expected to change the number of levels reported in individual soundings. The increase in the number of levels over time seen at Barrow, excluding data from 1965-1970 (Figure 5), indicates that the soundings contain more detailed structure, increasing the likelihood of detecting the first inversion top (point B in Figure 4) lower in the atmosphere. This, in turn, may contribute to the decreasing trend in the average height of surface-based inversion reported by BKD. An increase in the frequency of heights of surface-based inversions below 100 m is indeed seen in the Barrow record (Figure 6).

For VIZ radiosondes, the radio transmission rate for 1950-1986 was controlled by a "baroswitch" which transmitted approximately every 12 mbar in the lower atmosphere; i.e., about 100 m or 20 s (M. Friedman, personal communication, 1994). During this period, the radiosonde data were recorded onto a strip chart recorder. A major instrumentation revision occurred with the introduction of the Automatic Radio Theodolite (ART) systems around 1986, when the use of the strip chart was eliminated and the transmission rate was no longer controlled by the baroswitch. The ART system radiosondes report data at high frequency, which are then averaged by a ground station computer to produce a raw sounding with points every 6 s during the radiosonde flight.

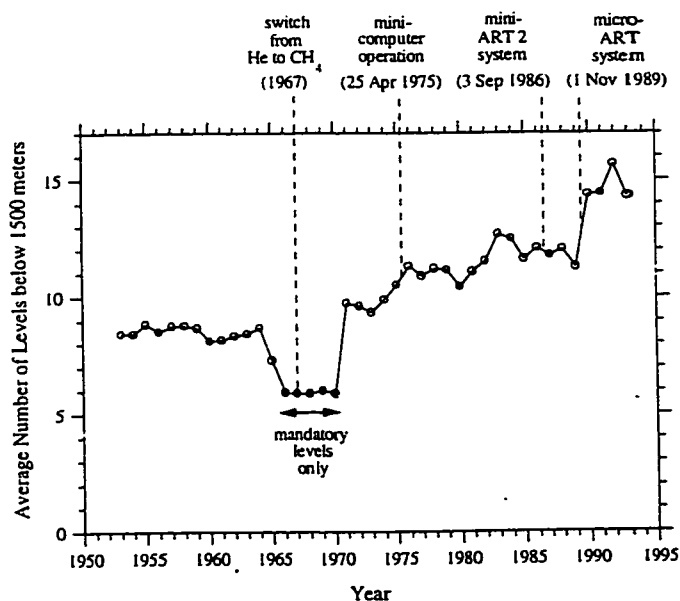


Figure 5. Average number of levels (mandatory plus significant) below 1500 m in winter season radiosonde reports at Barrow. Dates are marked at which changes were made in balloon ascent rate, radiosonde data transmission rate, and computer processing procedures. Some of these dates were given by Schwartz and Wade [1993] and Schwartz and Govett [1992].

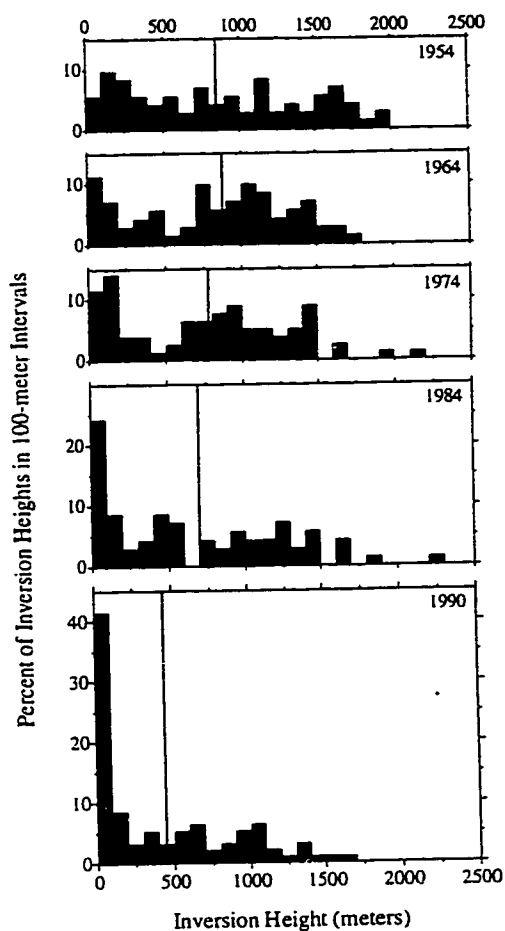


Figure 6. Frequency distribution of heights of surface-based inversions, found using BKD's method for a sample winter season in each of five decades. The vertical solid lines indicate the winter average inversion heights as determined by BKD. The distribution changes over time, showing an increasing number of inversion heights below 100 m.

Reporting Policy

The method for processing the raw sounding data has changed due to modifications in reporting policy. An example was noted by BKD in the Barrow record for the years 1965-1970, when only data from mandatory levels were available (Figure 5). The absence of significant levels caused the temperature profile to contain less structure and therefore the height of the first detected inversion to be higher on average (Figure 2a). The designation of mandatory levels has also changed in time; recently, another level was added at 925 mbar.

Other policy changes were instituted at the time of instrumentation upgrades. The introduction of the mini-computer system around 1975 eliminated the need to manu-

ally convert values from the strip chart to atmospheric temperatures and significantly reduced the amount of manual calculation performed by human observers. The switch to the mini-ART 2 system (in 1986 at Barrow) was the first fully automated system to determine significant levels without the strip chart recorder.

The criterion for defining significant levels has also changed in time. Prior to 1989 and the introduction of the micro-ART system, significant levels below 100 mbar were determined based on a departure of the temperature from linearity of greater than 1°C; the actual significant level is the point of maximum departure. The micro-ART system lowered the temperature criterion to 0.5°C; its introduction thus resulted in a greater number of significant levels (Figure 5).

Other Nonclimatic Factors

The last three nonclimatic factors discussed above are probably the ones most likely to have affected the radiosonde record at Barrow. Other factors that may affect the record at Arctic stations of other countries are all four of those discussed above, as well as the following factors.

Correcting for thermal lag. A simple correction procedure, recommended by *Jensen* [1958], is to take the temperature measured at time t but assign it to the pressure measured at time $(t-\tau)$. This procedure, or something similar, has been used at many stations, as reviewed by *Gaffen* [1994] and *Parker and Cox* [1995]. Implementation of this correction would cause a decrease in the derived inversion heights.

Pressure sensor. The response time τ to be applied in the correction for thermal lag is actually the difference between response times of the thermistor and the pressure sensor. Changes in the response time of the pressure sensor could therefore affect the reported profiles. We have been unable to obtain information about the response time of the pressure sensor.

Insertion of surface air temperature. The radiosonde report is augmented before it is sent to the GTS, by insertion of the surface air temperature as the first temperature in the profile. Details of how this is done can affect the diagnosis of a surface-based inversion. At Barrow, it was done in three ways: (1) by measuring the temperature at the balloon launch site, (2) by measuring the temperature at a fixed "screen" location, or (3) by extrapolation of the radiosonde transmissions down to ground level (C. Doran, personal communication, 1994). Depending on which procedure is used at a particular station, spurious surface-based inversions would appear if the balloon inflation tower (BIT) is significantly warmer or colder than the surface air, because the balloon is normally released immediately after opening the tower doors. We observed this effect in our experiments at South Pole Station, where the BIT is heated. The first temperature in the report is the surface air temperature; the second temperature is the first radiosonde transmission, which can be artificially high because of its memory of the warm room. The third temperature is colder again, so there

is an apparent but spurious surface-based inversion whose top is at the second level of the report [Walden and Warren, 1993, Figure 2]. At Barrow, the BIT is not heated, but it is sometimes warmer (colder) than the surrounding air because of recent cold (warm) synoptic-scale air advection.

Recommended Procedure for Analysis of Inversions

In an individual profile such as in Figure 4, the diagnosed height of the top of the inversion differs depending on which definition is used. BKD reviewed several definitions and chose one, which diagnoses point B as the inversion height in this particular profile. This choice is sensitive to the vertical resolution of the radiosonde data, which is affected by the factors listed above. However, even if the plotted profile is taken to be a true representation of the atmosphere, we think that point B may not be a particularly significant feature of the atmosphere. The small-scale structure in the temperature profile is due to interleaving (incomplete mixing) of adjacent air parcels and could be quite different in detail if measured by a second radiosonde launched just a few hours later.

We think it is probably more useful to study the monthly or seasonal average profile, in which the erratic fluctuations of individual profiles are averaged out, and all definitions of inversion height then agree. Furthermore, the inversion strength of the average profile is less ambiguous, and thus may be a more useful indicator of climate change. A further advantage to studying average profiles is that they are less sensitive to the changes in radiosonde technology and changes in operational procedures described above. In regional and global climatic studies, it may not be practical to investigate the details of operational procedure at each station as we have done for Barrow, so it is therefore useful to choose an analysis method that is relatively insensitive to nonclimatic factors. Monthly average or seasonal average profiles may be more useful than individual profiles for other purposes as well, such as in comparison with climate-model simulations.

Acknowledgments. Will Spangler, Dennis Joseph, and Ernie Recker helped us access NCAR's radiosonde data set. Kitt Hughes and Bob Koney (National Weather Service (NWS), Kauai) assisted with our experiments on thermal lag of radiosondes at South Pole Station. We thank Richard Moritz, David Battisti, Tony Beesley, and Conway Leovy (University of Washington), Roy Jenne (NCAR), Carl Benson (University of Alaska), Phil Jones (University of East Anglia) and Jonathan Kahl (University of Wisconsin-Milwaukee) for helpful discussions. Helpful information about radiosonde operational procedures was provided by David Parker (U.K. Meteorol. Office), Dian Gaffen (NOAA Air Resources Lab.), Bary Schwartz (NOAA Environmental Research Lab.), Roger Tanner (National Climatic Data Center), Vin Lally (NCAR), Charles Wade (NCAR), Frank Schmidlin (NASA), Maurice Friedman (VIZ Corp.), Sue Ann Bowling (University of Alaska), Andrew Brewington (NWS, Anchorage), Chuck Evans (NWS, Barrow), and Curt Doran (NWS, Barrow, retired). We thank two anonymous reviewers for their valuable comments. This research was supported by NSF grants OPP-91-20380 and OPP-94-21096.

References

- Belmont, A.D., Lower tropospheric inversions at Ice Island T-3, *J. Atmos. Terr. Phys.*, special suppl., 215-284, 1957.
- Bradley, R.S., F.T. Keimig, and H.F. Diaz, Climatology of surface-based inversions in the North American Arctic, *J. Geophys. Res.*, **97**, 15,699-15,712, 1992.
- Bradley, R.S., F.T. Keimig, and H.F. Diaz, Recent changes in the North American Arctic boundary layer in winter, *J. Geophys. Res.*, **98**, 8851-8858, 1993.
- Elliott, W.P., and D.J. Gaffen, On the utility of radiosonde humidity archives for climate studies, *Bull. Am. Meteorol. Soc.*, **72**, 1507-1520, 1991.
- Gaffen, D.J., Temporal inhomogeneities in radiosonde temperature records, *J. Geophys. Res.*, **99**, 3667-3676, 1994.
- Huovila, S., and A. Tuominen, Effect of radiosonde lag errors on upper-air climatological data, in World Meteorological Organization Instruments and Observing Methods, Rep. 35, pp. 291-298, Washington, D.C., 1989.
- Jenne, R.L., and T.B. McKee, Data, in *Handbook of Applied Meteorology*, edited by D.D. Houghton, pp. 1175-1281, John Wiley, New York, 1985.
- Jensen, A., Correction of radiosonde measurements for lag error, *Geophysica*, **6**, 275-279, 1958.
- Jones, P.D., S.C.B. Raper, R.S. Bradley, H.F. Diaz, P.M. Kelly, and T.M.L. Wigley, Northern Hemisphere surface air temperature variations: 1851-1984, *J. Clim. Appl. Meteorol.*, **25**, 161-179, 1986.
- Kahl, J.D., Characteristics of the low-level temperature inversion along the Alaskan Arctic coast, *Int. J. Climatol.*, **10**, 537-548, 1990.
- Kahl, J.D., M.C. Serreze, and R.C. Schnell, Tropospheric low-level temperature inversions in the Canadian Arctic, *Atmos.-Ocean*, **30**, 511-529, 1992a.
- Kahl, J.D., M.C. Serreze, S. Shiotani, S.M. Skony, and R.C. Schnell, In situ meteorological sounding archives for Arctic studies, *Bull. Am. Meteorol. Soc.*, **73**, 1824-1830, 1992b.
- Kahl, J.D., D.J. Charlevoix, N.A. Zaitseva, R.C. Schnell, and M.C. Serreze, Absence of evidence for greenhouse warming over the Arctic Ocean in the past 40 years, *Nature*, **361**, 335-337, 1993a.
- Kahl, J.D.W., M.C. Serreze, R.S. Stone, S. Shiotani, M. Kiskey, and R.C. Schnell, Tropospheric temperature trends in the Arctic: 1958-1986, *J. Geophys. Res.*, **98**, 12,825-12,838, 1993b.
- Karl, T.R., Smudging the fingerprints, *Nature*, **371**, 380-381, 1994.
- National Weather Service, *Radiosonde Code, Federal Meteorological Handbook 4*, p. B2-1, Silver Spring, Maryland, 1976.
- Ney, E.P., R.W. Maas, and W.F. Huch, The measurement of atmospheric temperature, *J. Meteorol.*, **18**, 60-80, 1961.
- Parker, D.E., and D.I. Cox, Towards a consistent global climatological rawinsonde data-base, *Int. J. Climatol.*, **15**, 473-496, 1995.
- Schwartz, B., and M. Govett, A hydrostatically consistent North American radiosonde data base at the Forecast Systems Laboratory, 1946-present, *Tech. Memo. ERL-FSL-4*, 81 pp., Natl. Oceanic and Atmos. Admin., Boulder, Colorado, 1992.
- Schwartz, B., and C. Wade, Considerations for the climatologist using North American radiosonde data, in *Eighth Symposium on Meteorological Observations and Instrumentation*, pp. 177-182, Am. Meteorol. Soc., Boston, Massachusetts 1993.
- Serreze, M.C., J.D. Kahl, and R.C. Schnell, Low-level temperature inversions of the Eurasian Arctic and comparisons with Soviet drifting station data, *J. Clim.*, **5**, 615-629, 1992.
- Skony, S.M., J.D.W. Kahl, and N.A. Zaitseva, Differences between radiosonde and dropsonde temperature profiles over the Arctic Ocean, *J. Atmos. Oceanic Technol.*, **11**, 1400-1408, 1994.

7134

WALDEN ET AL.: COMMENTARY

Stone, R.S., and J.D. Kahl. Variations in boundary layer properties associated with clouds and transient weather disturbances at the south pole during winter. *J. Geophys. Res.*, 96, 5137-5144, 1991.

Walden, V.P., and S.G. Warren. Atmospheric longwave radiation spectrum and near-surface atmospheric temperature profiles at South Pole Station. *Antarc. J. U. S.*, 28, 269-271, 1993.

Zaitseva, N.A., Historical developments in radiosonde systems in the former Soviet Union, *Bull. Am. Meteorol. Soc.*, 74, 1893-1900, 1993.

A. Mahesh, Geophysics Program, University of Washington, Box 351650, Seattle, WA 98195-1650. (e-mail: mahesh@atmos.washington.edu)

V.P. Walden and S.G. Warren, Department of Atmospheric Sciences, University of Washington, Box 351640, Seattle, WA 98195-1640. (e-mail: walden@atmos.washington.edu; sgw@atmos.washington.edu)

(Received January 13, 1995; revised July 14, 1995; accepted August 8, 1995.)

Appendix B. Radiosonde Temperature Measurements in Strong Inversions: Correction for Thermal Lag based on an Experiment at the South Pole

FEBRUARY 1997

MAHESH ET AL.

45

Radiosonde Temperature Measurements in Strong Inversions: Correction for Thermal Lag Based on an Experiment at the South Pole

ASHWIN MAHESH, VON P. WALDEN, AND STEPHEN G. WARREN

Geophysics Program and Department of Atmospheric Sciences, University of Washington, Seattle, Washington

(Manuscript received 29 February 1996, in final form 5 July 1996)

ABSTRACT

Very steep shallow temperature inversions occur during most of the year in the near-surface layer on the Antarctic Plateau. A radiosonde carried by a balloon rising at a few meters per second does not measure such inversions accurately because the response time of the thermistor is several seconds. To quantify this error, the authors flew a radiosonde on a tethered kite on several occasions in winter at South Pole Station immediately prior to the routine launch of the same sonde on a weather balloon. In all cases, the equilibrated temperatures measured by the tethered sonde at a given pressure level were higher than those from the balloon-borne sonde throughout most of the inversion layer. Assuming that the tethered sonde data represent the true atmospheric temperature profile, a procedure can be developed to correct the temperature data from routine radiosonde soundings for the finite response time of the thermistor. The authors devise an accurate deconvolution method to retrieve the true atmospheric temperature profile from the radiosonde data when the thermistor response time is known. However, a simple technique of shifting the profile a few seconds back in time gives results that are nearly equivalent to the deconvolution. Additional temperature errors result at the South Pole because the radiosonde is launched immediately after being brought out of a warm room, making it necessary to further adjust data from the lowest few tens of meters. It is found that the temperature errors cause a 0.3 W m^{-2} error in the computed downward longwave radiation flux in winter at the South Pole, most of which is in spectral regions dominated by emission from water vapor and carbon dioxide. This is similar to the 0.5 W m^{-2} change induced by the increase in carbon dioxide concentration from preindustrial to present values. The thermal lag is shown to be significant also for winter profiles in Alaska. A correction for thermal lag is recommended for all situations where radiosondes are used to measure steep temperature gradients in the boundary layer: in polar regions throughout the year, at midlatitude continental stations in winter, and at the tops of subtropical marine stratocumulus clouds.

1. Introduction

Temperatures reported by radiosondes are subject to several sources of error (Luers and Eskridge 1995), one of which is the thermal lag of the thermistor (Badgley 1957; Jensen 1958; Elliott and Gaffen 1991). The thermal lag has been of particular concern for measurement of temperature in the stratosphere, where the thermistor responds very slowly because of the low density of air. In the troposphere its response time is shorter, typically several seconds, and thermistors on the radiosondes used at U.S. weather stations have been unchanged since 1949 (Elliott and Gaffen 1991, Table 1; Jenne and McKee 1985, p. 1198). However, even in the troposphere the thermal lag can cause significant errors in reported temperature in situations where the sonde rises rapidly through a region where the vertical gradient of

temperature is large (Huovila and Tuominen 1989). Weather balloons carrying radiosondes typically rise at a rate of $3\text{--}5 \text{ m s}^{-1}$ in the lower atmosphere. If the ascent rate of the balloon is constant, the thermistor's lag in time corresponds to a lag in height, so that at a given altitude, the thermistor reports a temperature more appropriate to some lower height that it passed through a few seconds earlier. Quantification and correction of this lag error are the primary topics of this paper. We focus on radiosonde temperature profiles taken at South Pole Station, since steep surface-based temperature inversions occur there most of the year.

A further, related problem is that the radiosonde and its balloon are sometimes prepared in a heated or air-conditioned room and then released before the sonde equilibrates to the outside air temperature (Schwartz and Doswell 1991). This causes the temperatures reported in the lowest few tens of meters to be higher or lower than those of the ambient air. The height to which this memory of the balloon inflation room's temperature is significant depends on the actual radiosonde response time, the balloon ascent rate, and how soon the sonde

Corresponding author address: Stephen G. Warren, Department of Atmospheric Sciences, Box 351640, University of Washington, Seattle, WA 98195-1640.
E-mail: sgv@atmos.washington.edu

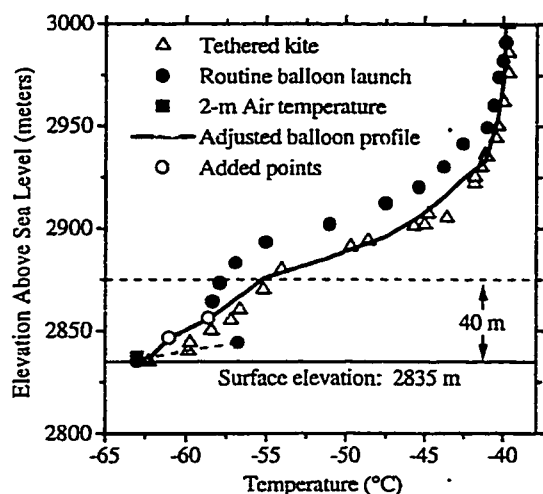


FIG. 1. Atmospheric temperature profiles above South Pole Station for 0000 UTC 28 August 1992. The filled circles are data points from the routine radiosonde launch of the South Pole Weather Office (SPWO); the open triangles are data reported by the same radiosonde on a tethered kite prior to the launch. The first point in the reported temperatures (the solid square) is not measured by the radiosonde, but is instead added to the radiosonde report from an SPWO thermometer at 2 m. The adjusted balloon profile is shown as a solid line. Radiosonde data below the dashed horizontal line at 2875 m are ignored in the adjustment procedure as discussed in the text; the balloon reached this height after 9 s. Data from other near-surface thermometers at South Pole Station that are inserted into the adjusted profile are shown as open circles.

is launched after leaving the inflation room. At the South Pole, the balloon and sonde are prepared in a heated balloon inflation tower (BIT).

Radiosondes report both temperature and humidity, but in this paper we consider only the temperature measurements. Radiosonde humidity sensors are typically calibrated only to -40°C , and we found that the sensors used at the South Pole were insensitive at temperatures below -50°C (Walden and Warren 1996, manuscript submitted to *J. Geophys. Res.*, Fig. 9). During our experiments, surface temperatures were in the range -62° to -70°C , so the humidity data are not usable. Lag errors for humidity have been discussed by Brousaides and Morrissey (1974).

2. Data

The radiosondes used at the South Pole are supplied by Atmospheric Instrumentation Research (AIR), whereas most U.S. weather stations use radiosondes supplied by VIZ Manufacturing Co. However, their thermistors are identical. AIR actually obtains sondes from VIZ but replaces the pressure sensor and data transmitter (J. Roby, AIR, 1996, personal communication). Both sondes have capacitive pressure sensors, which have response times of tens of milliseconds (Maz-

TABLE 1. Differences among the 2-m thermometers at South Pole Station. Here T_s are 2-m temperatures recorded hourly by the SPWO; T_r are the 2-m temperatures inserted into radiosonde reports, also collected by the SPWO using a different thermometer on the same observation tower. Both thermometers are aspirated. Comparisons are made by interpolating the hourly values of T_s to the time of launch. Here T_w are 2-m temperatures from an unspirated thermometer mounted on the walk-up tower and maintained by NOAA. Monthly average values of the temperature and temperature differences, indicated by the overbar, are given here for the year 1992.

Month (1992)	\bar{T}_s ($^{\circ}\text{C}$)	$\bar{T}_r - \bar{T}_s$ (K)	$\bar{T}_w - \bar{T}_s$ (K)
January	-29.3	-0.1	1.3
February	-43.1	0.0	1.4
March	-56.7	-0.1	1.0
April	-53.3	-0.1	0.5
May	-59.0	-0.3	0.6
June	-55.5	-0.4	0.6
July	-60.1	-0.4	0.5
August	-60.7	-0.5	0.6
September	-57.9	-0.3	0.5
October	-47.1	-0.1	0.5
November	-39.4	0.0	1.0
December	-30.2	-0.1	1.7

zarella 1985); this is much less than the few-second response time of the thermistor.

To quantify the temperature errors, we flew a radiosonde on a tethered parafoil kite at South Pole Station on nine occasions in August and September of 1992, immediately prior to the routine launch of the very same radiosonde by the South Pole Weather Office (SPWO). The kite was stopped at different altitudes, allowing the thermistor to equilibrate to its surrounding temperature. The kite was then reeled in, and the sonde was launched on a balloon. Five of these experiments were successful in obtaining kite profiles that extended through the inversion layer; at other times, the wind was too weak to lift the kite sufficiently. Figure 1 shows an example of the difference between a balloon profile and the corresponding kite profile.

The solid square is the 2-m air temperature measured by an SPWO thermometer upwind of the station. This temperature is an instantaneous reading made by the observer while initializing the AIR software and is routinely inserted as the first temperature in the sounding. The dashed line between the 2-m temperature and the first reported sonde temperature signifies that they are part of the same sounding. The solid circles below the horizontal dashed line (at 40 m above the surface) are affected by memory of the warm BIT (see section 3). The figure shows that the temperatures reported by the balloon-borne sonde differ by several degrees from those reported by the tethered sonde within the inversion layer. The two profiles begin to agree as the air temperature changes more slowly near the top of the inversion, 150 m above the surface.

A further complication is the lack of agreement among three 2-m temperature sensors used at South Pole Station. The South Pole Weather Office, maintained by

Antarctic Support Associates under contract from the National Science Foundation, operates two of these instruments. These are platinum-resistance thermometers made by Rosemount Inc. of Chatsworth, California; both are aspirated. They are located a few centimeters apart on the same observation tower. One is used for recording routine hourly observations of the 2-m air temperature (T_a), but it is the other whose temperatures (T_r) are inserted into the radiosonde profile. The third sensor (T_s), a platinum-resistance thermometer made by Logan Enterprises of West Liberty, Ohio, is located on a different meteorological tower less than 100 m away (Warren et al. 1993) and is operated by personnel of the Climate Monitoring and Diagnostics Laboratory (CMDL) of the National Oceanic and Atmospheric Administration (NOAA). This tower also has a temperature sensor at 21 m, as discussed below. Table 1 shows that T_r differs from T_a mainly in the wintertime, possibly due to different calibrations at low temperatures; T_s and T_a differ in all months, but by a larger amount during sunlit times, probably indicating a bias in one of the sensors as well as the influence of sunlight on the CMDL sensor, which was not aspirated in 1992. It has since been replaced with an aspirated thermometer, as has the 21-m thermometer.

3. Method

Since the thermistor has a nonzero response time, the reported temperature from the balloon-borne sonde, T_{bal} , can be approximated as a linear combination of the air temperatures T_{air} experienced at earlier times. The contribution of each T_{air} falls off with time in accordance with the response time of the thermistor. In the following derivation, we assume that the data are reported by the radiosonde at regular time intervals of spacing δt . At the South Pole, δt is 2 s. At any time t_j , the temperature reported by the balloon-borne radiosonde, $T_{bal}(t_j)$, can be related to the actual temperatures in the atmosphere it has passed through: $T_{air}(t_1), T_{air}(t_2), T_{air}(t_3), \dots, T_{air}(t_j)$, where $t_j = t_{j-1} + \delta t$ and t_1 is the time of the first report from the sonde. Using the standard notation of inversion theory (Twomey 1977), we set $g_j = T_{bal}(t_j)$ and $f_j = T_{air}(t_j)$, and obtain g_j as a weighted average of the f_k at preceding times, $k \leq j$:

$$g_j = \frac{\sum_{k=1}^j W_{jk} f_k}{\sum_{k=1}^j W_{jk}}, \quad (1)$$

where the weights are

$$W_{jk} = \exp\left[-(j-k)\frac{\delta t}{\tau}\right] \quad (2)$$

and τ is the e -folding response time of the thermistor.

Equation (1) can be conveniently rewritten as a matrix equation:

$$g_j = \sum_{k=1}^j K_{jk} f_k, \quad \text{or} \quad \mathbf{g} = \mathbf{K}\mathbf{f}, \quad (3)$$

where \mathbf{g} and \mathbf{f} are column vectors and the kernel \mathbf{K} is a lower-triangular matrix whose jk th element is given by

$$K_{jk} = \frac{W_{jk}}{\sum_{k=1}^j W_{jk}}. \quad (4)$$

In practice, the computation can be made more efficient by zeroing the leading elements of each row because they are negligible and retaining only those K_{jk} for which $j-k \leq 30$. The triangular matrix then becomes a banded matrix. For the first few reported temperatures (g_1, g_2, \dots), Eq. (1) offers a poor description because it does not contain the history of the sonde's environment prior to launch ($k \leq 0$). We therefore require a time span of 2τ to elapse after launch before using (1); that is, we use the reported values g_j only for $j \geq 2\tau/\delta t$. In Fig. 1, this level is indicated by the horizontal dashed line. Fortunately, all weather stations have a fixed thermometer measuring temperature at about 2-m height, and this temperature is inserted into the beginning of the data stream to augment the sounding before it is distributed and archived. To complete the temperature profile, one can therefore interpolate between the lowest derived temperature and the 2-m temperature, using additional data if available. The thickness of this " 2τ " layer actually varied between 34 and 73 m in our five experiments because of variations in ascent rate and thermistor response time. However, in our analysis we used 40 m as the thickness in all five cases and found it to be adequate.

Knowing the ascent rate of the balloon, the vectors \mathbf{f} and \mathbf{g} can be expressed as functions of height instead of time, and an approximate atmospheric temperature profile \mathbf{f}' can be inferred from the measurements \mathbf{g} by inverting (3) using the least squares solution

$$\mathbf{f}' = (\mathbf{K}^T \mathbf{K})^{-1} \mathbf{K}^T \mathbf{g}. \quad (5)$$

Equation (5) is an unstable inversion because of the presence of measurement errors in \mathbf{g} , so it must be constrained in some way. A constraint can easily be incorporated into the solution, as shown by Twomey (1977). A popular constraint is to require the derived profile \mathbf{f}' to be smooth minimizing its second derivative. However, for the problem of deconvoluting radiosonde temperatures, we found that the inversion process works better if instead the constraint is an a priori estimate of the solution vector (called \mathbf{h}), which is given a specified weight. Following Twomey (1977), a least squares solution for \mathbf{f}' is then obtained as

$$\mathbf{f}' = (\mathbf{K}^T \mathbf{K} + \gamma \mathbf{I})^{-1} (\mathbf{K}^T \mathbf{g} + \gamma \mathbf{h}), \quad (6)$$

TABLE 2. The response times τ_i of the radiosondes used in the five kite experiments, as determined by the shift in time needed to minimize the difference between the adjusted balloon data and the kite data. The range of possible τ_i values due to maximum temperature changes between the times of the kite and balloon flights is also given.

Date (0000 UTC)	Ascent rate (m s^{-1})	τ_i (s)	Range of possible τ_i (s)
28 August 1992	4.4	4	3–4
2 September 1992	2.7	9	7–9
3 September 1992	3.3	18	13–18
11 September 1992	2.6	13	9–13
18 September 1992	4.2	5	4–7

where γ is a “Lagrangian multiplier” chosen such that the residual $|\mathbf{Kf}' - \mathbf{g}|$ is comparable to the estimated error in the measurements \mathbf{g} , and \mathbf{I} is the identity matrix of size $\mathbf{K}^T\mathbf{K}$. The multiplier γ ranges between 0 and ∞ ; $\gamma = 0$ results in no constraint [Eq. (5)], and $\gamma = \infty$ forces $\mathbf{f}' = \mathbf{h}$.

4. Results

In an earlier attempt to correct radiosonde temperatures for thermal lag, Jensen (1958) recommended that the reported temperature at time t should simply be assigned to the pressure measured at the earlier time $t - \tau$. From our measured values of the true air temperature T_{air} collected by the tethered sondes, we determine this “Jensen profile” by shifting the balloon profile downward assuming various values of τ until the shifted profile agrees as closely as possible with the kite temperatures. We find the optimum choice of τ by minimizing the root-mean-square (rms) difference between the shifted temperatures and the kite profile within the inversion layer, ignoring points in the near-surface “ 2τ layer.” The result is an estimate of the response time τ_i (using the subscript J for Jensen). The response times we find are applicable to the South Polar near-surface layer; with decreasing pressure, the response time increases.

Table 2 shows the values of τ_i we obtain for the five soundings, indicating a range of response times from 4 to 13 s, with one outlier at 18 s to be discussed below. This variability may be partially due to manufacturing differences among radiosondes and perhaps also due to differences in ventilation at different ascent rates. However, the τ_i may also be affected by nonideal conditions during our experiments. The values we obtain are based on the assumption that the temperature structure in the inversion layer did not change between the time of the tethered kite experiment and that of the routine weather balloon launch one hour later. To test the validity of that assumption, we used data recorded at 10-min intervals by the CMDL thermometers on the meteorological tower to determine temperature trends during our experiments. The temperatures at 2 and 21 m during the hour prior to the balloon launch differed from that at the time of launch by less than 1.3 K. By shifting each

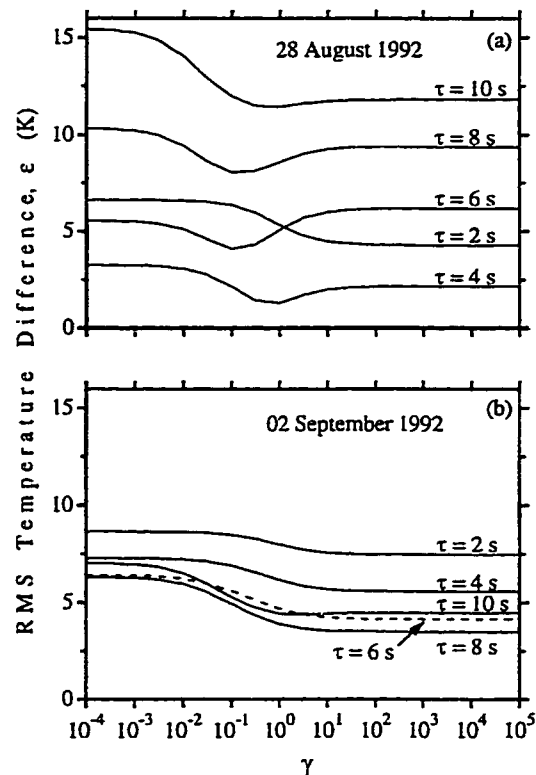


FIG. 2. The rms temperature difference (ϵ) between the deconvoluted balloon profiles and the tethered kite profiles data using various combinations of τ and γ . The difference is computed at altitudes from 40 m above the surface (or about 2τ) to the top of the tethered kite profile. (a) On 28 August 1992, ϵ reached a minimum at $\gamma = 1$ and $\tau = 4$ s. In the other four cases, one of which is shown in (b), no minimum was obtained, indicating that the inversion procedure offered no improvement over the Jensen profile.

entire balloon profile by the maximum change during the previous hour, we recalculated the values of τ_i for the five cases to see how this change in temperature might have affected our determination (Table 2). The derived response times for the five radiosondes still show significant differences, even allowing for this effect.

Now using the Jensen profile as our a priori estimate \mathbf{h} in our deconvolution, we minimize the rms difference between \mathbf{f}' and \mathbf{f} within the inversion layer by varying τ and γ . Figure 2a shows that a minimum exists for the 28 August case at $\tau = 4$ s and $\gamma = 1$. However, Fig. 2b indicates that on 2 September the best fit to the tethered kite temperatures occurs at high values of γ , where $\mathbf{f}' \approx \mathbf{h}$. This is also true of the other three cases. Therefore, we conclude that our deconvolution method is not a significant improvement upon Jensen's method, if our criterion is the ability of the adjusted profile to match the kite profile.

The principal benefit we desire from the deconvolution is to bring the smooth balloon profile into agreement with the kite profile. Our main interest is to obtain accurate calculations of radiation spectra as illustrated below, where small (meter scale) deviations from the smoothed profile have little effect. Small-scale structure in the inversion layer that is not resolved by Jensen's method could possibly be resolved by the deconvolution procedure using a small value of γ , but we are unable to judge the accuracy of such small-scale structure because it usually does not persist long enough to be seen in both profiles taken one hour apart.

Having rejected the data from the first 40 m, we assign values for the temperatures at these heights to supersede the Jensen profile. The first point in the radiosonde dataset is still useful, since it is recorded by the SPWO thermometer at 2 m, which is equilibrated with its environment. Temperatures are also available at 21 m from CMDL and at 11 m from a thermistor attached to a pyrgeometer (Walden 1995). Figure 1 shows the adjusted profile (solid line) and the inserted points (open circles).

The 11- and 21-m temperatures in the adjusted profile in Fig. 1 are lower than those reported by the kite, for two main reasons. First, on 28 August, the temperature at 21 m decreased by about 1 K between the tethered kite experiment and the balloon launch. The remaining difference may be due to a "heat island" effect. The 11- and 21-m temperatures were measured upwind of the station, whereas the kite was flown just downwind. Although the station is small, in winter the difference between indoor and outdoor temperatures is typically 80 K, so such an effect is plausible. The heat island effect is another reason why the procedure for the determination of τ_r should not use data in the lowest part of the sounding.

Raw and corrected temperature profiles for all five days are compared to kite flights in Fig. 3. Having the tethered kite data for these five days allows us to determine how much the reported temperatures need to be shifted, thereby giving an estimate for the response time of the thermistor (Table 2). However, for routine soundings throughout the year, we do not have the benefit of the kite data, so we must assume an average response time. The 3 September profile in Fig. 3 appears to be an outlier. Its τ_r was poorly determined, because the balloon profile on this day had only two data points in the lowest 145 m. This may be partly responsible for the high value of τ_r determined for this case. We therefore take the average response time of the thermistor to be the average of the other four cases, that is, 8 s. The response time should be proportional to atmospheric density, so this value of 8 s at the South Pole, at a surface pressure of 700 mb, corresponds to 5.6 s at sea level, in agreement with the 5–6-s value stated by the manufacturer.

The error due to thermal lag may be greater on average than it is in the cases shown here, since the in-

versions shown in Fig. 3, except for 28 August, were actually weaker than the monthly average inversion. This is because the kite experiments were successful only on days with sufficient wind to lift the kite. Winds tend to mix the boundary layer, weakening the inversion.

We examined the possibility that corrections for thermal lag had been instituted at times in the past, especially in the 1950s when the lag of the thermistors first began to be understood. Early studies of radiosonde thermal lags focused on corrections to temperatures recorded in the stratosphere, where the lags produce large errors because of the low air density (Badgley 1957). Although a correction for thermal lag may have been applied routinely in the past at some Antarctic stations (B. Gardiner 1993, personal communication), such a correction was apparently never applied at South Pole Station, even in its first years of operation in the late 1950s (E. Flowers 1994, personal communication). The radiosonde thermistors now used at South Pole Station are made by VIZ Manufacturing Co., as are those used at most other U.S. weather stations. These radiosondes are normally assumed to have a response time τ of 5–6 s (M. Friedman, VIZ Manufacturing Co., 1994, personal communication), but our experiments suggest that τ is variable (Table 2). No correction for thermal lag is now made to radiosonde data from U.S. stations either in the process of recording the data or in being sent out to the Global Telecommunications System to be archived (D. Gaffen, F. Schmidlin, and R. Tanner 1994, personal communication). Some corrections for solar heating of thermistors were instituted for data between 400 and 10 mb, but that procedure was discontinued when the thermistors began to be coated with white paint in 1960 (Jenne and McKee 1985; Gaffen 1994).

5. Application to non-Antarctic locations

Adjustments to the reported temperatures may be important at other high-latitude weather stations as well, where strong near-surface temperature inversions are common in winter. Most data available from such stations are at coarser time resolution than the 2-s data we have for South Pole Station. Before May 1995, only data from mandatory and significant levels were routinely available; however, data from U.S.-controlled upper-air sites are now available at 6-s resolution from the National Climatic Data Center. Also, supplementary temperature data (such as the tower temperatures at the South Pole) are not normally available. In such cases, we can still use the principles of the method we have developed for the South Pole. As an example, we took the mandatory- and significant-level temperatures reported by the radiosondes at Fairbanks, Alaska, in 1989, and shifted them by a similar procedure. This is justified since, prior to March 1990, VIZ radiosondes were used at Fairbanks (Schwartz and Govett 1992). Because the weather station at Fairbanks is at an elevation of only 135 m, we used a response time of 5.6 s.

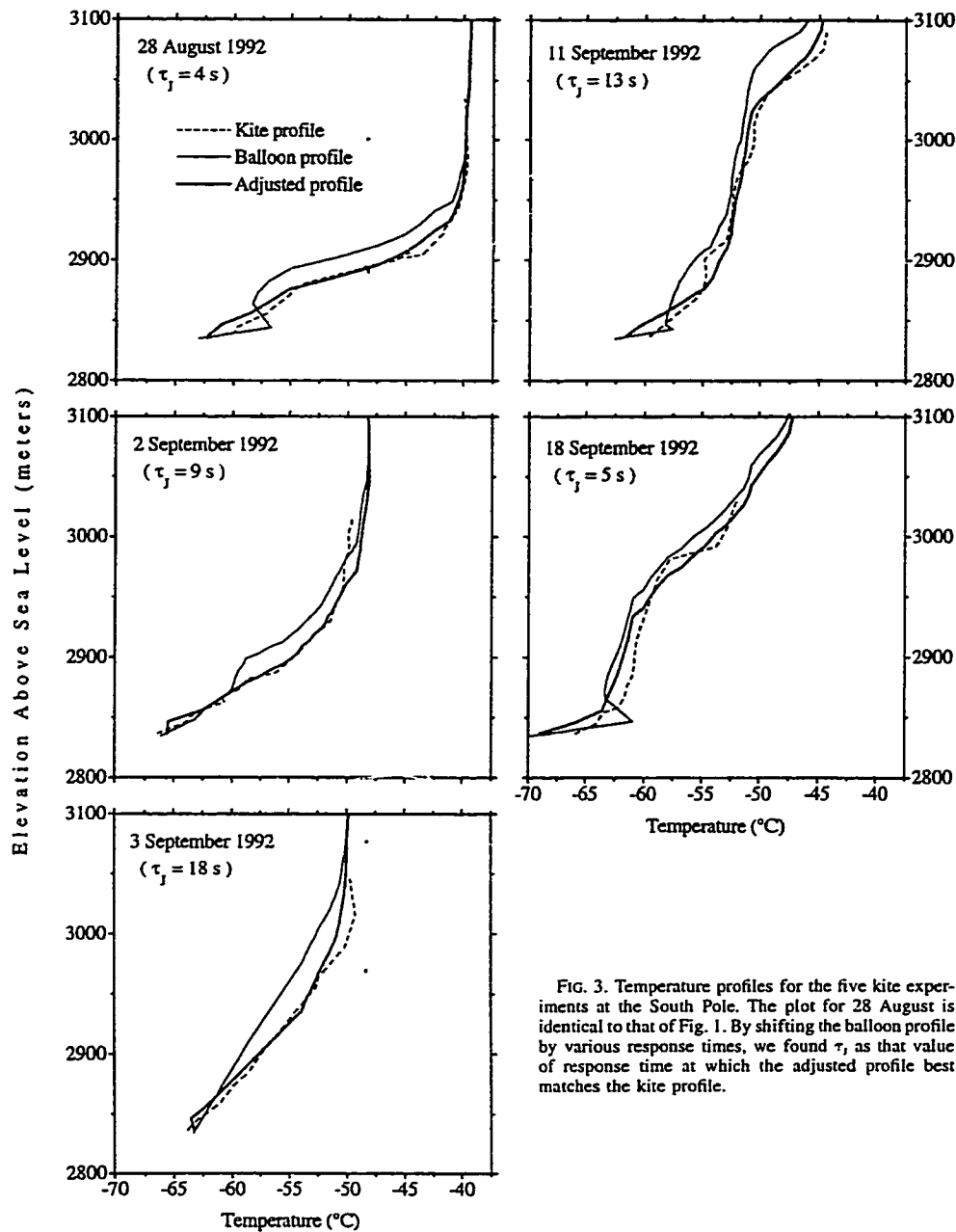


FIG. 3. Temperature profiles for the five kite experiments at the South Pole. The plot for 28 August is identical to that of Fig. 1. By shifting the balloon profile by various response times, we found τ_j as that value of response time at which the adjusted profile best matches the kite profile.

We ignored data within the 2τ layer, estimated to extend up to an elevation of 190 m. We then specified a point at 190 m by interpolating between the heights at which data were available immediately below and above 190 m. These data, from 190 m and upward, are

then shifted by the estimated average response time of 5.6 s according to the Jensen procedure. We then linearly connect the point at 190 m to the 2-m air temperature. Figure 4 shows the reported and adjusted profiles from data taken at Fairbanks. The effect of thermal lag on

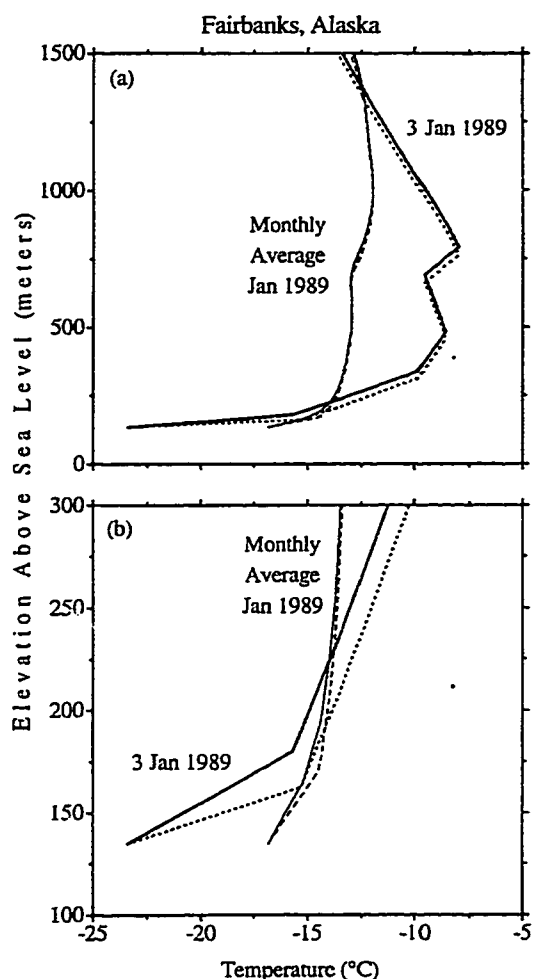


FIG. 4. Thermal lag corrections at Fairbanks (65°N , 148°W). The solid lines are unadjusted profiles from the station; the dashed and dotted lines are the adjusted profiles. The lowest 160 m of the profiles are shown on an expanded scale in (b).

the accuracy of the temperatures is small in the monthly average profile. However, errors can be significant on individual days with steep inversions, as shown in the figure. These errors can affect the analysis of inversion heights (Huovila and Tuominen 1989; Skony et al. 1994; Walden et al. 1996).

6. Implications for radiative transfer modeling

The downward longwave radiation spectrum at the surface is affected by the near-surface atmospheric temperature structure. Temperature errors within the inversion layer at the South Pole may therefore cause significant errors in radiative transfer calculations. We in-

vestigated this possibility using MODTRAN3, a radiative transfer model with moderate spectral resolution (Berk et al. 1989), in conjunction with temperature data from 2 September 1992. We show this case because its 9-s response time is closest to our estimate of the average response time. We computed the clear-sky downward infrared radiance at the surface from the adjusted profile and compared this spectrum to that calculated using the unadjusted profile. In these calculations, only the temperatures below the height of the inversion (3.2 km above sea level) were adjusted. The effects of possible lag errors above the near-surface layer were not investigated, because the lapse rate is sufficiently small through the free troposphere that the thermistor can respond adequately. Tropospheric water vapor concentrations were specified by saturating (with respect to ice) the near-surface layer up to the height of the inversion, and by setting the relative humidity above this layer, but below 7 km, to 75% (Walden and Warren 1996, manuscript submitted to *J. Geophys. Res.*). Stratospheric values were fixed at 4 ppmv, consistent with measurements made by Rosen et al. (1991) at the South Pole in winter using sondes equipped with frost-point hygrometers. Since relative humidity is fixed in the model troposphere, the absolute humidity in the near-surface layer is higher in the adjusted profile than in the unadjusted one. The vertical profile of ozone was specified using CMDL ozonesonde data from 1992 (Bodhaine et al. 1993). Carbon dioxide concentrations at the South Pole come from Keeling and Whorf (1994), while other radiative gases such as methane and nitrous oxide are specified at the values of the subarctic winter model atmosphere (McClatchey et al. 1972).

Figure 5a shows the longwave spectrum for a viewing angle of 60° between 0 and 2500 cm^{-1} (wavelength greater than $4\text{ }\mu\text{m}$) using the adjusted temperature profile. Figure 5b gives the error in radiance (bold line) caused by not adjusting the profile. Radiance differences occur mainly in spectral regions dominated by emission from water vapor and carbon dioxide. The differences are mostly negative because the reported temperature profile is colder than the true profile, and the reported humidity profile is drier than the true profile. The region of positive differences corresponds to the center of the carbon dioxide band, where the absorption length for photons is short, and occurs because the unadjusted profile is warmer than the adjusted profile in the first 20 m above the surface. Thus, the practice of launching radiosondes directly from the heated BIT at South Pole has a noticeable effect on radiative transfer calculations.

The downward longwave flux is determined by integrating the radiance over the hemispheric field of view (calculated at every 10° of zenith angle) and over the entire longwave spectrum. The error in computed clear-sky flux caused by using the unadjusted profile is about -0.3 W m^{-2} out of a total of 58 W m^{-2} . This error can be compared to the difference in flux using preindustrial instead of current concentrations of carbon dioxide, that

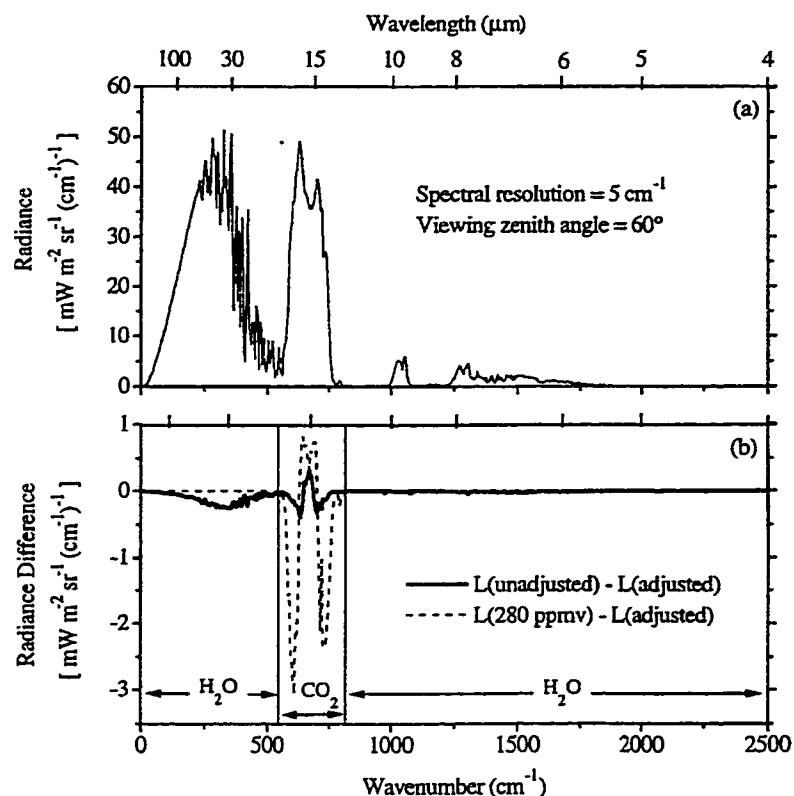


FIG. 5. (a) Spectral downward longwave radiance calculated by radiative transfer model MODTRAN3 using the adjusted temperature profile for 2 September 1992. (b) The effect on the computed downward longwave radiance caused by adjusting the reported temperatures at the South Pole. Here $L(\text{adjusted})$ is the spectral radiance calculated using the adjusted temperature profile; $L(\text{unadjusted})$ uses the temperature profile directly as reported by the balloon-borne radiosonde; $L(280 \text{ ppmv})$ is the spectral radiance using the adjusted profile, but with a carbon dioxide concentration of 280 ppmv; $L(\text{adjusted})$ and $L(\text{unadjusted})$ use 360 ppmv.

is, 280 instead of 360 ppmv. The dashed line in Fig. 5b shows this difference; the corresponding flux difference is -0.5 W m^{-2} .

7. Conclusions

The slow response of thermistors used in radiosondes is useful to provide some smoothing in the measured temperature profile. However, in atmospheres with steep temperature gradients, the slow response causes the data to be biased. Correcting for the slow response is important not only at the South Pole but wherever rapid changes in temperature in the lower troposphere are recorded by balloon-borne radiosondes. Near-surface inversions are common in the Arctic throughout the year (Vowinckel and Orvig 1970) and at midlatitude continental locations in winter. The correction could also be significant at the tops of subtropical marine stratocumulus clouds, where, at a pressure level of 800–900

mb, the reported temperature typically rises by 5–10 K over 50 m or less (Nicholls and Leighton 1986).

The error due to thermal lag can be corrected accurately if the response time of the radiosonde is known. However, different sondes, even those made by the same manufacturer, appear to have different response times. Why this variability exists is unclear. Possible explanations include inconsistent manufacturing and differences in ventilation produced by different ascent rates. A sophisticated deconvolution procedure turns out to be no more accurate than a simple shifting of the profile downward in height as proposed by Jensen in 1958. At the South Pole, temperature profiles should also be adjusted for errors caused by the balloon-launching procedure, namely, spurious warm temperatures reported immediately after the sonde has left the warm inflation tower. Such a correction may also be important in hot climates, if the sonde is prepared in an air-conditioned room that is significantly cooler than the outside ambient

air (Schwartz and Doswell 1991). Allowing the radiosonde to equilibrate outdoors for 1 min before launch would eliminate such effects at both warm and cold stations and the need for supplementary data. The National Weather Service (1974) specifies that when the temperature at which the sonde is prepared for launch differs from the outside temperature by more than 30°C, 10 min should be allowed for the sonde to equilibrate. Such a long wait might be necessary to allow the hygrometer to register the true outside humidity, but the temperature sensor should equilibrate to the outside temperature within 1 min.

Radiative transfer modeling indicates that the thermal lags produce a half-percent error in the downward longwave flux for clear sky in winter at the South Pole. This is comparable to that caused by the change in atmospheric concentration of carbon dioxide from preindustrial to current values.

Acknowledgments. We thank Prof. Takeshi Ohtake (University of Alaska) for the use of his kite and winch for the tethered kite experiments. The South Pole weather observers for 1992, Kitt Hughes and Bob Koney (National Weather Service, Kauai), provided considerable assistance with the tethered kite experiments and were essential to the success of the project. Dan Ireland, South Pole meteorologist for 1996, provided further information about procedures and instruments. We thank Dian Gaffen (NOAA), Maurice Friedman (VIZ Corp.), Ed Flowers (NOAA-ERL, retired), Brian Gardiner (British Antarctic Survey), Frank Schmidlin (NASA), and Roger Tanner (NOAA-NCDC) for information about radiosonde operational procedures. Sam Oltmans provided the ozone profiles. We thank Barry Schwartz and two anonymous reviewers for their comments. This research was supported by NSF Grants OPP-91-20380 and OPP-94-21096.

REFERENCES

- Badgley, F. I., 1957: Response of radiosonde thermistors. *Rev. Sci. Instrum.*, **28**, 1079–1084.
- Berk, A., L. S. Bernstein, and D. C. Robertson, 1989: Modtran: A moderate resolution model for Lowtran 7. Rep. GL-TR-89-0122, 38 pp. [Available from Geophysics Laboratory, Hanscom Air Force Base, MA 01731-5000.]
- Bodhaine, B., and Coauthors, 1993: Aerosol, radiation, ozone, and water vapor division. Climate Monitoring and Diagnostics Laboratory Summary Rep. 1992, 131 pp. [Available from NOAA, 325 Broadway, Boulder, CO 80303.]
- Brousailles, F. J., and J. F. Morrissey, 1974: Residual temperature-induced humidity errors in the National Weather Service radiosonde, final report. Rep. AFCRL-TR-74-0111, 40 pp. [Available from Meteorology Laboratory, Hanscom Air Force Base, MA 01731-5000.]
- Elliott, W. P., and D. J. Gaffen, 1991: On the utility of radiosonde humidity archives for climate studies. *Bull. Amer. Meteor. Soc.*, **72**, 1507–1520.
- Gaffen, D. J., 1994: Temporal inhomogeneities in radiosonde temperature records. *J. Geophys. Res.*, **99**, 3667–3676.
- Huovila, S., and A. Tuominen, 1989: Effect of radiosonde lag errors on upper-air climatological data. WMO Instruments and Observing Methods Rep. 35, WMO/TD No. 303, 291–297 pp. [Available from World Meteor. Org., Publications Sales Unit, Case Postale 2300, CH-1211 Geneva 2, Switzerland.]
- Jenne, R. L., and T. B. McKee, 1985: Data. *Handbook of Applied Meteorology*. D. D. Houghton, Ed., John Wiley and Sons, 1175–1281.
- Jensen, A., 1958: Correction of radiosonde measurements for lag error. *Geophysica*, **6**, 275–279.
- Keeling, C. D., and T. P. Whorf, 1994: Atmospheric CO₂ records from sites in the SIO air sampling network. *Trends '93. A Compendium of Data on Global Change*, T. A. Boden, D. P. Kaiser, R. J. Sepanski, and F. W. Stoss, Eds., Carbon Dioxide Information Analysis Center, 16–26.
- Luers, J. K., and R. E. Eskridge, 1995: Temperature corrections for the VIZ and Vaisala radiosondes. *J. Appl. Meteor.*, **34**, 1241–1253.
- Mazzarella, D. E., 1985: Measurements today. *Handbook of Applied Meteorology*. D. D. Houghton, Ed., John Wiley and Sons, 283–328.
- McClatchey, R. A., R. W. Fenn, J. E. A. Selby, F. E. Volz, and J. S. Garing, 1972: Optical properties of the atmosphere. Rep. AFCRL-72-0497, 108 pp. [Available from Geophysics Laboratory, Hanscom Air Force Base, Bedford, MA 01731.]
- National Weather Service, 1974: *Federal Meteorological Handbook No. 3, Radiosonde Observations*. B2-21, 731 pp. [Available from Superintendent of Documents, U.S. Government Printing Office, Washington, DC 20402.]
- Nicholls, S., and J. Leighton, 1986: An observational study of the structure of stratiform cloud sheets: Part I. Structure. *Quart. J. Roy. Meteor. Soc.*, **112**, 431–460.
- Rosen, J. M., N. T. Kjöme, and S. J. Oltmans, 1991: Balloon borne observations of frost point and ozone in polar stratospheric clouds at the South Pole. *Geophys. Res. Lett.*, **18**, 171–174.
- Schwartz, B. E., and C. A. Doswell III, 1991: North American rawinsonde observations: Problems, concerns, and a call to action. *Bull. Amer. Meteor. Soc.*, **72**, 1885–1896.
- , and M. Govett, 1992: A hydrostatically consistent North American radiosonde data base at the Forecast Systems Laboratory, 1946–present. Tech. Memo. ERL-FSL-4, 81 pp. [Available from NOAA, 325 Broadway, Boulder, CO 80303.]
- Skony, S. M., J. D. W. Kahl, and N. A. Zaitseva, 1994: Differences between radiosonde and dropsonde temperature profiles over the Arctic Ocean. *J. Atmos. Oceanic Technol.*, **11**, 1400–1408.
- Twomey, S., 1977: *Introduction to the Mathematics of Inversion in Remote Sensing and Indirect Measurements*. Elsevier, 243 pp.
- Vowinkel, E., and S. Orvig, 1970: The climate of the north polar basin. *Climates of the Polar Regions*, Vol. 14, *World Survey of Climatology*, S. Orvig, Ed., Elsevier, 129–252.
- Walden, V. P., 1995: The downward longwave radiation spectrum over the Antarctic plateau. Ph.D. thesis, University of Washington, Seattle, WA, 267 pp.
- , A. Mahesh, and S. G. Warren, 1996: Comment on "Recent changes in the North American Arctic boundary layer in winter." *J. Geophys. Res.*, **101**, 7127–7134.
- Warren, S. G., M. Starbuck, and C. Groeneveld, 1993: Relative elevations of meteorological facilities at South Pole Station. *Antarct. J. United States*, **28**, 271–273.

VITA

Ashwin Mahesh was born in June 1969 in Madras, India to C.N.U.Maheswaran and Sudha Mahesh. He attended school in Madras and then in Bangalore, graduating from high school in 1984. He received his Bachelors degree in Science from Bangalore University in May 1989, and a Masters degree in Business Administration from Pondicherry University in May 1991. He then enrolled in the graduate program in Astronomy at Vanderbilt University in Nashville, and received his Masters there in August 1993, before coming to the Geophysics Program at the University of Washington for his Ph.D.

Publications: (* indicates peer-reviewed journal)

Mahesh, Ash, Stephen G. Warren, Von P. Walden, Kitt Hughes and Robert Koney, 1995: Radiosonde temperature profiles at South Pole: Correction for thermal lag. Fourth Conference on Polar Meteorology and Oceanography. American Meteorological Society, Jan 15-20, 1995. Dallas, TX, 22-23.

Warren, Stephen G., Ash Mahesh and Von P. Walden, 1995: Heights of temperature inversion in the Arctic troposphere; a multi-decadal trend? Fourth Conference on Polar Meteorology and Oceanography, American Meteorological Society, Jan 15-20, 1995. Dallas, TX, 278-279.

* Weintraub, D. A., Joel Kastner and Ashwin Mahesh, 1994: The discovery of a companion star to Lkha 234. *Astrophysical Journal*, 420, L87-L90.

* Walden, V. P., Ashwin Mahesh and Stephen G. Warren, 1996: Comment on "Recent changes in the North American Arctic boundary layer in winter" by R. S. Bradley et. al., *Journal of Geophysical Research*, 101, D3, 7127-7134.

* Mahesh, Ashwin, Von P. Walden and Stephen G. Warren, 1997: Radiosonde Temperature Measurements in Strong Inversions: Correction for Thermal Lag Based on an Experiment at the South Pole., *Journal of Atmospheric and Oceanic Technology*, 14, 45-53.

Mahesh, Ashwin, Von P. Walden, and Stephen G. Warren, 1996: Ground-based remote sensing of cloud base heights at South Pole using CO₂-slicing. Proceedings of the International Radiation Symposium, August 19-24, 1996, Fairbanks, Alaska, USA. Deepak Publishing, Virginia.

Mahesh, Ashwin, Von P. Walden, and Stephen G. Warren, 1997: Ground-based remote sensing of cloud optical depths at South Pole. Proceedings of the International Association of Meteorology and Atmospheric Science Conference. July 2-9, 1997. Melbourne, Australia.

Walden, Von P, Ash Mahesh and Stephen Warren, 1997: Climate Studies over the Antarctic Plateau using downward infrared radiance spectra. Proceedings of the Conference on Polar Processes and Global Climate, Orcas Island, Washington, USA., in press.

* Ashwin Mahesh, Von P. Walden and Stephen G. Warren, 1998: Ground-based remote sensing of infrared cloud properties over the Antarctic Plateau, Part I: Cloud base heights. *J. Appl. Meteor.*, in preparation.

* Ashwin Mahesh, Von P. Walden and Stephen G. Warren, 1998: Ground-based remote sensing of infrared cloud properties over the Antarctic Plateau, Part II: Optical depths and particle sizes. *J. Appl. Meteor.*, in preparation.

Ashwin Mahesh, Von P. Walden and Stephen G. Warren, 1998: Ground-based remote sensing of cloud optical depths and particle sizes at South Pole. Proceedings of the 10th Conference on Atmospheric Radiation, Madison WI, June 28 - July 2, 1999.